Molecular-frame measurements of light-induced processes using rotational coherences driven by ultrafast laser pulses

by

Huynh Van Sa Lam

B.A., Ho Chi Minh City University of Education, Vietnam, 2013

AN ABSTRACT OF A DISSERTATION

submitted in partial fulfillment of the
requirements for the degree

DOCTOR OF PHILOSOPHY

Department of Physics
College of Arts and Sciences

KANSAS STATE UNIVERSITY
Manhattan, Kansas

2021

Abstract

One of the main goals of ultrafast atomic, molecular, and optical physics is to monitor and control chemical reactions in real time. Ultrashort laser pulses (time scales in picoseconds or shorter) provide sufficiently high spatio-temporal resolution to study the reaction dynamics. Together with the development of shorter pulses, studies of these reactions in three-dimensional (3D) space are also crucial since the 3D structures determine the physical and chemical properties of molecules. For example, stereoisomers, such as chiral molecules, have the same molecular formula but can behave very differently in reactions with other stereoisomers or optical pulses because of the different orientations of their atoms in space. However, in a gas-phase experiment, the orientation-dependent information is usually lost after averaging over a randomly distributed molecular sample. Many different methods have been investigated to solve this important problem.

In 2014, Makhija *et al.*[1] demonstrated that the angle-dependent strong-field ionization of ethylene (C_2H_4), an asymmetric top molecule, can be retrieved from a time-resolved measurement of the yield of the cation. In this pump-probe experiment, the pump aligns and the probe ionizes the molecules, and the ion yield is measured as a function of pump-probe delay. The angle dependence is retrieved from fitting to this delay-dependent ion yield. This time-domain approach, called Orientation Resolution through Rotational Coherence Spectroscopy (ORRCS), has many advantages that can be exploited in other applications. The main theme of this work is the further development of ORRCS for extracting orientation-resolved information of different processes from rotational wave packet dynamics.

The first goal of this dissertation is to systematically investigate and develop the ORRCS retrieval algorithm, since the retrieval of the angle dependence is sensitive to many parameters. We perform a series of experiments and statistical analyses to evaluate different types

---

[1] Varun Makhija, *Laser-induced rotational dynamics as a route to molecular frame measurements*, Ph.D. dissertation, Kansas State University, 2014

of errors, determine the appropriate size of the model, and check the consistency of the retrieval. Specifically, we look at the angle-dependent strong-field ionization of carbon dioxide (CO_2, a linear molecule) and sulfur dioxide (SO_2, an asymmetric top molecule). Strong-field ionization of CO_2 has been discussed extensively in the literature because there were significant discrepancies between different experiments and theories, while SO_2 has been used extensively in other experiments.

The second goal of this dissertation is to expand the time-domain approach to momentum measurements. With this new development, we present two applications of ORRCS to the dissociation and photoionization of molecules. In the dissociation of molecules, the axial recoil approximation is often used without validation. We show that this approximation can be tested by measuring the momentum distributions of the fragment ions as a function of pump-probe delay. In particular, we examine the dissociation of CO_2 and N_2 with 800 nm and 262 nm laser pulses, respectively. In each case, we determine how the likelihood of dissociation depends on the initial orientation of the molecule and the effect of the laser field on the momentum distribution of the fragment ions.

With a similar framework but different interpretation, we show that substantial information about molecular-frame photoelectron angular distributions can be obtained using rotational wave packets. We retrieve the alignment dependence of photoelectron angular distributions from N_2, CO_2, and C_2H_4 in the few-photon ionization regime. We also compare few-photon ionization with single-photon ionization and strong-field ionization to enrich our knowledge in this regime, which is not very well understood.

We believe that the time-domain approach discussed in this work is useful in many areas of ultrafast physics and chemistry. With the rapid development of high-repetition-rate light sources in recent years, we expect that many measurements, including those using x-ray free-electron lasers and ultrafast electron beams, will have the ability to apply our method and gain valuable insights into molecular structures and dynamics in the near future.

Molecular-frame measurements of light-induced processes using rotational coherences driven by ultrafast laser pulses

by

Huynh Van Sa Lam

B.A., Ho Chi Minh City University of Education, Vietnam, 2013

A DISSERTATION

submitted in partial fulfillment of the
requirements for the degree

DOCTOR OF PHILOSOPHY

Department of Physics
College of Arts and Sciences

KANSAS STATE UNIVERSITY
Manhattan, Kansas

2021

Approved by:

Major Professor
Vinod Kumarappan

Copyright

© Huynh Lam 2021

My fist steps

into the world of ultrafast atomic, molecular and optical physics

Abstract

One of the main goals of ultrafast atomic, molecular, and optical physics is to monitor and control chemical reactions in real time. Ultrashort laser pulses (time scales in picoseconds or shorter) provide sufficiently high spatio-temporal resolution to study the reaction dynamics. Together with the development of shorter pulses, studies of these reactions in three-dimensional (3D) space are also crucial since the 3D structures determine the physical and chemical properties of molecules. For example, stereoisomers, such as chiral molecules, have the same molecular formula but can behave very differently in reactions with other stereoisomers or optical pulses because of the different orientations of their atoms in space. However, in a gas-phase experiment, the orientation-dependent information is usually lost after averaging over a randomly distributed molecular sample. Many different methods have been investigated to solve this important problem.

In 2014, Makhija *et al.*[2] demonstrated that the angle-dependent strong-field ionization of ethylene (C_2H_4), an asymmetric top molecule, can be retrieved from a time-resolved measurement of the yield of the cation. In this pump-probe experiment, the pump aligns and the probe ionizes the molecules, and the ion yield is measured as a function of pump-probe delay. The angle dependence is retrieved from fitting to this delay-dependent ion yield. This time-domain approach, called Orientation Resolution through Rotational Coherence Spectroscopy (ORRCS), has many advantages that can be exploited in other applications. The main theme of this work is the further development of ORRCS for extracting orientation-resolved information of different processes from rotational wave packet dynamics.

The first goal of this dissertation is to systematically investigate and develop the ORRCS retrieval algorithm, since the retrieval of the angle dependence is sensitive to many parameters. We perform a series of experiments and statistical analyses to evaluate different types

---

[2] Varun Makhija, *Laser-induced rotational dynamics as a route to molecular frame measurements*, Ph.D. dissertation, Kansas State University, 2014

of errors, determine the appropriate size of the model, and check the consistency of the retrieval. Specifically, we look at the angle-dependent strong-field ionization of carbon dioxide (CO_2, a linear molecule) and sulfur dioxide (SO_2, an asymmetric top molecule). Strong-field ionization of CO_2 has been discussed extensively in the literature because there were significant discrepancies between different experiments and theories, while SO_2 has been used extensively in other experiments.

The second goal of this dissertation is to expand the time-domain approach to momentum measurements. With this new development, we present two applications of ORRCS to the dissociation and photoionization of molecules. In the dissociation of molecules, the axial recoil approximation is often used without validation. We show that this approximation can be tested by measuring the momentum distributions of the fragment ions as a function of pump-probe delay. In particular, we examine the dissociation of CO_2 and N_2 with 800 nm and 262 nm laser pulses, respectively. In each case, we determine how the likelihood of dissociation depends on the initial orientation of the molecule and the effect of the laser field on the momentum distribution of the fragment ions.

With a similar framework but different interpretation, we show that substantial information about molecular-frame photoelectron angular distributions can be obtained using rotational wave packets. We retrieve the alignment dependence of photoelectron angular distributions from N_2, CO_2, and C_2H_4 in the few-photon ionization regime. We also compare few-photon ionization with single-photon ionization and strong-field ionization to enrich our knowledge in this regime, which is not very well understood.

We believe that the time-domain approach discussed in this work is useful in many areas of ultrafast physics and chemistry. With the rapid development of high-repetition-rate light sources in recent years, we expect that many measurements, including those using x-ray free-electron lasers and ultrafast electron beams, will have the ability to apply our method and gain valuable insights into molecular structures and dynamics in the near future.

Table of Contents

List of Figures

List of Tables

Acknowledgments

I would like to sincerely thank my advisor, Dr. Vinod Kumarappan, for his guidance throughout my doctoral study. I have been working under Vinod's supervision since my second semester at Kansas State University. I always remember my first summer when there were no senior students or postdocs in our lab at that time, and my practical experience in the field was almost zero. Vinod spent his nights and weekends patiently teaching me basic skills on aligning and using each experimental equipment. Sometimes we came out of the lab around 3 A.M., and he offered me a ride home. That will always be my sweet memory as the first step of becoming an experimentalist. I also appreciate every discussion with Vinod. While discussing physics with him, I am not afraid to ask any questions. No matter what inane questions that I ask, he always patiently explain until I understand. I have never ceased to be amazed by his deep and rigorous wealth of knowledge and his ability to provide answers with clarity. Vinod encourages me to not stop at finishing a project and publishing a paper but also dig deeper for the beauty and elegance of physics. I always wonder when I can reach his level, I can only hope some part of it has been transferred to me.

I want to acknowledge all of the current and former members in our group — Tomthin Nganba Wangjam, Dr. Suresh Yarlagadda, Dr. Rajesh Kushawaha, Dr. Varun Makhija, and Dr. Xiaoming Ren. Being a graduate student, I spent the majority of my time in the lab. I want to thank my labmate, Tomthin, for sticking with me over the last five years. Tomthin and I have different personalities and working styles; I hope we have been complementing each other in some sense. I also spent a significant amount of time working with Suresh and Rajesh on the ionization project. Many codes and equipment that we have been using were built by former students Varun and Ren — who have always kindly responded to my emails when I needed help. Together, we went through many ups and downs, fixed many broken apparatus, to pursue our dream of exploring physics.

For the Tpx3Cam experiment, I must acknowledge our collaborators — Dr. Daniel

Rolles and his student Anbu Venkatachalam, Dr. Thomas Weinacht and his student Chuan Cheng, Dr. Andrei Nomerotski and his student Peter Svihra. The exchange of ideas between different groups has a very positive impact on me, and I believe that it would take me forever to figure out how to run the Tpx3Cam without their help. I also would like to thank Dr. Eric Wells and his group for appreciating our contribution in the work on strong-field control[3]. I also want to thank Dr. Daniel Rolles, Dr. Chii-Dong Lin, Dr. Martin Centurion, and Dr. Dunja Perić for serving on my committee and carefully reading my thesis.

I want to acknowledge Dr. Cosmin Blaga and his students, Sajed Hosseini-Zavareh and Eric Mullins, for keeping the HITS laser running in our oxygen experiments. I am also grateful to the technical staff at James R. Macdonald Lab — Al Rankin, Justin Millette, Chris Aikens, Scott Chainey, and Vince Needham — for their help in solving technical problems. I want to thank Kevin for proofreading this dissertation and Charles for helping with the safety while we were running sulfur dioxide. I am also grateful to all members of the Physics Department and Kansas State University, for taking care of my life and broadening my experience as an international graduate student.

I am not a workaholic, but I have a terrible habit of ignoring everything else while I am working — skipping meals, staying up all night, or even forgetting the world outside. I believe I would not last long without the support from my friends. I thank all my friends for their friendship and their help in all aspects. Thanks for occasionally checking if I was still okay and giving me food to make sure that I was not starving. Thanks for organizing all the trips to explore the USA. You all made this journey more enjoyable and sustainable.

And last but not least, I am forever indebted to my parents and my younger sister at home in Vietnam. Even though they do not understand what I have been doing, they always provide me their endless love and support. I love you — mom, dad, and Mèo!

This work was supported by the Chemical Sciences, Geosciences, and Biosciences Division, Office of Basic Energy Sciences, Office of Science, US Department of Energy under Award No. DE-FG02-86ER13491.

---

[3] Iwamoto *et al.*, J. Chem. Phys. 152, 054302 (2020)

Chapter 1

Introduction

In this chapter, we briefly review the motivations and developments of time-resolved and angle-resolved measurements of gas-phase molecules in the effort to monitor and control chemical reactions in real-time of atomic, molecular, and optical physics. In particular, we discuss why molecular-frame measurements are important in various contexts and how measurements in the molecular frame can be achieved using different methods. Finally, by situating our work in this broad context, we provide a succinct overview of the work presented in this dissertation and why this contribution is necessary.

1.1 The motivations and developments of time-resolved and angle-resolved measurements

One of the main goals of atomic, molecular, and optical physics is to monitor and control chemical reactions in real time. This has become possible thanks to the invention of ultrashort optical pulses from mode-locked lasers[1,2], where ultrashort refers to a time scale of picoseconds and shorter[3]. Over the years, tremendous progress has been made, and the pulse duration in the visible wavelength range has reached its fundamental limitation of a few femtoseconds (roughly one optical cycle in the time domain)[4–6]. Generating isolated pulses with high flux at shorter time scales and shorter wavelengths has also been an active area of research[7]. In most ultrafast experiments, a short laser pulse is used either directly as a probe or indirectly to produce short pulses of other wavelengths in the electromagnetic spectrum (including x-rays), or short pulses of particles (such as electrons)[8–16]. The rapid development of ultrashort pulses has had a great impact on many areas of science and technology, such as ultrafast spectroscopy, laser-controlled chemistry, optical communications, biomedical applications, and materials processing[3]. Notable recognitions include the 1999 Nobel Prize in Chemistry awarded to A. Zewail for inventing "femtochemistry" and the 2018 Nobel Prize in Physics awarded to A. Ashkin, G. Mourou, D. Strickland for "groundbreaking inventions in the field of laser physics".

Together with the development of shorter pulses, studies of chemical reactions in three-dimensional (3D) space are also crucial since the 3D structures determine the physical and chemical properties of molecules[17–19]. For example, stereoisomers have the same molecular formula but can behave very differently in reactions with other stereoisomers or optical pulses because of the different orientations of their atoms in space[19–21]. However, the random distribution of gas-phase molecules would wash out much of the orientation-dependent information in any measurement. Hence, it is of great interest to break the isotropic distribution and collect information about dynamical processes in the molecular frame (MF) to reveal more details about molecular structure and dynamics[22–25]. Before discussing how molecular frame information can be accessed in the next section, we would like to examine what new knowledge we can gain by doing so in various circumstances. Some important examples are discussed below.

1.1.1 Ionization

Photoionization is a well-established method for examining the properties of molecules. By measuring the spectra of the ionization products (ions, electrons), we gain information about the energy levels of the molecular electronic states. Angle-resolved spectra can provide knowledge about the shape and the symmetry of molecular orbitals[26,27]. With ultrashort and intense laser pulses, ionization happens in a strong laser field and is called strong-field ionization (SFI)[28]. The strong laser field makes it possible to remove valence electrons from molecules with photon energies much smaller than the ionization energy. As demonstrated experimentally[29–31] and theoretically[32,33], the probability of SFI depends on the relative orientation of the molecule in the laser field; furthermore, the angle-dependent ionization probability can mimic the shape of the ionized orbital. A strong laser field can simultaneously ionize from multiple valence electronic states into different channels. Each ionization channel has a distinct angle-dependent ionization probability reflecting the nodal symmetries of the ionizing orbitals and other phenomena including electron correlations[34]. This attractive feature makes SFI in the MF an attractive tool for investigating valence electronic dynamics.

1.1.2 High harmonic generation

SFI can also trigger many interesting higher-order processes such as high harmonic generation (HHG) where photons (high-order harmonics of the fundamental) in the extreme ultraviolet (XUV) regime are generated following ionization events[35–37]. HHG can be understood in the framework of the three-step model[28,38]: (1) the electron is tunnel-ionized into the continuum, (2) the electron propagates in the laser field and gains energy, (3) when the electric field changes direction, the electron has a chance to come back, recombine with the parent ion, and emit a high energy photon. The emission of the XUV photon can occur twice in each optical cycle, and the tunneling happens most likely in a time interval of about 300 attoseconds near each field crest around the peak of the driving laser pulse[39]. The sub-cycle property makes both attosecond pulses and time-resolved measurements directly available in the HHG process[40]. Attosecond pulses generated by HHG can be used to investigate the dynamics of electrons[41]. The study of the HHG spectrum itself, called high-harmonic spectroscopy, can also reveal information about the molecular target and the photorecombination process with the advantage of accessing a wide spectral range simultaneously[42,43]. Angle-resolved high-harmonic spectroscopy can unfold features that are hard or impossible to observe in orientation-averaged measurements, such as the Cooper minimum and shape resonance of molecules[44–47], quantum interference and contributions from multiple orbitals[48,49], laser-induced modifications of the electronic structure of molecules[50], and coupled electronic and nuclear dynamics[51–54]. Molecular-frame high-harmonic spectroscopy is a unique and convenient way to measure the photoionization (angular) differential cross section (or photoionization transition dipole) across a wide spectral range[44,46,55,56], since photorecombination can be considered as the time reversal of photoionization where the same transition matrix elements are involved[57–59]. Molecular-frame HHG is a promising tool for time-, energy- and angle-resolved measurements, providing a lot of information to investigate the molecular structures, dynamics, and photoionization processes.

1.1.3 Ultrafast electron diffraction

Another widely-used class of tool for structural determination is diffraction, including ultrafast electron diffraction (UED), laser-induced electron diffraction (LIED), and x-ray diffraction techniques.

If electron diffraction is performed on an isotropic distribution of gas-phase molecules, the diffraction patterns will vary radially but not angularly. The diffraction pattern will consist of rings, and the intensity in each ring (radius) is isotropic[60]. For small molecules with only a few bond distances, the rings (maxima) can be well separated, and the bond lengths can be retrieved directly from the data by Fourier transforming the interference signal[61]. If all the bond lengths can be determined, the structure of the molecule can be reconstructed in principle. However, the difficulty in structural determination increases rapidly for bigger molecules with complex structures since many bond distances will overlap[62].

UED[63] for molecules in the gas phase has been making impressive progress for the last 20 years. The temporal resolution was improved from the picosecond (ps)[64–66] to the femtosecond (fs) time scale in both mega-electron-volt (MeV) relativistic[67] and tabletop kilo-electron-volt (keV) non-relativistic[68] electron beams. In time-resolved measurements where the rearrangement of atoms is of interest, the relation between the rearrangement and the change in electron signals with time is hard to correlate and interpret[69]. The retrieval of structural and dynamical information usually needs to be paired with a theoretical model containing a substantial prior understanding of the molecules[24,62].

The diffraction patterns of laser-aligned molecules are anisotropic[66], providing more information — both the atomic pairwise distances and the angles. The contrast between maxima and minima of the interference also increases with alignment[24]. These features enable the possibility of simultaneously extracting multiple bond lengths, allowing the retrieval of the two- and three-dimensional structure of polyatomic molecules directly without the need of fitting using a theoretical model[70,71]. Direct retrieval is important in probing transient states where the change in molecular structure is of interest. Direct retrieval makes the UED technique more powerful and convincing in general[62]. When the transient states of the molecules are induced by a laser pulse, the excitation can be a parallel or perpendicular transition and the distribution of the molecular axis is no longer isotropic[72,73]. Hence, studies of UED on aligned gas-phase molecules are important.

In 2009, Reckenthaeler *et al.* recorded UED patterns from transiently aligned molecules[66] for the first time. In this experiment, $C_2F_4I_2$ was dissociated by a 50 fs ultraviolet (UV) pulse and probed by a 2.3 ps electron pulse. The molecules preferentially dissociate along the C-I bond (along the laser polarization axis due to parallel transition) creating an anisotropic molecular distribution. On the picosecond time scale, Reckenthaeler *et al.* observed a strong anisotropic diffraction pattern at the beginning (between 0 ps and 1.7 ps), the fading of this anisotropy (between 3.3 ps and 5 ps), and an isotropic diffraction pattern after 8 ps. This observation reflects the deterioration of alignment due to molecular rotation. Later on, the alignment and structural changes of CS_2 molecules at different laser intensities were imaged using UED[74]. Recently, the evolution during a full rotational period of the N_2 rotational wave packet has been captured with temporal resolution in the hundreds of femtoseconds by Yang *et al.*[75] with a MeV UED setup (100 fs) and by Xiong *et al.*[68] with a 5 kHz tabletop keV UED setup (240 fs).

Progress has also been made in using UED to image the 3D structure of polyatomic molecules[70,71]. By using three diffraction patterns corresponding to different angular distributions, Hensley *et al.*[70] can retrieve the structure of isolated CF_3I molecules. By improving the spatiotemporal resolution to sub-ångström and femtosecond, these efforts have positioned UED of aligned gas-phase molecules as a powerful tool for observing the motion of each nucleus in 3D structural changes during molecular reactions from the initial to the final state[72,73,76–78].

1.1.4 Laser-induced electron diffraction

Instead of using an independent external electron beam like the conventional electron diffraction, LIED[79,80] uses the electron from a molecule to image the molecular target itself. LIED can also be understood by the three-step model similar to HHG as described before, but in the third step, the returning electron wave packet scatters elastically from its molecular parent ion instead of recombining. These electrons, called rescattered electrons, show up as high-energy electrons in the photoelectron spectrum and carry information about molecular structure.

However, since LIED happens in a strong oscillating laser field, it is necessary to remove the influence of the laser field on the electron spectra and extract the field-free electron-ion elastic differential cross section (DCS). The quantitative rescattering theory (QRS) by Lin *et al.*[57,81,82] has been used to show that this DCS can be retrieved from the angular distributions of the high-energy photoelectron spectrum. Experimentally, for LIED to resolve positions of atoms, the electron-ion recollisions need to be highly energetic and core-penetrating (small impact parameter) so that the effect of the valence electrons can be neglected[83]. These conditions can be realized in the laboratory by using midinfrared (MIR) wavelengths[83,84]. For electrons with energies on the order of 100 eV and at large angles (these electrons have sufficient momentum transfer), the independent atom model (and hence, the bond length retrieval method) used in conventional electron diffraction can be applied[85]. The retrieval could also be done on a spectrum at a fixed angle and varied rescattering momentum without prior structural information by using a Fourier transform method[86].

It is worth noting that LIED images the structure of the molecular ion instead of the neutral molecule. In combination with coincident detection, LIED is very useful for examining the dynamics of different ionization channels[25,87]. Compared to UED, LIED is also more sensitive to light atoms such as hydrogen[88], which is essential in many biological and chemical processes. Together with the development of high repetition rate MIR light sources[89], LIED has been emerging as a powerful imaging tool. Since the first experiment performed by Blaga *et al.*[84] in 2012, LIED has been used to successfully retrieve the static structures of many diatomic molecules such as O_2[84,88] and N_2[84,86], and polyatomic systems such as CS_2[90], OCS[91], C_2H_2[25,88], CF_3I[92], C_2H_4[93], C_6H_6[94], and C_{60}[95] with spatial resolution in picometers and temporal resolution from a few femtoseconds down to the sub-femtosecond range. Some ultrafast structural dynamics such as bond length contraction of O_2[84], the deformation of CS_2[90] and C_{60}[95], and the deprotonation of $C_2H_2^{2+}$[25,88] in strong laser fields, were also observed.

Similar to UED, simultaneous extraction of multiple bond lengths is also a challenge in LIED. Up to now, most of the LIED analyses were done by fitting based on a theoretical model, but this approach will not be applicable for large polyatomic systems since the parameter space will increase rapidly[69]. Direct retrieval using the Fourier transform method[86] has only been performed on small molecules[86,88] where, for example, three bond distances of C_2H_2[88] already show a significant convolution. LIED on aligned molecules will amplify the experimental interference patterns and, more importantly, allow the direct retrieval of 2D and 3D structure without a theoretical model. Additionally, the photoelectron signal in LIED is always nonisotropic. That is because two out of three steps in the three-step model — the tunnel ionization and the recollision processes — depend on the angle between the molecular axis and the laser polarization axis[29–31,96,97]. Moreover, the distribution of molecules can also be changed significantly before the ionization happens[31]. From their study of LIED on aligned CF_3I molecules, Krečinić *et al.*[92] also show evidence of the contribution from multiple orbitals to the photoelectron spectrum. Different orbitals have different angle-dependent ionization rates[32] and rescattering cross sections[96] and hence contribute differently[86,88,92]. Therefore, the investigation of LIED on aligned gas-phase molecules[25,87,92,98] is very crucial and unavoidable.

1.1.5 Ultrafast x-ray diffraction

X-ray diffraction has a much smaller DCS compared to electron diffraction (about 5 to 6 orders of magnitude less) and interacts more strongly with the electronic charge density cloud[11,99]. Because of the low cross section, x-rays penetrate deeper (longer mean free path) and are used to study proteins and other macromolecules[11]. Ultrafast x-ray diffraction has become feasible due to the development of the x-ray free-electron laser (XFEL)[23]. Similar to the problems in UED and LIED, ultrafast x-ray diffraction on aligned gas-phase molecules can boost the signal-to-noise ratio of the diffraction patterns and allow direct retrieval of structures in 2D and 3D. Many efforts have been carried out toward x-ray imaging of dynamics in the molecular frame[23,100–105].

1.2 Approaching molecular-frame measurements

In the previous section, we discussed the benefits of measurements in the MF. In this section, we briefly review the advantages and disadvantages of different methods for retrieving the MF observables. There are three main approaches: post-selection by coincident fragment imaging, preselection by alignment, and time-domain measurements from rotational wave packets.

1.2.1 Post-selection by coincident fragment imaging

If the physical or chemical processes of interest lead to the dissociation of molecules into charged fragments (for example, inner-shell photoionization of a molecule), coincident imaging can be used at a low count rate[22,106–108]. In these cases, the momenta of fragment ions and electrons from the same molecule are measured simultaneously. The momenta of fragment ions can be used to reconstruct the body frame of the molecule, called the recoil frame. If the dissociation is fast and along the bond axes, the recoil frame of the fragments will be a good representation of the MF. This method only applies to dissociative processes resulting in charged particles, and it requires multi-ion coincidences sufficient to determine the body frame of the molecule. Although this is a very powerful technique that is widely used, it precludes many important classes of experiments such as HHG, valence-shell ionization leaving a stable parent ion, and the excitation of neutral molecules. The reconstruction of the MF from the recoil frame also requires the axial recoil approximation (molecules dissociate along the bond axes) which can be questionable in many cases[109–114] and is often used without validation, as we will discuss in chapter 5.

1.2.2 Preselection by alignment

In the second approach, the molecules are first fixed in space, then the orientation of the probe pulse is varied to scan the angles between its polarization and the molecular axes. Initially, symmetric top molecules were oriented by using a hexapole electric field[115] and used in many stereochemistry experiments[116–118]. Later on, with the rapid development of the laser, it was noticed that molecules can be aligned along the polarization axis of the laser via the induced polarizability[119], and hence, laser pulses with moderate intensity below the ionization threshold can be used to align neutral molecules for further experiments[120–122]. In the beginning, the aligning laser pulses (in nanoseconds) were much longer than the rotational period of the molecules (in picoseconds). The molecules slowly rotate from the field-free states to reach maximum alignment at the peak of the laser pulse. After that, the alignment gradually reduces and the molecules return to the field-free states after the pulse is gone. This type of alignment, called adiabatic alignment, shows strong molecular axis confinement for various molecules including asymmetric tops[123–125]. However, the fact that the alignment happens during a strong laser field limits applications of the method, since the laser field can affect the process of interest and complicate the analysis.

With laser pulses much shorter than the rotational period of the molecules, which is typically in the 10–100 ps range, it is possible to align the molecules impulsively. The short alignment pulse induces a broadband rotational wave packet with the initial alignment observed shortly after the pulse is gone[126,127]. For linear molecules, this induced rotational wave packet is periodic, and the initial alignment will be revived after each rotational period. Alignment can also be observed at fractions (such as a half or a quarter) of the rotational period, and depending on the species, these alignments can be higher than the initial one[126,128]. Impulsive alignment provides an aligned molecular sample under the field-free condition, thus overcoming the limitations of adiabatic alignment. We will quantitatively discuss impulsive alignment in detail in chapter 2.

When the angular distribution of molecules is narrow, the LF approaches the MF. At the peak of the alignment, the relative orientation between the aligning pulse and the probe pulse is varied to sample different angles. This approach has been used to retrieve various angle-resolved quantities for linear molecules, such as the molecular-frame SFI probability[29,34,129,130], electron return probability after SFI[96], and transition dipole moments in HHG experiments[44]. In practice, perfect alignment (i.e., all molecules are confined to one orientation) requires an infinite range of high angular momentum and thus is not possible, hence, in almost all cases, we need to separate the molecular axis distribution from the LF data and extract the angle dependence of ionization in the MF[29,34,44,96,129–131]. However, the fitting procedure for deconvolution is sensitive noise and results can be inconsistent[29,129,131]. We will extensively address one problem of this kind in chapter 4.

This approach becomes a lot more challenging when applied to asymmetric top molecules because the angle dependence now involves two Euler angles (see Fig. 2.1, this will be more clear in chapter 2). The method requires the field-free 3D alignment of the molecules[132–135] and the ability to orient the laser polarization in any arbitrary direction. Neither of these is trivial. Furthermore, unlike the case of linear molecules, the induced rotational wave packet of symmetric top molecules is not periodic (we will explain why in section 2.1 of chapter 2), hence, there is no well-defined single alignment peak. It is not clear how different distributions can affect the retrieval process.

1.2.3 Time-domain measurements from rotational wave packets

Another approach to the MF, based on Rotational Coherence Spectroscopy (RCS)[136], is from time-domain measurements. In this case, we launch a rotational wave packet using a non-resonant laser pulse (impulsive alignment). This wave packet evolves in a field-free environment after the aligning pulse, and a LF observable is measured as a function of the pump-probe delay. While the polarizations of the aligning pump pulse and the ionizing probe pulse are identical and stay fixed, the molecules sweep over all possible angles between the probe polarization and the molecular axis as the rotational wave packet evolves. Assuming the molecular structure is known, it is possible to retrieve the angle-dependence of the photochemical processes by fitting to the LF delay-dependent data[30,31,46,137–142].

The time-domain approach has been used to retrieve the angle-resolved SFI probability of linear[97,137,141] and symmetric-top[142] molecules, and high-harmonic[46,138,143] and molecular-frame photoelectron angular distributions[140] of linear molecules. Notably, Makhija *et al.*[144] demonstrated that, for asymmetric top molecules, this approach provides access to the dependence of ionization on both relevant angles. They retrieved the angle-dependent SFI of C_2H_4, an asymmetric top molecule, from the measurement of ion yield as a function of pump-probe delay where the pump aligns and the probe ionizes the molecules. This time-domain approach, called Orientation Resolution through Rotational Coherence Spectroscopy (ORRCS)[144], has many attractive advantages that can be exploited in other applications. We will describe the basic idea, advantages, and challenges of ORRCS in detail in section 2.2 of chapter 2.

1.3 Structure of this dissertation

The main theme of this dissertation is retrieving the angle dependence of several important light-matter interaction processes, such as strong-field ionization, few-photon ionization, and dissociation, by the time-domain approach. We follow the same pump-probe scheme in all the experiments: a non-resonant pump pulse will impulsively align the molecules, launching a broadband rotational wave packet, and a probe pulse that comes at a later time will induce the process of interest (ionization, dissociation). We measure the LF observable (ion yield, momentum distribution of ions and electrons) as a function of the pump-probe delay when the rotational wave packet evolves under field-free conditions after the aligning pulse is gone. From these time-domain measurements, we then extract the angle dependence of the observable using ORRCS. In chapter 2, we provide a detailed, quantitative discussion on all the necessary fundamentals of impulsive alignment and ORRCS. And in chapter 3, we describe the realization of these ideas in our laboratory, including the light sources, the optical layout of the experimental setup, the generation of cold molecules, the measurement and analysis of data, etc. Information in these two chapters is essential for understanding the work described in later chapters.

In chapter 4, we discuss the retrieval of the angle-dependent strong-field ionization of CO_2 (a linear molecule) and SO_2 (an asymmetric top molecule). We address the discrepancies between previous experiments and theories on CO_2, while the work on SO_2 gives more experimental evidence on asymmetric top molecules and can help to understand other experiments, since SO_2 has been used extensively as a test system. We systematically test the stability and sensitivity of the ORRCS retrieval algorithm with various parameters through different statistical analyses to determine the appropriate size of the fitting model. We also perform independent experiments to check the consistency of the retrieval.

In chapter 5, we expand the time-domain approach to momentum measurements. With this new development, we show that the axial recoil approximation can be validated by measuring the momentum distributions of the fragment ions as a function of pump-probe delay. Specifically, we study the dissociation of CO_2 by a strong 800 nm laser pulse and the dissociation of N_2 by a 262 nm pulse. We show how the dissociation depends on the initial orientation of the molecule and inspect the effect of the laser field on the final distributions of the fragment ions.

In chapter 6, we present another application of ORRCS for momentum measurements in the photoionization of molecules. We use the framework developed in chapter 5 to retrieve the orientation-resolved photoelectron angular distributions of N_2, CO_2, and C_2H_4 in the few-photon ionization regime. We also compare few-photon ionization with single-photon ionization and strong-field ionization to enrich our knowledge in this regime, which is not very well understood.

Chapter 7 provides a summary of the presented works and our outlook into the future. We believe that many areas of ultrafast physics and chemistry can gain valuable insights by applying the method developed in this dissertation. We share a few ideas of this kind. Some of them have already been under investigation in our laboratory, others are only vaguely sketched awaiting a more complete picture in the future.

Chapter 2

Theoretical fundamentals on impulsive alignment and Orientation Resolution through Rotational Coherence Spectroscopy

We begin this chapter by classifying molecular rotors into different types based on their inertia tensor. Throughout this dissertation, we will work with linear (N_2, CO_2) and asymmetric top (SO_2, C_2H_4) molecules. After defining the frames and angles, we then focus our discussion on how the impulsive alignment of molecules works and how to apply the Orientation Resolution through Rotational Coherence Spectroscopy to retrieve the angle-resolved observable from the delay-dependent measurements on the rotational wave packet. We use the semi-classical model where molecules are treated as quantum rigid rotors and the electric field is described classically. In each section, we write down the expressions for linear molecules first and for asymmetric top molecules later. Although the general ideas in both cases are very similar, the technical details are different with some issues arise from the involvement of more angles for asymmetric top molecules.

2.1 Impulsive molecular alignment

2.1.1 Classification of molecular rotors

Depending on the symmetry of the molecules, we can classify them into different categories as linear, spherical top, symmetric top, and asymmetric top molecules as shown in Table 2.1. This is based on three components I_A, I_B, I_C of the moment of inertia tensor about three principal axes A, B, C, with the center of mass as the origin (conventionally, $I_A \leq I_B \leq I_C$).

Table 2.1: *Classification of molecular rotors*

Molecules	Relation	Examples
Linear	$I_A \approx 0 \ll I_B = I_C$	N_2, O_2, CO_2
Spherical top	$I_A = I_B = I_C$	SF_6, CCl_4, CH_4
Symmetric top		
• Prolate top	$I_A < I_B = I_C$	CH_3I
• Oblate top	$I_A = I_B < I_C$	C_6H_6
Asymmetric top	$I_A < I_B < I_C$	SO_2, C_2H_4

If molecules are considered as rigid rotors, the Hamiltonian for free rotations will be

$$H_0 = \frac{J_A^2}{2I_A} + \frac{J_B^2}{2I_B} + \frac{J_C^2}{2I_C} = AJ_A^2 + BJ_B^2 + CJ_C^2, \tag{2.1}$$

where J_i $(i = A, B, C)$ are angular momentum operators and A, B and C are the rotational constants about each principal axis (A, B, C). In this dissertation, we treat molecules as rigid rotors, although for linear molecules, we do add a term to correct for the centrifugal distortion.

2.1.2 Definitions of the molecular frame and the laboratory frame

In laser-induced alignment of molecules, we use the laser field to confine one or more molecular axes along laboratory fixed axes. We will use two frames of reference to depict the relative orientation and the rotation of the molecules in the laser field: the molecular frame (xyz) and the laboratory frame (XYZ).

The molecular frame (MF) is defined by three principal axes of the polarizability tensor with the z axis as the most polarizable axis and the x axis as the least polarizable one. For small molecules with high internal symmetries such as N_2, CO_2, C_2H_4 and SO_2 that we will consider in this dissertation, the principle axes of the polarizability tensor coincide with the principle axes of the inertia tensor.

The laboratory frame (LF) is defined by the polarization state of the laser field. For linearly polarized pulses, the LF Z-axis is the polarization axis and the LF Y-axis is the propagation axis. For circularly polarized pulses, on the other hand, the LF Z-axis is normally defined as the propagation axis and the LF Y-axis is parallel to the detector plane, which basically swaps the definitions compared to the case of linear polarization. The detector plane is parallel to both the Y and Z axes, as we will describe more in chapter 3.

The two frames are connected by a rotation through the three Euler angles θ, ϕ, and χ[145] (see Fig. 2.1(a)). θ is the polar angle between the Z and z axes, ϕ is the azimuthal angle about the Z axis measuring the angle between the X axis and the projection of the z axis on the XY plane, and χ is the azimuthal angle about the z axis measuring the angle between the x axis and the projection of the Z axis on the xy plane. With these three angles (ϕ, θ, χ), we can make the two frames coincide by rotating one into the other and vice versa by using the Euler rotations[145]. Any orientation of the molecule in the LF can be described by ϕ, θ and χ.

From the MF perspective (see Fig. 2.1(b)), the angles ϕ, θ, and χ define the orientation of the laser field. If the laser field has cylindrical symmetry about the Z axis then ϕ will be irrelevant since all values of ϕ will be equivalent. In that case, we would need two Euler angles θ and χ to describe the angle dependence of a physical process that happens with asymmetric top molecules. If the molecule is also linear, as in Fig. 2.1(c), then the rotation about χ is also physically irrelevant since all χ are equivalent. The angle dependence of a process will depend only on the angle θ between the molecular axis and the laser polarization axis.

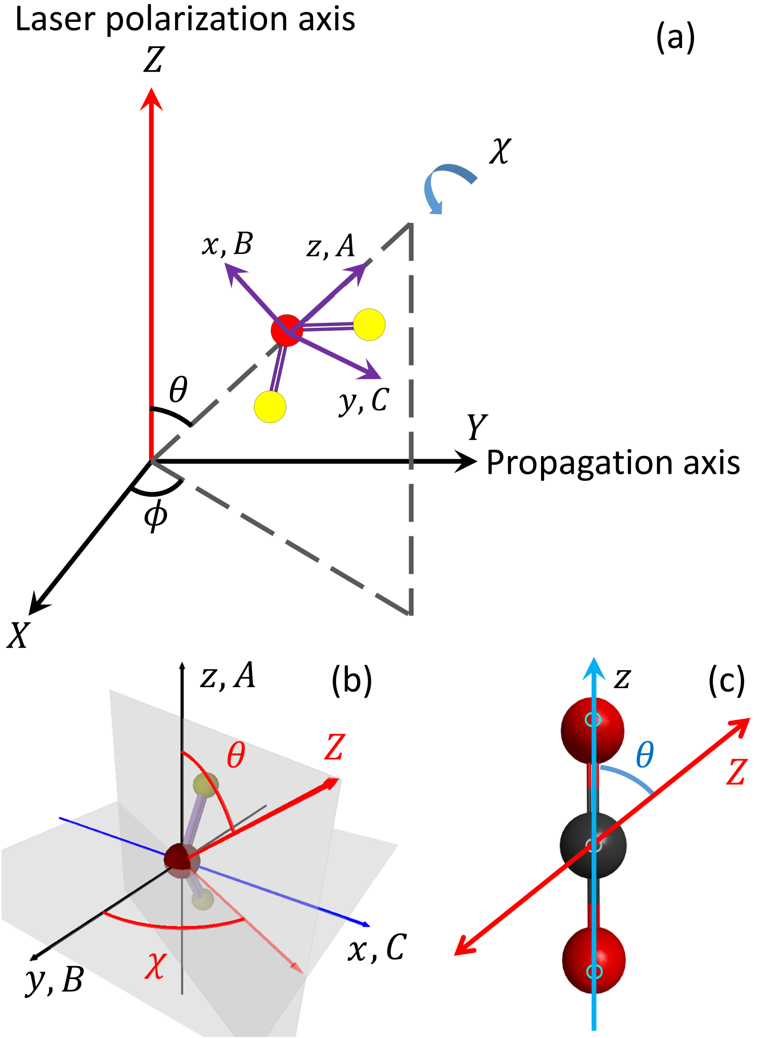

Figure 2.1: *Definitions of frames and angles. (a) The MF xyz and the LF XYZ are connected by three Euler angles ϕ, θ and χ. From the MF perspective, the angles ϕ, θ, and χ define the orientation of the laser field. (b) If the laser field has cylindrical symmetry about the Z axis then ϕ will be irrelevant. (c) If the molecule is also linear, then the rotation about χ is also physically irrelevant.*

2.1.3 Rotational states of the field-free Hamiltonian

In this section, we discuss the rotational states of the molecules in the absence of the laser field. The rotational states are simultaneous eigenfunctions of the field-free rotational Hamiltonian H_0 in Eq. (2.1), the square of the total angular momentum J^2, and the projection of the total angular momentum on the LF Z-axis J_Z. In the next section, we will use these rotational states as the basis for the in-field calculation and use their energy levels in the discussion on the time evolution of the rotational wave packet induced by the laser field.

Linear molecules

For linear molecules ($I_A \approx 0 \ll I_B = I_C$), there is only one distinct value of the angular momentum component so the rotational Hamiltonian can be written in terms of the total angular momentum J^2 as $H = BJ^2$. The rotational states are, therefore, the angular momentum eigenfunctions $|JM\rangle$, where J is the total angular momentum quantum number and M is the projection of J on the LF Z-axis. In the real angular space, the rotational states $|JM\rangle$ are represented by the spherical harmonics $Y_{JM}(\theta, \phi)$ as $\langle \theta, \phi | JM\rangle = Y_{JM}(\theta, \phi)$. The energy of a rotational state $|JM\rangle$ only depends on J as $E = J(J+1)B$.

Symmetric top molecules

For symmetric top molecules, $A = B$ and $J_A = J_B$ if the top is prolate, $B = C$ and $J_B = J_C$ if the the top is oblate. We will write down in detail the solution for prolate symmetric top molecules. An equivalent can be written for oblate symmetric top molecules without any difficulties. Because two component angular momenta are identical, the rotational Hamiltonian can be expressed in terms of the total angular momentum J and one of the components, say, J_A as $H_0 = AJ_A^2 + B(J^2 - J_A^2) = BJ^2 + (A - B)J_z^2$ ($z \equiv A$ since the inertia and the polarizability tensors coincide). Hence, the rotational states now need to be simultaneous eigenfunctions of J^2, J_Z and J_z.

The identicality of the other two component angular momenta makes the last component angular momentum (about the axis with highest internal symmetry) a constant of motion (see Euler's Equations for a free top[146]), thus, the projection of the total angular momentum on the MF z-axis is conserved. The rotational states are then denoted as $|JKM\rangle$, where where K is the projection of the angular momentum onto the MF z-axis. J, K and M are all conserved. In the real angular space, these symmetric top rotational states are

$$\langle \phi, \theta, \chi | JM\rangle = \sqrt{\frac{2J+1}{8\pi^2}} D_{MK}^{J\star}(\phi, \theta, \chi), \tag{2.2}$$

where $D_{MK}^{J}(\phi, \theta, \chi)$ are Wigner-D functions (see, for example, page 104 of Zare[145] for a derivation). The energy of a prolate symmetric top rotational state $|JKM\rangle$ only depends on J and K as $E = BJ(J+1) + (A-B)K^2$. For an oblate symmetric top, C is the axis with highest internal symmetry, and the energy level is $E = BJ(J+1) + (C-B)K^2$.

Asymmetric top molecules

Similarly, for asymmetric top molecules, the rotational states must be the simultaneous eigenfunctions of J^2, J_Z and H_0. However, now, H_0 needs to be represented by J^2 and two of the component angular momenta, say, for example, J_z and J_x. J_z and J_x do not commute with each other and H_0 does not commute with any component of the angular momentum in the MF axes (J_x, J_y, J_z). The eigenvectors of the field-free Hamiltonian for asymmetric top molecules do not have an analytical form[146]. However, since H_0 still commutes with J^2 and J_Z, J and M are still good quantum numbers (conserved). In the symmetric top $|JKM\rangle$ representation, H_0 will be block diagonal (block of different K for each J and M). We can write these eigenvectors as a linear combination of the $|JKM\rangle$ as

$$|J\tau M\rangle = \sum_K c_K \, |JKM\rangle, \tag{2.3}$$

where τ, running from $-K$ to K, is not a good quantum number and is used as an index of increasing energy levels. Diagonalization of H_0 will give values of the coefficients c_K determining the rotational states and the energy levels. Rotational states and energy levels for different types of molecules are summarized in Table 2.2.

Table 2.2: *Rotational states and energy levels for different types of molecules*

Molecules	Rotational state	Energy level
Linear	$\|JM\rangle$	$BJ(J+1)$
Symmetric top		
• Prolate top	$\|JKM\rangle$	$BJ(J+1)+(A-B)K^2$
• Oblate top	$\|JKM\rangle$	$BJ(J+1)+(C-B)K^2$
Asymmetric top	$\|J\tau M\rangle = \sum_K c_K \, \|JKM\rangle$	

2.1.4 Rigid rotors in an external electric field

The molecules can be aligned by a moderately intense non-resonant laser pulse due to the interaction between the polarizability of the molecules and the laser field[17,19,127,147]. This interaction V is well portrayed within the dipole approximation[148] as

$$V(t) = -\boldsymbol{\mu}\cdot\mathbf{E}(\mathbf{t}). \tag{2.4}$$

The electric dipole moment of the molecule $\boldsymbol{\mu}$ can be expanded as a power series of the electric field $\mathbf{E}(\mathbf{t})$ as

$$\boldsymbol{\mu} = \boldsymbol{\mu}_0 + \frac{1}{2}\boldsymbol{\alpha}\mathbf{E}(\mathbf{t}) + \frac{1}{6}\boldsymbol{\beta}\mathbf{E}^{\mathbf{2}}(\mathbf{t}) + ..., \tag{2.5}$$

where $\boldsymbol{\mu}_0$ is the permanent dipole moment, $\boldsymbol{\alpha}$ is the polarizability tensor of rank 2, and $\boldsymbol{\beta}$ is the hyperpolarizability tensor of rank 3.

The fast oscillating electric field changing direction every half cycle will average out the contributions from the permanent dipole and the hyperpolarizability, letting the polarizability determine the interaction. Therefore, $\boldsymbol{\alpha}$ is sufficient for modeling alignment. $\boldsymbol{\beta}$ will play an important role if orientation is of interest, since in that case one needs to break the symmetry of the electric field[149,150].

In impulsive alignment of molecules, the duration of the alignment laser pulse τ (typically from tens to hundreds of femtoseconds) is much shorter than the rotational period of the molecules $\mathrm{T_{rot}}$ (typically from tens to hundreds of picoseconds) ($\tau \ll \mathrm{T_{rot}}$), and, in most cases, much longer than one cycle of the electric field (multicycle pulse, $\tau \gg 2\pi/\omega$). $\mathrm{T_{rot}} \gg \tau$ means the molecules do not move during the alignment pulse, $\tau \gg 2\pi/\omega$ means the alignment pulse is multicycle and the carrier envelope phase is not important, hence, the interaction potential can be cycle-averaged assuming the envelope varies slowly. $\mathrm{T_{rot}} \gg \tau \gg 2\pi/\omega$ also implies that the wavelength (and also the chirp) of the alignment pulse is irrelevant as long as there are no resonances. Effectively, the molecules only see the envelope of the alignment pulse.

Linear molecules

The electric field $\mathbf{E(t)}$ of a linearly polarized laser pulse can be written as

$$\mathbf{E(t)} = E_0(t)\cos\omega t\hat{\mathbf{Z}}, \tag{2.6}$$

where $E_0(t)$ is the envelope of the field and ω is the central frequency of the pulse. For linear molecules, due to the cylindrical symmetry of the molecule about the bond axis (molecular axis), the polarizability tensor can be described with two components parallel ($\alpha_\parallel$) and perpendicular ($\alpha_\perp$) to the internuclear axis as

$$\boldsymbol{\alpha} = \begin{pmatrix} \alpha_\parallel & 0 & 0 \\ 0 & \alpha_\perp & 0 \\ 0 & 0 & \alpha_\perp \end{pmatrix}. \tag{2.7}$$

Substituting the equations for $\mathbf{E(t)}$ and $\boldsymbol{\alpha}$ into Eq. (2.4), and averaging over one cycle, the interaction potential will be

$$V(t) = -\frac{E_0^2(t)}{4}\Delta\alpha\cos^2\theta + \alpha_\perp, \tag{2.8}$$

where $\Delta\alpha = \alpha_\parallel - \alpha_\perp$ is the polarizability anisotropy and θ is the angle between the molecular axis and the laser polarization axis. In fact, $\alpha_\perp$ is just a constant offset and can be dropped. This potential has minima at 0° and 180° leading to the alignment of the molecules along the laser polarization axis, and the maximum at 90° leads to the anti-alignment in the plane perpendicular to the laser polarization axis.

The alignment pulse applies a torque

$$-\frac{\partial V(\theta,t)}{\partial\theta} = \Delta\alpha\frac{E_0^2(t)}{4}\sin 2\theta, \tag{2.9}$$

and transfers angular momentum to the molecules[151]. The torque is zero at $\theta = 0°$ and is maximum at $\theta = 45°$. Molecules parallel to the laser field ($\theta = 0°$) experience no torque and do not rotate, while molecules at an angle with the laser field ($\theta \neq 0°$) experience a torque and rotate towards the laser polarization direction. For small angle θ, the torque is nearly proportional to θ since $\sin 2\theta \approx 2\theta$, hence, the angular velocity that the molecule gained from the laser pulse is nearly proportional to the initial angle. Expressing this impulsive approximation in the form of Newton's second law for angular momentum, we have $\Delta J = \text{torque} \cdot \Delta t$. This explains why impulsive alignment only depends on the laser fluence (pulse intensity times duration, or physically, optical energy per unit area). As long as both alignment pulses are impulsive and have the same fluence, a pulse of higher intensity and shorter duration will have the same alignment effect as a pulse of lower intensity but longer duration.

When the angle θ is larger, the torque is stronger, and the molecule rotates faster. Many molecules reach $\theta \approx 0°$ at nearly the same time, forming an initial alignment distribution assuming the angular velocity the molecule gained from the pulse is much higher than its initial velocity (or $\Delta J \gg J_T$, where J_T is the angular momentum from the initial thermal distribution). This initial alignment can be seen as a peak in Fig. 2.2 at time $t = 0$. Here, for demonstration purposes, the time axis has been shifted so that $t = 0$ is the peak of the initial alignment distribution, not the peak of the alignment pulse (270 fs earlier). Elsewhere, $t = 0$ is defined by the peak of an alignment laser pulse unless otherwise stated. For a 100 fs alignment pulse, we can see that the initial alignment happens after the pulse is gone.

During the pulse, the rotational dynamics of an isolated molecule are governed by the time-dependent Schrödinger equation (TDSE)

$$i\partial_t \left|\psi(t)\right\rangle = \left[H_0 + V(t)\right] \left|\psi(t)\right\rangle . \tag{2.10}$$

This TDSE can be solved in the rotational states basis $|JM\rangle$ where $|JM\rangle$ are the spherical harmonics in real space. Since M is conserved because of the cylindrical symmetry of the linearly polarized laser field about the laser polarization axis, the induced broadband rotational wave packet $|\psi(t)\rangle$ is expanded as

$$|\psi(t)\rangle = \sum_{J} C_{JM}(t)\,|JM\rangle\,, \tag{2.11}$$

where the coefficients $C_{JM}(t)$ are time-dependent. Substituting $|\psi(t)\rangle$ into the TDSE, we obtain the equation that determines $C_{JM}(t)$ as

$$i\partial_t C_{JM}(t) = -iC_{JM}(t)BJ(J+1) + i\frac{E_0^2(t)}{4}\Delta\alpha \sum_{J'} C_{J'M}\,\langle JM|\cos^2\theta\,|J'M\rangle. \tag{2.12}$$

This differential equation is solved numerically using a Runge-Kutta method with adaptive step size as described in detail previously[144,152]. The code is written in C++ using OpenMP to run the calculations for different values of M in parallel. An array of coefficients $C_{JM}(t)$ is obtained at each time step. The selection rules for $\cos^2\theta$ in the second term on the right hand side of Eq. (2.12) show that the alignment pulse populates each initial rotational state $|J_0M_0\rangle$ to higher rotational states with the selection rules $\Delta J = 0, \pm 2$ and $\Delta M = 0$ via Raman transitions.

After the pulse is gone, this rotational wave packet continues to evolve under field-free condition as

$$|\psi(t)\rangle = \sum_{J} C_J(t_e)\,|JM\rangle \exp(-iE_J t), \tag{2.13}$$

where the coefficients $C_J(t_e)$ are now time-independent constants with t_e as the end time of the alignment pulse. For linear molecules, since the energy levels of higher rotational states are integer multiples of the ground state energy level, $E_J = 2\pi BJ(J+1)$, the rotational wave packet will show periodic structures with time. The features that appear at time t will be repeated at later time $t + nT_{rot}$ where n is an integer. These repeating patterns are called revivals of alignment[126]. Fig. 2.2 shows that the initial alignment peak is revived after each rotational period ($t = T_{rot}, 2T_{rot}, 3T_{rot}$). This is called full revivals. We can also observe fractional revivals at $t = \left(n + \frac{1}{2}\right) T_{rot}$ (half revivals), $t = \left(n + \frac{1}{4}\right) T_{rot}$ or $t = \left(n + \frac{3}{4}\right) T_{rot}$ (quarter revivals).

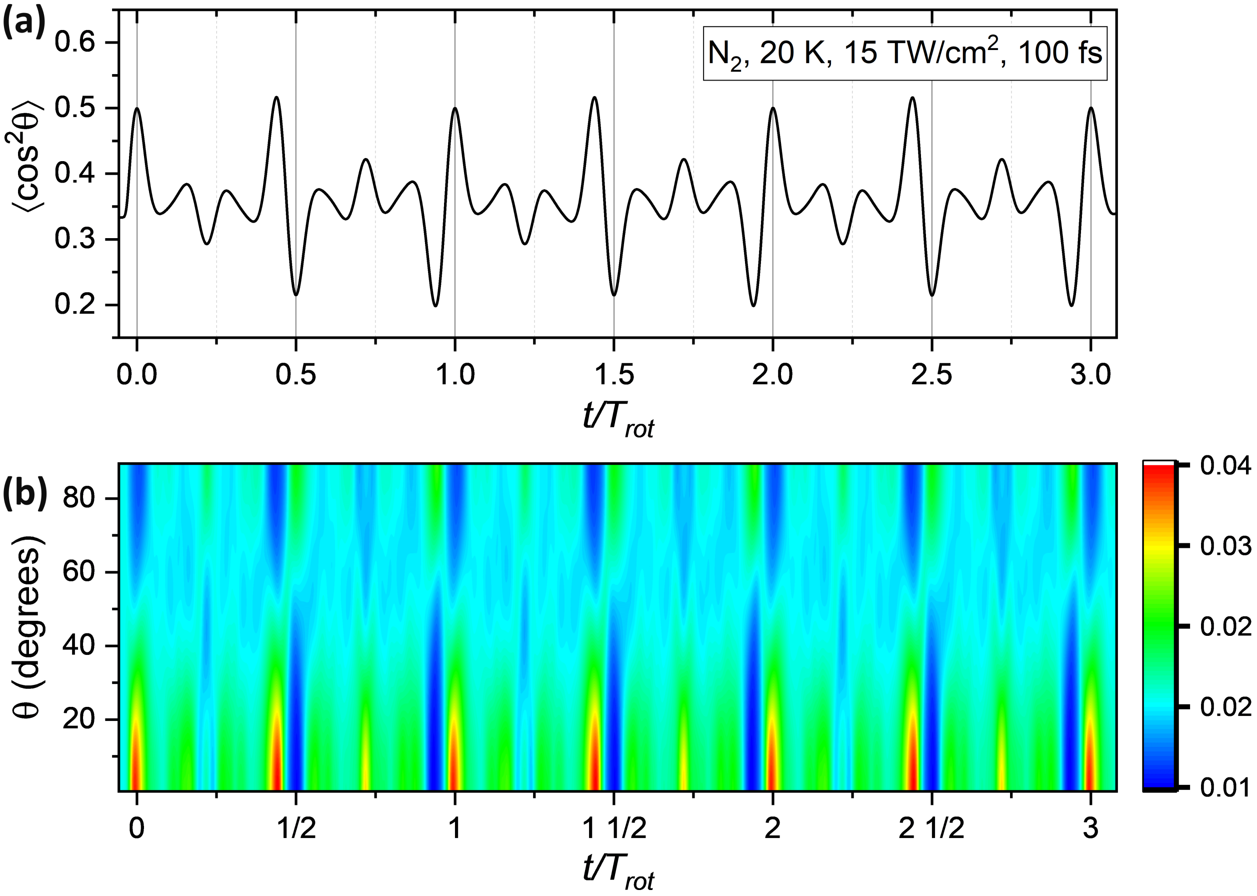

Figure 2.2: *In impulsive alignment, after the aligning pulse is gone, the wave packet evolves with time periodically, repeating its structures after each rotational period. This can be observed in both the $\langle\cos^2\theta\rangle$ of the distribution (a) or in the full distribution of the molecular axis (b). The initial alignment peak at $t = 0$ is revived after each rotational period ($t = T_{rot}, 2T_{rot}, 3T_{rot}$). These are called full revivals. We can also observe fractional revivals at $t = \left(n + \frac{1}{2}\right) T_{rot}$ (half revivals), $t = \left(n + \frac{1}{4}\right) T_{rot}$ or $t = \left(n + \frac{3}{4}\right) T_{rot}$ (quarter revivals). Note that the time axis has been shifted so that $t = 0$ is the peak of the initial alignment distribution, not the peak of the alignment pulse. The initial alignment peak comes 270 fs after the peak of the alignment pulse.*

Because the thermally populated initial states are incoherent, we calculate the time evolution of each initial state $|J_0M_0\rangle$ separately and then weight them with their nuclear spin degeneracies g_{J_0} and the Boltzmann distribution. The weighting factor $w_{J_0M_0}$ can be written as

$$w_{J_0M_0} = g_{J_0} \frac{e^{-BJ_0(J_0+1)/k_BT}}{\sum_{J_0} e^{-BJ_0(J_0+1)/k_BT}}, \tag{2.14}$$

where k_B is the Boltzman constant. Under our experimental conditions of ultrahigh vacuum ($10^{-10} - 10^{-11}$ Torr) and low temperature (a few K), this approach has been working well for many cases[30,31,46], giving equivalent results to the density matrix approach[19]. In other cases, such as when the molecular alignment is affected by collisional relaxations in a high-density environment[153,154], the density matrix approach of solving the Liouville–von Neumann equation should be used to describe the dynamics[155].

Conventionally, the degree of alignment of the rotational wave packet is measured by $\langle \cos^2\theta \rangle$ (or, equivalently, the second-order moment) of the distribution. $\langle \cos^2\theta \rangle$ is a good measure of alignment since it has the property of being 0 for perfect anti-alignment and 1 for perfect alignment distribution. For an isotropic distribution, the degree of alignment is

$$\langle \cos^2\theta \rangle = \frac{1}{2\pi} \int_0^{\pi} \cos^2\theta \sin\theta d\theta \int_0^{2\pi} d\phi = 1/3. \tag{2.15}$$

$\langle \cos^2\theta \rangle$ is typically the most dominant moment in describing the anisotropy of a distribution. $\langle \cos^2\theta \rangle$ can explain many experiments where observables are not sensitive to higher order moments such as the Kerr effect or single-photon ionization[156], and of course, where distributions are $\cos^2\theta$ or $\sin^2\theta$ such as single photon excitation[73].

However, it is important to realize that the complete angular distribution of the rotational wave packet is characterized by all axis distribution moments $\langle P_K(\cos\theta) \rangle (t)$ where $P_K(\cos\theta)$ are the Legendre polynomials. To explain this, we first start by expanding the molecular axis distribution in the spherical harmonic basis

$$\rho(\theta, \phi, t) = \sum_{K,Q} A_{K,-Q}(t) Y_{K,Q}(\theta, \phi), \tag{2.16}$$

where $A_{K,-Q}(t)$ are called the time-dependent axis distribution moments[156]. Multiplying both sides of Eq. (2.16) with $Y^{\star}_{K',Q'}(\theta, \phi)$ and integrate over the solid angle $d\Omega = \sin\theta d\theta d\phi$, we have

$$\int \rho(\theta, \phi, t) Y^{\star}_{K',Q'}(\theta, \phi) d\Omega = \sum_{K,Q} A_{K,-Q}(t) \int Y_{K,Q}(\theta, \phi) Y^{\star}_{K',Q'}(\theta, \phi) d\Omega, \tag{2.17}$$

or equivalently,

$$\langle Y^{\star}_{K',Q'}(\theta,\phi)\rangle(t) = \sum_{K,Q} A_{K,-Q}(t)\delta_{K,K'}\delta_{Q,Q'}. \tag{2.18}$$

We can see that the axis distribution moments are basically the expectation values of the spherical harmonics $A_{K,-Q}(t) = \langle Y^{\star}_{K',Q'}(\theta,\phi)\rangle(t) = (-1)^Q\langle Y_{K,-Q}(\theta,\phi)\rangle(t)$. In the case of a linear molecule and linear polarization that we are considering, there is no dependence on ϕ, spherical harmonics reduce to Legendre polynomials, and the axis distribution moments become expectation values of the Legendre polynomials ($\langle P_K(\cos\theta)\rangle(t)$) with a scale factor

$$A_K(t) = \sqrt{\frac{2K+1}{4\pi}}\langle P_K(\cos\theta)\rangle(t), \tag{2.19}$$

where we can always absorb this scale factor into the $A_K(t)$ themselves. In many experiments, such as multiphoton ionization or strong-field ionization[31], the probes are sensitive to higher order moments of the distribution and $\langle\cos^2\theta\rangle$ will not be adequate to explain the results. An understanding of the full rotational wave packet is needed.

If the laser field is circularly polarized, the axis of symmetry is the laser propagation direction rather than the polarization direction. It is natural to describe the relative orientation through the angle β between the molecular axis and the electric field propagation vector $\vec{k}$[33,157,158]. In the frame described in Sec. 2.1.2, the electric field can be written as

$$\mathbf{E}(\mathbf{t}) = E_0(t)\left(\cos\omega t\hat{\mathbf{X}} + \sin\omega t\hat{\mathbf{Y}}\right), \tag{2.20}$$

and the interaction potential would be

$$V(t) = \frac{E_0^2(t)}{4}\Delta\alpha\cos^2\beta. \tag{2.21}$$

This potential has a minimum at $\beta = 90°$ leading to the alignment of the molecules in the plane perpendicular to the propagation axis (planar alignment). On the other hand, the anti-alignment at $\beta = 0°$ and $\beta = 180°$ (maxima of the potential) lead to molecules along the propagation axis k, called $k-$alignment[157].

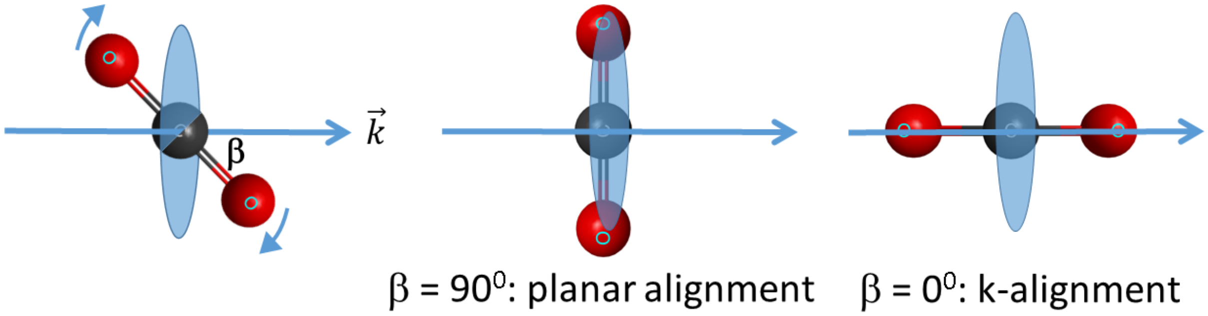

Figure 2.3: *Definition of angle: For circular polarization, the axis of symmetry is the laser propagation direction rather than the polarization direction. In this case, it would be best to describe the relative orientation through angle* β *between the molecular axis and the electric field propagation vector* $\vec{k}$[33,157,158]. *In order to avoid confusion with the linearly polarized case, we use the symbol* β *for the polar angle between the molecular axis and the propagation vector* $\vec{k}$. *When* $\beta = 0°$, *the molecules are along* $\vec{k}$, *we have k-alignment; when* $\beta = 90°$, *the molecules are in the plane perpendicular to* $\vec{k}$, *and we have planar alignment*[157].

Asymmetric top molecules

The polarizability tensor of asymmetric top molecules has three distinct components along the three principle axes

$$\boldsymbol{\alpha} = \begin{pmatrix} \alpha_{xx} & 0 & 0 \\ 0 & \alpha_{yy} & 0 \\ 0 & 0 & \alpha_{zz} \end{pmatrix}. \tag{2.22}$$

In a linearly polarized laser field, we can substitute this polarizability $\boldsymbol{\alpha}$ and the electric field $\mathbf{E(t)}$ from Eq. (2.6) into Eq. (2.4) and average over one cycle to obtain the interaction potential as

$$V(t) = -\frac{E_0^2(t)}{4\sqrt{6}}\left[\alpha_0^2\left(\frac{3}{2}\cos^2\theta - 1\right) + \alpha_2^2\sqrt{\frac{3}{2}}\sin^2\theta\cos 2\chi\right], \tag{2.23}$$

where $\alpha_0^2 = \left[2\alpha_{zz} - (\alpha_{xx} + \alpha_{yy})\right]/\sqrt{6}$ and $\alpha_2^2 = (\alpha_{xx} - \alpha_{yy})/2$. This interaction potential depends on both Euler angles θ and χ. Therefore, in this case, a linearly polarized laser pulse does not only induce the typical "1D alignment" (dependence on one angle), but creates anisotropic distributions of the molecular axis in both angles θ and χ. With a proper method, as we will discuss in section 2.2, we will be able to retrieve the fully angle-resolved observables (for example, ionization probability) of asymmetric top molecules depending on both Euler angles.

The TDSE for asymmetric top molecules can be solved by writing the rotational wave function as

$$|\psi(t)\rangle = \sum_{J'K'} C_{J'K'}(t)\, |J'K'M\rangle\,, \tag{2.24}$$

where M is conserved because of the cylindrical symmetry about the laser polarization axis. By substituting this into the TDSE and projecting onto a particular $|JKM\rangle$ state, we will have a differential equation that determines the expansion coefficients

$$i\partial_t C_{JK}(t) = \sum_{J'K'} \left[C_{J'K'}(t)\langle JKM|H_{rot}|J'K'M\rangle\delta_{JJ'} + C_{J'K'}(t)\langle JKM|V(t)|J'K'M\rangle \right]. \tag{2.25}$$

This has an advantage that the Hamiltonian can be written down analytically in the symmetric top basis. We can rewrite the interaction potential in terms of Wigner-D rotation matrices as

$$V(t) = -\frac{E_0^2(t)}{4\sqrt{6}} \left\{ \alpha_0^2 D^2_{0,0}(\chi,\theta,\phi) + \alpha_2^2 \left[D^2_{0,2}(\chi,\theta,\phi) + D^2_{0,-2}(\chi,\theta,\phi) \right] \right\}, \tag{2.26}$$

The interaction term now becomes an integral over products of three rotation matrices and can be calculated with the Clebsch-Gordan coefficents by using Eq. (3.118) in Zare[145]. Without evaluating the details, the selection rules of the rotation matrices products can already tell us that a linearly polarized laser pulse will excite coherences between states with $\Delta J = 0, 1, 2$, $\Delta K = 0, 2$, and $\Delta M = 0$.

After the aligning pulse is gone, we transform the wave packet back into the asymmetric top basis $|J\tau M\rangle$ and propagate it under field-free conditions. Because the energy levels of asymmetric top molecules are not regularly spaced (see Sec. 2.1.3), the rotational wave packet is not periodic. However, some approximate revivals corresponding to some energy subsets can be identified[136]. We list these revivals for prolatelike asymmetric top molecules (SO_2, C_2H_4) considered in this dissertation in Table 2.3. In this table, n denotes an integer, the coherences refer to the symmetric-top limit, and J and K are symmetric-top rotational quantum numbers. All the details about mathematical derivations and computational calculations for solving the TDSE using a C++ code have been provided by Makhija in his previous work[144].

Table 2.3: *Rotational coherences of prolatelike asymmetric top molecules. Source: Felker (1992)*[136].

Transition type	Approximate revival time	Contributing coherences
J-type	$n/2(B+C)$	$\lvert\Delta J\rvert = 1, 2,\ \lvert\Delta K\rvert = 0$
K-type	$n/(4A-2B-2C)$	$\lvert\Delta J\rvert = 0,\ \lvert\Delta K\rvert = 2$
Hybrid	$n/(2A-B-C)$	$\lvert\Delta J\rvert = 0,\ \lvert\Delta K\rvert = 1$
C-type	$n/4C$	$\Delta J = 2,\ \Delta K = 0$
A-type	$n/4A$	$\Delta J = 2,\ \Delta K = 2$

The axis distribution moments that characterize the angular distribution of the rotational wave packet now depend on two quantum numbers J and K (K is the projection of J on the MF z-axis),

$$\rho(\theta, \chi, t) = \sum_{JK} \frac{2J+1}{8\pi^2} \langle D^{J\star}_{0,K}(\theta, \chi)\rangle(t) D^{J}_{0,K}(\theta, \chi). \tag{2.27}$$

$\langle\cos^2\theta\rangle$ only measures the 1D alignment between the LF Z-axis and the MF z-axis and hence is no longer adequate to describe the degree of alignment. The expectation values of the cosine squared of the three Euler angles ($\langle\cos^2\theta\rangle, \langle\cos^2\phi\rangle, \langle\cos^2\chi\rangle$) or the directional cosines ($\langle\cos^2\theta_{xX}\rangle, \langle\cos^2\theta_{yY}\rangle, \langle\cos^2\theta_{zZ}\rangle$) are used to characterize the alignment in 3D. However, it is not easy to interpret the degree of alignment by looking at these three quantities simultaneously. V. Makhija *et al.* have proposed a single metric for three-dimensional alignment of molecules[159]. This single scalar metric works for all possible orientations and is easy to interpret physically, helping to design a better 3D alignment scheme[134,144,152].

If the laser field is circularly polarized, by using Eq. (2.20) for the electric field, we can find the interaction potential for asymmetric top molecules to be

$$V(t) = \frac{E_0^2(t)}{2\sqrt{6}} \left[\alpha_0^2 \left(\frac{3}{2}\cos^2\theta - 1 \right) + \alpha_2^2 \frac{\sqrt{6}}{2} \sin^2\theta \cos 2\chi \right]. \tag{2.28}$$

Similar to the discussion on linear molecules, in this case, the angles are measured between the molecular axis and the laser propagation vector instead of the electric field vector. Apart from the difference in the sign, the magnitude (factor of 2), and the redefinition of the coordinate system, the angle dependence of this potential is identical to the interaction potential in a linearly polarized laser field.

2.2 Orientation Resolution through Rotational Coherence Spectroscopy

2.2.1 Linear molecules

In Rotational Coherence Spectroscopy (RCS), measurements of weak-field rotational wave packets have been used to determine rotational constants (and hence the molecular geometry) of gas phase species[136]. It was applied to large species where the spacings of rotational lines (inversely proportional to the moments of inertia) are too narrow and difficult to resolve by using traditional rotational spectroscopy in the frequency domain. The basic idea of RCS is to use a polarized picosecond laser pulse resonant with a vibronic transition of interest to excite an initial alignment of species in the sample via a dipole transition and then probe the rephasing of this initial alignment (revivals) in the time domain. The revivals happen because of the coherences between rotational states. The rotational constants of the species can be obtained by characterizing the time of these revivals.

It is important to note that in the weak-field limit, the pump only excites to nearby rotational states via one cycle of Raman transition following standard spectroscopic selection rules. In strong-field impulsive alignment, the alignment pulse can excite many higher rotational states above the initial one via multiple Raman cycles. The coherences between these states create a broadband, spatially well-defined rotational wave packet. In a stronger alignment laser field, more states will contribute to the rotational wave packet making the revivals more clear and more frequent[126,147].

V. Makhija *et al.* have turned the RCS paradigm the other way around in a femtosecond impulsive alignment pump - SFI probe experiment, where they assume that the molecular structure and polarizability are known and deduce the angle dependence of the SFI probe on the molecular orientation[30,144]. This approach, called Orientation Resolution through Rotational Coherence Spectroscopy (ORRCS), was used to retrieve the ionization rate of C_2H_4 in the MF[30]. Following is a summary of the ORRCS method as it applies to linear molecules.

We model the delay-dependent yield of the ion in the LF, $Y(t)$, (for example, see Fig. 2.4) as a convolution of the MF angle-dependent yield, $R(\theta)$, and the molecular axis distribution, $\rho(\theta, t)$

$$Y(t) = 2\pi \int \rho(\theta, t) R(\theta) \, \sin\theta \mathrm{d}\theta, \tag{2.29}$$

where θ is the angle between the molecular axis and the laser polarization direction (see Sec. 2.1.2). In this model, we employ the assumptions that rotations are separable from vibrational and electronic motions and that ionization is the same for all the rotational states in the entire rotational wave packet.

The unknown angle dependence $R(\theta)$ is expanded in the Legendre polynomial basis, where J can only take on even values due to the plane of symmetry perpendicular to the polarization vector

$$R(\theta) = \sum_{J=0}^{J_{\max}} C_J P_J\,(\cos\theta). \tag{2.30}$$

The sum must be truncated at a finite $J_{\max}$ for reasons discussed below. In a good experiment, $J_{\max}$ should be large enough for the truncated expansion to faithfully represent $R(\theta)$.

Substituting Eq. (2.30) into Eq. (2.29), we have

$$Y(t) = \sum_{J=0}^{J_{\max}} C_J \langle P_J\,(\cos\theta)\rangle\,(t), \tag{2.31}$$

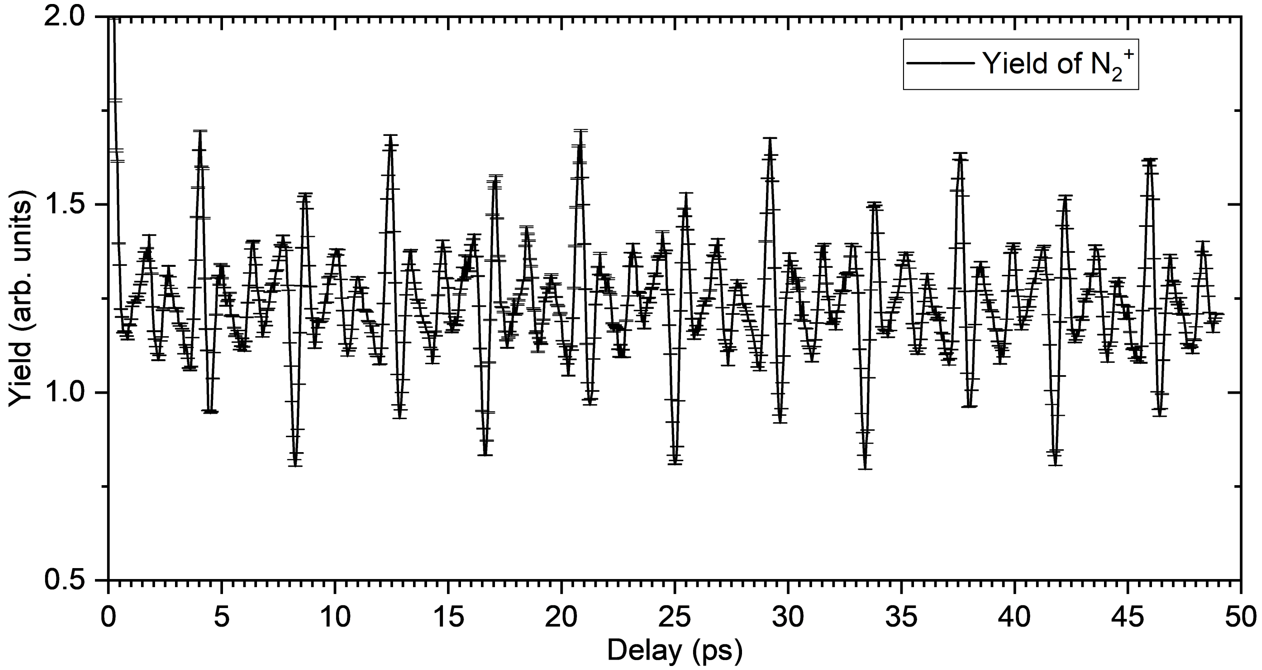

Figure 2.4: N_2^+ *yield as a function of pump-probe delay measured in the experiment.*

where

$$\langle P_J(\cos\theta)\rangle(t) = \int \rho(\theta,t) P_J(\cos\theta)\ \mathrm{d}\Omega \tag{2.32}$$

are the axis distribution moments. Since the delay t and Legendre polynomial index J take on a finite number of values, Eq. (2.31) is a matrix equation that can be solved using linear regression methods (see, for instance, Kuhn and Kjell[160]) for C_J (thus determining $R(\theta)$) if the $\langle P_J(\cos\theta)\rangle(t)$ matrix is known. The matrix is determined by the time-dependent molecular axis distribution, which in turn depends on the rotational wavepacket launched by the pump pulse. Since the rotational wavepacket has a finite width, the axis distribution moments decrease in magnitude with increasing J, and the corresponding terms in Eq. (2.30) become indistinguishable from experimental noise at some value of J — this is where the sum in Eq. (2.30) is truncated. In general, the higher the maximum alignment of the molecules, the larger the value of $J_{\max}$ that can be kept in the expansion.

In impulsive alignment, the rotational wave packet (which determines the time-dependent molecular axis distribution) only depends on the laser fluence and the gas rotational temperature[147,161] (see Sec. 2.1.4). Hence, if the laser fluence and the rotational temperature are known, the time evolution of the molecular axis distribution can be determined by solving the TDSE for a rigid rotor (assuming the aligning pulse does not excite any vibrational or electronic states). However, in practice, laser fluence and rotational temperature measurements are not very accurate[162,163]. Therefore, we use the measured values as an initial guess and fit the data $Y(t)$ over a grid of different pump laser intensities, pulse durations and gas rotational temperatures near the measured values. We consider the one that is best fitted to our data as the wave packet that we have in the experiment. ORRCS has been shown to be able to characterize the rotational wave packet without prior knowledge of the intrinsic molecular ionization dynamics[30,139,140].

2.2.2 Asymmetric top molecules

The basic ORRCS equations for asymmetric top molecules are similar to those for linear molecules in the previous section. The difference is that the angle dependence of the ionization $R(\theta, \chi)$ is now a function of two Euler angles θ and χ. In the MF, θ is the polar angle and χ is the azimuthal angle that describes the orientation of the electric field as shown in Fig. 2.1. We expand the unknown angle dependence $S(\theta, \chi)$ into a linear combination of the Wigner-D rotation matrix elements as

$$S(\theta, \chi) = \sum_{JK} C_{JK} \left[D^{J}_{0,K}(\theta, \chi) + D^{J}_{0,-K}(\theta, \chi) \right]. \tag{2.33}$$

Here, we choose the Wigner-D matrix elements as the basis instead of the spherical harmonics $Y(\theta, \chi)$ for better development of the method in the future with cases where more than two angles are involved (for example, elliptically polarized light). We now need to determine the expansion coefficients C_{JK} from the experiment in order to determine $S(\theta, \chi)$ through Eq. (2.33).

As in the previous section, we measure the ion yield of the asymmetric top molecule as a function of the pump-probe delay, called $Y(t)$. This is modeled as a convolution of the angle-dependent signal, $S(\theta, \chi)$, that we want to retrieve and the time-dependent molecular axis distribution, $\rho(\theta, \chi, t)$, induced by the alignment pump pulse

$$Y(t) = 2\pi \iint \rho(\theta, \chi, t) S(\theta, \chi) \sin\theta \mathrm{d}\theta \mathrm{d}\chi. \tag{2.34}$$

Substituting Eq. (2.33) into Eq. (2.34), we have

$$Y(t) = \sum_{JK} C_{JK} \left[\left\langle D^J_{0,K} \right\rangle (t) + \left\langle D^J_{0,-K} \right\rangle (t) \right], \tag{2.35}$$

where

$$\left\langle D^J_{0,K} \right\rangle (t) = 2\pi \iint \rho(\theta, \chi, t) D^J_{0,K}(\theta, \chi) \, \mathrm{d}\theta \mathrm{d}\chi. \tag{2.36}$$

We would like to shorten the notation for the real basis used in Eq. (2.35) to

$$\langle D_{JK} \rangle (t) = \left[\left\langle D^J_{0,K} \right\rangle (t) + \left\langle D^J_{0,-K} \right\rangle (t) \right]. \tag{2.37}$$

With $Y(t)$ measured experimentally and $\langle D_{JK} \rangle (t)$ obtained from solving the TDSE equation, the expansion coefficients C_{JK} in the matrix equation Eq. (2.35) can be solved in the same manner as Eq. (2.31) using linear regression methods[30,160]. $S(\theta, \chi)$ is now determined through Eq. (2.33).

2.2.3 Advantages and challenges

Compared to other approaches mentioned in chapter 1, the time-domain approach has some unique advantages. To the best of our knowledge, so far this is the only method that has been demonstrated to be able to resolve the dependence on both Euler angles of the non-dissociative ionization of an asymmetric top molecule[30]. This is achieved without the need of 3D alignment[134] and the control of the (probe) polarization in 3D, both of which are nontrivial. The measurement of the delay-dependent ionization yield is not a momentum imaging measurement, hence, we do not need to assume the axial recoil break up of molecules. In fact, we will expand the ORRCS method as a tool for validating the axial recoil approximation in chapter 5.

The approach can be generalized to retrieve the MF angle dependence in other measurements where its preservation of symmetry can be exploited, such as momentum angular distributions[31,140] or HHG[46,139]. It is also relatively easy to adapt the method to measurements using probe pulses of different ellipticity whose applications are being explored[20,129,158].

Apart from possibly long and intensive computations for solving multiple rigid-rotor TDSEs on a grid (for big molecules), in practice, ORRCS requires a long, high-quality delay scan with a high degree of alignment and a reliable fitting procedure[30,139]. The most difficult challenge of ORRCS probably is to determine where to truncate the expansion of the angle dependence in Eq. (2.30) and Eq. (2.33). We will discuss the experimental setup we use for taking data with high signal-to-noise ratio (SNR) in the next chapter, and address the truncation problem in chapter 4.

Chapter 3

Experimental techniques

In this chapter, we first discuss the optical layout of our experimental setup, mainly the separation and combination of laser pulses in a pump-probe scheme, and the independent control of each pulse. After that, we will discuss in detail some essential apparatus: the gas source, the probe pulse, and the detector. The gas source is where we generate rotationally cold molecules under supersonic expansion to achieve a high degree of impulsive alignment. In photoelectron experiments, the third harmonic of the laser output is generated using nonlinear processes in β-BBO crystals and used as a few-photon ionization probe. The detection region is where we measured the yields or the momentum distributions of charged particles (ions and electrons) with our velocity map imaging spectrometer and camera. We also discuss some data acquisition techniques that we implemented to improve the quality of the data.

3.1 Experimental setup

A schematic diagram of the experimental setup is shown in Fig. 3.1. The first important element is the Kansas Light Source (KLS), a home-built, multi-pass, chirped-pulse amplified Ti:Sapphire laser system[164]. KLS delivered pulses at 2 mJ/pulse, 785 nm center wavelength, 35 fs pulse duration, and 2 kHz repetition rate. KLS used a mirror-dispersion-controlled self-mode-locked Ti:Sapphire oscillator (Femtosecond Scientific PRO) producing sub-12 fs, 4 nJ optical pulses at 80 MHz. The chirped pulse amplification (CPA) technique developed by G. Mouru and D. Strickland in 1985[165,166] makes it possible to amplify laser pulses from the nJ energy level in the oscillator to the mJ level in a Ti:Sapphire crystal without damaging any optical components. The main idea is to stretch the pulses temporally into tens of picoseconds before amplification, amplify them and then compress them back to femtosecond pulses. For this invention, G. Mouru and D. Strickland were awarded the Nobel Prize in Physics in 2018 "for groundbreaking inventions in the field of laser physics", in particular "for their method of generating high-intensity, ultra-short optical pulses" (quoted from The Nobel Committee for Physics on the Nobel Prize in Physics 2018). Depending on the powers and repetition rates of the diode pump lasers, and the capacity to remove heat from the crystal (in our case, by using liquid nitrogen), only a certain number of pulses from the oscillator were picked and amplified using a Pockels cell. By changing the operations of the pump lasers and the Pockels cell, we can control the repetition rate of the laser. In the photoelectron experiments (chapter 6), we operated KLS at a 1 kHz repetition rate to work with our 1 kHz camera.

Pulses from KLS are split into two with a broadband 75%-reflection beam-splitter. The transmitted pulses are expanded by a telescope and serve as probes while the reflected pulses are down-collimated by another telescope and further split into two alignment pulses (some experiments used only one aligning pulse). The compressor grating was optimized for the shortest probe pulses, while the alignment pulses are stretched by SF-11 glass. Transform limited probe pulses preclude effects of the chirp on ionization, and long alignment pulses allow us to increase the fluence, and hence increase the alignment as discussed in section 2.1.

Pulse durations were measured using frequency-resolved optical gating (FROG)[167] before the beams enter the vacuum chamber. A window was added before the FROG setup to account for dispersion in the chamber window. The focal spot size of the two pump beams is about two times larger than that of the probe beam, which allows us to measure signal only from well-aligned molecules and reduce the effect of averaging over the distribution of pump intensities in the focus. Focal spot sizes were measured using a camera (see the right panel of Fig. 3.1).

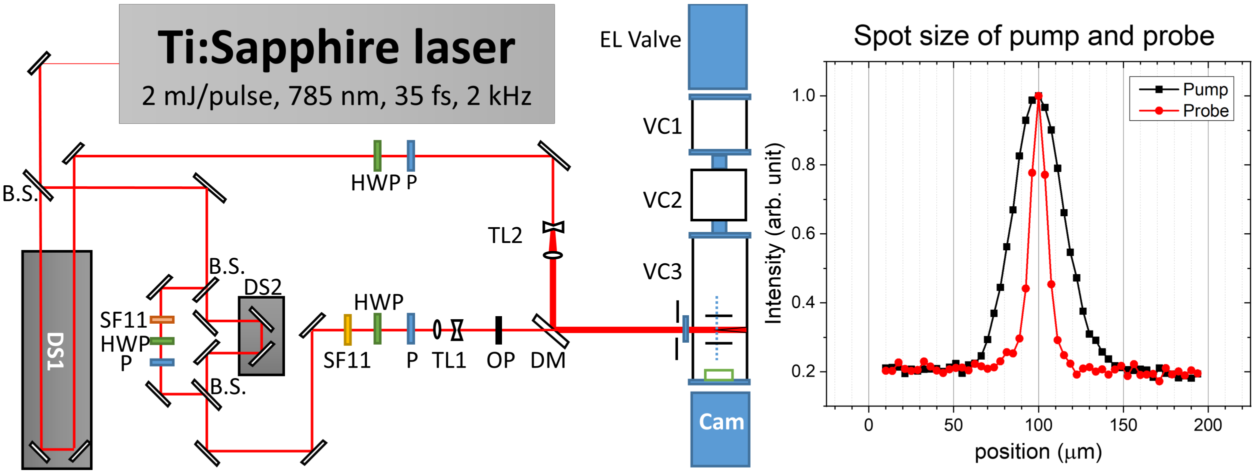

Figure 3.1: *Experimental setup. B.S. = Beam splitter, DS1 = Motorized delay stage, DS2 = Manual delay stage, P = Polarizer, HWP = Half-waveplate, SF11 = SF11 glass, TL1 = Shrinking telescope, OP = Optical chopper running at 500 Hz, TL2 = Expanding telescope, DM = Drilled mirror with a hole through the center, EL Valve = Even-Lavie valve running at 1 kHz, Cam = Camera (either a Basler 504k camera or a Tpx3 time-stamping pixel detector), VC1 = Gas jet chamber (10^{-5} Torr), VC2 = Middle chamber to improve differential pumping (10^{-8} Torr), VC3 = VMI chamber (10^{-10} Torr). The right panel shows the intensity distribution at the foci of the pump and the probe pulses. Adapted from Lam et al.*[31]*. ©APS.*

With the measured values of the pulse duration and the focal spot size, the pulse intensity was estimated assuming Gaussian spatial and temporal profiles. The pulse energy (the beam power divided by its repetition rate) is

$$\text{Pulse energy} = I_0 \int_0^{\infty} e^{-r^2/2r_0^2} r\,dr \int_0^{2\pi} d\phi \int_{-\infty}^{\infty} e^{-4\ln 2\; t^2/\tau^2} dt = I_0 \pi \sqrt{\pi} \omega^2 \tau / \sqrt{\ln 2}, \qquad (3.1)$$

where I_0 is the peak intensity, r_0 is the spatial standard deviation, and τ is the pulse duration. The peak intensity then would be

$$I_0 = \frac{\text{Pulse energy}\sqrt{\ln 2}}{\pi\sqrt{\pi}\omega^2\tau}. \tag{3.2}$$

Achromatic zero-order half-wave plates and cube polarizers in both beams allow independent control of power. Circularly polarized pulses are made by adding achromatic zero-order quarter-wave plates to both the beams and characterized by measuring the Stokes polarization parameters[168]. The delay between the aligning pulses and the probe pulse is varied using a computer-controlled translation stage. The beams are recombined on a drilled mirror with a hole through the center and then back-focused inside a vacuum chamber by a 25 cm focal length concave mirror. Recombination on the holey mirror reduces the energy loss on the pump beams (going through the hole) compared to recombination on a beam-splitter. Inside the chamber, the pulses interact with rotationally cold molecules produced by the supersonic expansion of seeded gas through a 1 kHz Even-Lavie valve[169] (see section 3.3).

3.2 Third-harmonic generation

In the photoelectron experiments (chapter 6), we do not use the fundamental pulse ω (785 nm, 35 fs) directly as the probe but to generate its third harmonic 3ω ($\approx$ 262 nm, $\approx$190 fs) via double- and sum-frequency mixing stages in β-BBO crystals (Fig. 3.2). The third harmonic then serves as the ionizing probe. A sketch of our setup is shown in Fig. 3.2.

We first generate the second harmonic (2ω) by doubling the frequency of the laser fundamental (ω) through a Type I SHG BBO crystal ($\theta = 29.2°$, $\phi = 90°$, 100 μm), anti-reflection coated for 400 and 800 nm. The polarization of the generated second harmonic (e-ray) is perpendicular to the fundamental (o-ray). We employ this property to compensate for the time delay between the two pulses before they enter the THG β-BBO crystal using a birefringent group velocity compensation plate (calcite plate).

After the calcite plate, we use a dual wave plate, which is a half-wave plate for the

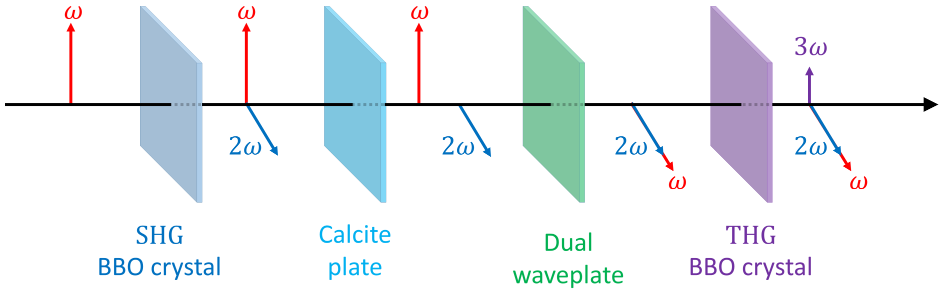

Figure 3.2: *Generation of the third harmonic using β-BBO crystals with half-wave plate and group velocity compensation calcite plate.*

fundamental and the full-wave plate for the second harmonic, to have both the ω and 2ω pulses in the same polarization. Type I sum-frequency mixing will happen and generate the third harmonic (3ω) when both the fundamental (ω) and the second harmonic (2ω) overlap in a Type I THG β-BBO crystal ($\theta = 44.3°$, $\phi = 90°$, 100 μm). The generated third harmonic has the same polarization as the input fundamental (before any optical elements). Finally, we filter out the third harmonic by using several harmonic separators that reflect 99% of the third harmonic and transmit 95% of other wavelengths.

The pulse duration of the third harmonic is estimated by measuring a cross-correlation with a known ω pulse (characterized by the FROG). When the 3ω pulse and the ω pulse with perpendicular polarization overlap temporally and spatially on a THG β-BBO crystal, a signal near 400 nm (2ω) depending on the overlap between these two pulses appears. We filter out this 2ω signal by second harmonic separators and measure it as a function of delay between the ω and 3ω pulses using a photodiode. This delay-dependent signal is called the cross-correlation trace. With ω and 3ω pulses that have gaussian temporal profiles, the pulse duration of the third harmonic can be calculated by

$$\tau_{3\omega} = \sqrt{\tau_{2\omega}^2 - \tau_{\omega}^2}, \tag{3.3}$$

where $\tau_{2\omega}$ is the FWHM of the cross-correlation trace[3].

3.3 Cold molecules and the Even-Lavie valve

Cold molecules in the gas phase are important in many modern experiments, from high-precision spectroscopy to atomic-resolution imaging. Many applications of cold molecules can be found in the discussions by Levy (1981), Carr *et al.* (2009) and Wall (2016)[170–172]. In particular, cold molecules can offer a high level of state selectivity and significantly simplify the experimental spectra, due to the reduction in the number of possible transitions in many degrees of freedom. For the alignment of molecules, cold gas-phase molecules reduce the number of initial thermal states and increase the coherences, thus increase the degree of the alignment[173].

Supersonic expansion is a well-known method for producing cold gas-phase molecules via an adiabatic expansion from a high-pressure gas reservoir (of pressure p_0, temperature T_0) into a vacuum (of background pressure p_0). As described by Miller (1988)[174], the flow may reach sonic speed at the exit if the pressure ratio p_0/p_b exceeds the critical value

$$G = \left(\frac{\gamma+1}{2}\right)^{\gamma/(\gamma-1)}, \tag{3.4}$$

where γ is the heat capacity ratio. The heat capacity ratio γ equals 5/3 for monatomic gases, 7/5 for diatomic gases ignoring vibration, and 9/7 for diatomic gases with vibration. G is less than 2.1 for all gases. Under this condition, the diameter (or width), D, of the expansion orifice (nozzle) is much greater than the mean free path, λ_0, of the gas molecules in the reservoir ($D \gg \lambda_0$)[175]. During the expansion process, the molecules escaping from the reservoir suffer many collisions. These collisions convert the initial thermal energy of the gas to forward kinetic energy, resulting in a fast-moving and dense beam of cold molecules.

Fig. 3.3 shows a schematic diagram of the expansion of a supersonic jet. After exiting the nozzle, the gas expands rapidly into a paraboloid volume constrained by the jet boundary. At the jet boundary, the pressure of the expanding gas is equal to the pressure of the background gas (p_b), and hence the gas can not expand further and is reflected back in form of compression waves. These waves coalesce to form a barrel shock wave (barrel shock).

The barrel shock ends at another shock wave called the Mach disk, which is nearly flat and perpendicular to the centerline of the beam. We can divide the region enclosed by these two shock waves into two sub-regions: the expansion fan region and the zone of silence. Near the beginning of the expansion (the expansion fan region), sufficient collisions happen and cool down the gas. After that, the frequency of collisions drops gradually until there is no collision between molecules. This collision-free region is called the “zone of silence”, and the flow is said to transition from the continuum regime to free molecular flow. All different regions in the expansion are typically described by the Mach number M, which is the ratio between the speed of the flow and the local speed of sound. In the “zone of silence”, the speed of sound is very small compared to the speed of the flow ($M \gg 1$), and that explains the name. When the background has high gas density, these structures are well defined and can be imaged by Schlieren photography[175] or light emission induced by electron beam excitation[176], however, when the gas density is insufficient, the definitions of these structures and thermodynamic variables are difficult.

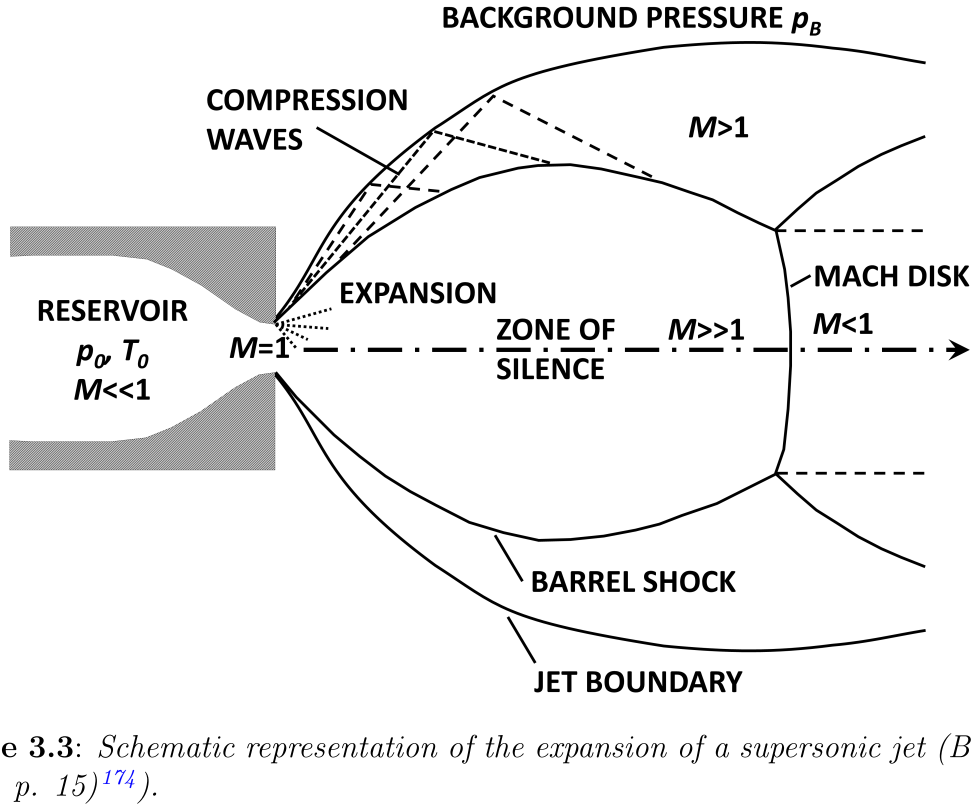

Figure 3.3: *Schematic representation of the expansion of a supersonic jet (Based on Miller (1988, p. 15)[174]).*

The equations describing the gas dynamics in the supersonic expansion are similar to equations used in the design of aircraft. The detailed theoretical derivation can be found in the discussion by Miller (1988)[174] or Morse (1996)[175]. Assuming isentropic, continuum flow, and ideal gas behavior, the main relation between the initial and later temperature is

$$\frac{T}{T_0} = \left(\frac{p}{p_0}\right)^{(\gamma-1)/\gamma} = \left(1 + \frac{\gamma - 1}{2} M^2\right)^{-1}, \tag{3.5}$$

where p and T are the local pressure and temperature. This model works well early in the expansion but starts to fail when the gas flow transition to the molecular flow regime, since the flow is no longer continuum and the number of collisions is insufficient. This equation shows that a lower temperature can be achieved by increasing the pressure difference (raising the initial gas pressure in the reservoir and lowering the pressure in the vacuum chamber). This can be realized by using a pulsed jet where the nozzle only opens and leaks the gas into the vacuum chamber at a certain frequency as needed instead of being continuously open. The pulsed jet operation allows putting high pressure in the reservoir (p_0) while simultaneously reducing the pressure in the vacuum chamber (p). The limitation is that the pulsed jet works better at low repetition rates.

One widely used design of the pulsed jet is the “Even-Lavie valve” designed by Even and Lavie[162] and distributed by Lamid. The Even-Lavie valve is optimized to work for any frequency up to 1 kHz, and its nozzle has a trumpet shape to produce higher gas density. The Even-Lavie valve also has different versions to work at high temperatures (hundreds of Celsius degrees) and low (cryogenic) temperatures. Our Even-Lavie valve was designed for high repetition rate, high pressure, and high temperature. We typically operate the valve at 1 kHz and ≈ 10 μs opening time, reducing the gas load by a factor of 100!

The “zone of silence” is the region we are interested in since molecules have reached their coldest temperature, and the gas beam can be skimmed without serious attenuation[175]. In the forward direction, the “zone of silence” is bounded by the Mach disk shock whose location is, surprisingly, independent of γ and is given by[174,175]

$$x_M = 0.67D\sqrt{\frac{p_0}{p_b}}. \tag{3.6}$$

In our setup, $D \approx 100\ \mu$m, $p_0 \approx 5 \times 10^4$ Torr, and $p_b \approx 1 \times 10^{-5}$ Torr, thus $x_M \approx 4.7$ m. This length, about 4 times longer then our entire setup of vacuum chambers, allows us to use skimmers to collimate and transmit the gas beam through differential pumping stages and reach the detection region with much lower pressure as described in sec. 3.4. The skimmers also narrow down the transverse velocity distributions and thus reduce the translational temperature in these directions.

Determination of the Mach number M, and hence the temperature, requires numerical simulations and can be found in the discussions by Miller (1988)[174] or Morse (1996)[175]. From these calculations, it is estimated that for monatomic gas ($\gamma = 5/3$) the final temperature (at a position far away from the nozzle) is roughly below 1 percent of the initial temperature (T_0). Helium at an initial temperature of about 300 K, for example, can be cooled down to a few degrees K. In our experiments, where a seeded molecular beam is used (a few percent of the target gas mixed with helium), when the two gases reach equilibrium conditions, the target gas will have the same temperature as helium, which makes up the majority of the mixture. The actual operations vary slightly depending on experimental factors, such as cluster formation or the percentage of the target gas, but in general, we reach the temperature of a few degrees K for many different gases in our experiments.

3.4 Vacuum chambers

In the source chamber (VC1 in Fig. 3.1), we evacuate the gas by a turbomolecular pump (Leybold Turbovac MAC integra) that has a pumping speed of 2400 l/s for helium to maintain the ambient pressure of $p_b \approx$ low 10^{-5} Torr while the jet is running at 1 kHz and $\approx 10\ \mu$s opening time! We separate the middle differential pumping chamber (VC2) from the source chamber (VC1) and the detection chamber (VC3) by two skimmers of 3 mm in diameter.

The middle chamber is a 6″ 4-way cross pumped by a 230 l/s turbopump (Pfeiffer Balzers TMU 260). This chamber is at a pressure of low 10^{-11} Torr without the gas load and low 10^{-8} Torr during the experiment. The detection chamber is backed by a 600 l/s turbopump (Agilent Turbo-V 551). For helium, this turbopump only has a compression ratio of 1×10^7, which limits our vacuum to about 1×10^{-9} Torr if the roughing vacuum is in the 10^{-2} Torr regime. To avoid the limitation of the compression ratio, we back this 600 l/s turbo by another turbopump (Pfeiffer TMH 261P, pumping speed 210 l/s). With the new outlet pressure of 10^{-6} Torr, the vacuum in the detection chamber reaches high 10^{-11} Torr without the gas load and low 10^{-9} Torr or below while the gas jet is running.

3.5 Velocity map imaging spectrometer

In 1997, Eppink and Parker introduced an electrostatic immersion lens in the ion imaging setup[177] to map each product velocity to the same point on the imaging detector, independent of the initial position of the particle. This technique is called velocity map imaging (VMI)[178]. Eppink and Parker demonstrated that the VMI technique substantially improves the velocity resolution of charged particle imaging to the point where multiple vibrational levels can be resolved in their studies of the photodissociation and ionization dynamics of molecular oxygen[179].

The basic imaging lens consists of three plates: the repeller, the extractor, and the ground plate. By changing the extractor voltage (by applying a voltage on the feedthrough), we can control the bent equipotential surfaces (nonuniform electric field). These electrodes (plates) act as an electrostatic lens focusing ions of equal velocity components parallel to the detector plane to the same point on the focal plane, reducing the effect of the initial positions of the particles. Our VMI spectrometer is based on the thick-lens design of Kling *et al.*[180] with a few modifications[181] (see Fig. 3.4). The thick-lens design provides high energy resolution over a wide energy range by replacing the single extractor plate with a stack of plates and independently controlling voltages of the first four electrodes[180]. In our VMI, we remove the first extractor plate to accommodate the laser beam going through in the back-focusing geometry[181]. Our extractor plates are connected by 100 MΩ resistors. The voltage on the first extractor plate is dropped sequentially down to zero at the ground plate (connected to the chamber). Our entire VMI spectrometer is enclosed in mu-metal (a nickel–iron soft ferromagnetic alloy with very high permeability) to shield it from stray static or low-frequency magnetic fields. The aluminum flight tube shields ions from stray electric fields. The whole section below the flight tube is also covered in a mu-metal cylinder (not shown in the figure for visibility).

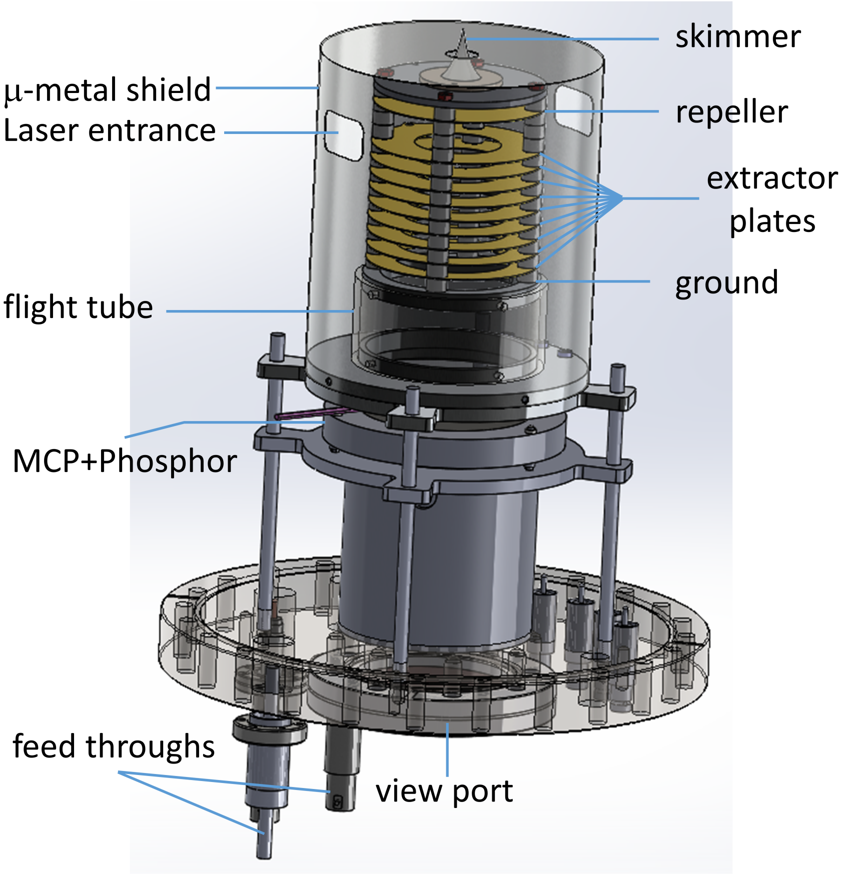

Figure 3.4: *Our velocity map imaging spectrometer using a thick-lens design with a microchannel plate and a fast phosphor screen.*

The gas beam, after passing through the two skimmers mentioned in sec. 3.4, will go through a 0.5 mm skimmer (top of Fig. 3.4) and interacts with the laser in the interaction region (between the repeller and extractor plates). The generated ions are driven by the nonuniform electric field towards the detector. Our detector (Photonis APD04KP-01) has a

Chevron MCP (2 microchannel plates) and a phosphor screen behind them. Each MCP plate is a slab of highly resistive glass (≈ 10 MΩ), 75 mm in diameter and 2 mm in thickness. The MCP consists of an array of millions of miniature electron multipliers (coated holes called channels) parallel to each other. These channels have a pore size of 25 μm, a center-to-center spacing of 32 μm and a bias angle of 8° to the MCP surface, so, about half of the MCP is actually empty!

Due to the bias angle, each particle or photon entering a channel is guaranteed to hit the wall and to start a cascade of electrons. Throughout the MCP, the original signal is amplified by several orders of magnitude (1.55×10^7 times at 2100 V for our MCP according to Photonis). These electrons are accelerated to the phosphor screen (P47) causing phosphorescence (with a lifetime of 120 ns). In the imaging experiments (chapter 5 and chapter 6), images of the phosphor screen were captured by a camera to determine the angular distribution of fragment ions and electrons. With the Basler A504k camera running at 1 kHz or the Tpx3Cam detector[182,183], the data was acquired shot-by-shot. The spatial blurring by the MCP and the phosphor screen detector is further compensated by event counting using the thresholding and centroiding techniques[152,184].

For measuring ion yields (chapter 4), the VMI spectrometer was run in Time-of-Flight (ToF) mode. In this mode, the front plate of the MCP is grounded and a high voltage ($\approx$ 2000 V) is applied on the back plate of the MCP (phosphor is not needed and the VMI is not in focusing condition). The current from the back plate is sent through a decoupling box and is measured on an oscilloscope. When charged fragments hit the MCP detector, a narrow peak ($\approx$ 50 ns) in the voltage is observed. Ions of different mass-to-charge ratios (m/q) arrive at different times (t) on the detector, and can be distinguished from each other. These ions are identified by calibrating the ToF equation[178]

$$t = k\sqrt{\frac{m}{q}} + t_0, \tag{3.7}$$

where the constants k and t_0 can be determined when the m/q and t for two fragments are known.

3.6 Tpx3Cam

The Tpx3Cam is a hybrid pixel detector: an optical sensor with high quantum efficiency[185,186] is bump-bonded to a Timepix3 ASIC[187], a time-stamping readout chip with 256×256 pixels, each with a size of $55\,\mu\text{m} \times 55\,\mu\text{m}$. The processing electronics in each pixel record the ToA (time of arrival) of hits that cross a preset threshold with ns resolution and store it as timecode in a memory inside the pixel. The information about ToT (time-over-threshold), related to the energy deposited in each pixel, is also stored. The readout is data-driven with only T = 475 ns + TOT pixel dead time, which allows multi-hit functionality at the pixel level and fast (80 Mpix/sec) throughput[188]. Tpx3Cam can also accept and time stamp an external trigger pulse, independent of the Timepix3 pixels. The granularity of the trigger time measurement is 0.26 ns.

The Tpx3Cam camera allows us to simultaneously measure all of the fragment ions and then select the ion of interest later using the ToF data calculated from ToA and the external trigger pulse information. We can also synchronize single-shot data to external triggers for gas jet and pump pulse reliably, which is non-trivial at 2 kHz (see sec. 3.8.3). In principle, 3D momentum distributions for ions can also be measured directly due to the 1.56 ns time resolution[189]. For linearly polarized pulses, using either the 2D or the 3D momentum distribution should lead to the same results due to the axial symmetry of the momentum distributions.

3.7 Data normalization

In our experiments, the aligning pulses are mechanically chopped at 500 Hz, letting two consecutive laser pulses through and blocking the next two consecutive laser pulses in each cycle. Since the laser repetition rate is 2 kHz and the Even-Lavie valve operates at 1 kHz, we get four combinations of pump and gas pulses (the probe is always present) in each chopper cycle: pump–probe–gas, pump–probe–no-gas, probe–gas, and probe–no-gas. The details on timing synchronization and identification of trigger status for each shot is laid out in section 3.8. The signal is measured as a function of pump-probe delay for each configuration of pump-probe-gas trigger status. Delay scans are repeated multiple times and averaged. We use this information to correct for both short- and long-term fluctuations in the gas density and laser intensity, and to average over any drifts in pump-probe overlap as shown below.

In ionization yield measurements (chapter 4), at each delay, the background signal measured without the jet on is subtracted from the signal measured with the jet on, and then normalized to the background-corrected signal from the unaligned gas. The corrected ion yield $Y(t)$ used in our further analysis is

$$Y(t) = \frac{Y\,[\mathrm{Pump}, \mathrm{Probe}, \mathrm{Gas}] - Y\,[\mathrm{Pump}, \mathrm{Probe}]}{Y\,[\mathrm{Probe}, \mathrm{Gas}] - Y\,[\mathrm{Probe}]}. \tag{3.8}$$

In the ion momentum measurements (chapter 5), the background count rate for fragment ions was small compared to the rate with the jet. Moreover, negative values introduced by subtraction of images complicate the interpretation of the result, so we did not subtract background images. Instead, the VMI images $M_{2D}(\vec{k}_{2D}, t)$ were normalized to the total count from the unaligned gas measurements to correct for the fluctuation in gas density and laser intensity as expressed in Eq. (3.9).

$$M_{2D}(\vec{k}_{2D}, t) = \frac{[\mathrm{Pump}, \mathrm{Probe}, \mathrm{Gas}]}{\mathrm{Count}\,[\mathrm{Probe}, \mathrm{Gas}]} \tag{3.9}$$

In the photoelectron momentum measurements (chapter 6), because the scattered UV light causes background signal (light and electrons) which can affect the analysis, we use the subtraction of background images at each delay. This step introduces negative values in the low-count area of the image, however, the negative value is typically at a few percent level compared to the electron signals from the ionization channels. The corrected VMI image $M_{2D}(\vec{k}_{2D}, t)$ used in further analysis is

$$M_{2D}(\vec{k}_{2D}, t) = \frac{[\mathrm{Pump}, \mathrm{Probe}, \mathrm{Gas}] - [\mathrm{Pump}, \mathrm{Probe}]}{\mathrm{Count}\,[\mathrm{Probe}, \mathrm{Gas}] - \mathrm{Count}\,[\mathrm{Probe}]} \tag{3.10}$$

We discuss the data and analysis of the molecular ion yield data in chapter 4, and the momentum measurements in chapter 5 and chapter 6.

3.8 Timing synchronization

3.8.1 Ionization yield measurements

Our timing synchronization involves two SRS delay generators model, DG-535 (delay boxes 1 and 2 in Fig. 3.5). The first delay box triggered by the laser Pockels cell (2 kHz) delivers 2 kHz pulses to trigger data acquisition (gated integrator) and monitoring (oscilloscope) equipment. The second delay box, triggered by the first one, generates pulses at 1 kHz to trigger other experimental apparatus such as the gas jet (Even-Lavie valve driver) and the optical chopper. The delay and width of each delay pulse are adjusted to ensure the alternating appearance of 4 trigger combinations of pump-probe-gas mentioned in the previous section.

In the ion yield measurements, the MCP signal from the AC/DC decoupler is sent to the gated integrator. By setting the gate timing, we integrate the signal from one ion of interest (one m/q peak). The integrator averages the "signal in" with a chosen number of samples and sends the "averaged out" to an analog in - analog out channel (AI 0 in our National Instrument BNC-2110 Terminal Block). We also send timing for the gas jet and the chopper ($A \sqcap B$ and $C \sqcap D$ in delay box 2) to two analog in - digital out channels in this BNC box. Both the ToF integrated signal of each laser shot and the timing information about the gas jet and the optical chopper corresponding to this shot are simultaneously recorded by a PCIe-6353 NI DAQ card (connected to the BNC box) and transferred to the computer. This makes it easy to classify the trigger status of each laser shot.

After beginning this project, we purchased a digital oscilloscope (Spectrum digitizer M4i card). This digitizer can record the full ToF signal, allowing us to select the ions of interest while analyzing data without repeating the measurements multiple times for all the peaks in the ToF. This also enables us to perform covariance mapping[190] since ions with different m/q can be acquired simultaneously.

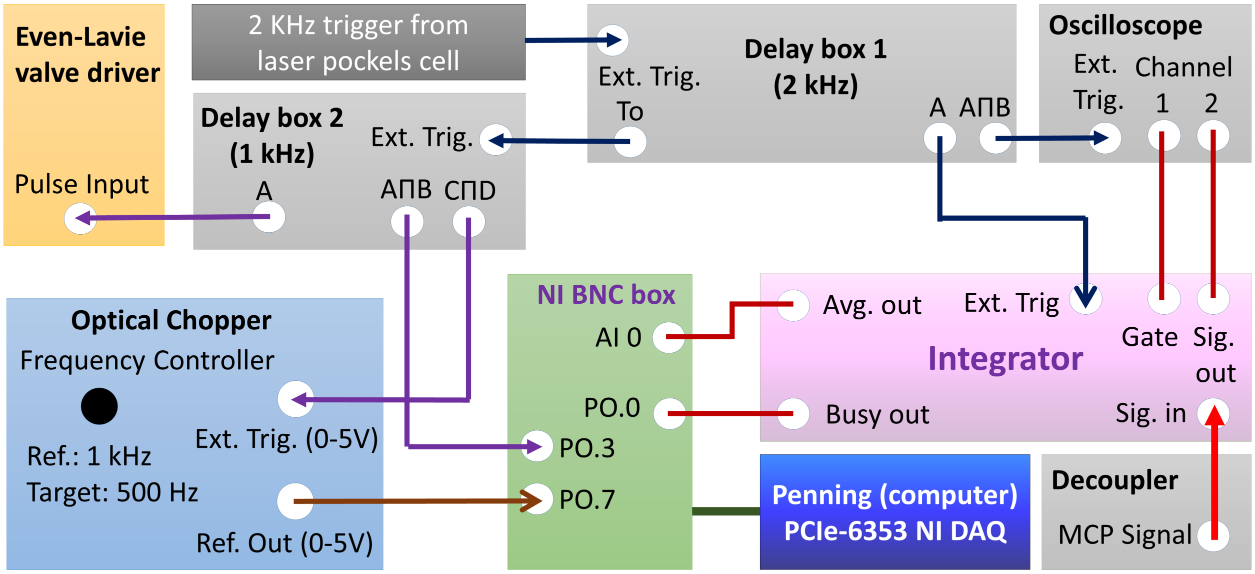

Figure 3.5: *Timing diagram for synchronization with the gated integrator in ionization yield measurements.*

3.8.2 VMI measurements with the 1 kHz Basler A504k camera

When using the Basler A504k camera running at 1 kHz, the camera is triggered instead of the gated integrator or the digital oscilloscope. The difficulty is that 2D images acquired by the camera cannot be analyzed fast enough to be written simultaneously with other timing information (gas jet and chopper) shot to shot. To overcome this problem, we use the same pulses that contain timing information for the chopper and the gas jet (A$\sqcup$B and C$\sqcap$D in delay box 2 of Fig. 3.6) to light up two LEDs with the identical delay and time width by generating the corresponding voltages through the BNC box. These two LEDs will be imaged simultaneously with the VMI spectrum for each laser shot, and hence they encode the trigger status information directly into the camera image as shown on the right of Fig. 3.6. With the LEDs serving as indicators for the on and off states of the pump and gas jet, we can classify the trigger status for each image.

3.8.3 VMI measurements with the Tpx3Cam

This section is an edited version of the discussion published in Physical Review A[31]. *© APS.*

In VMI measurements with the Tpx3Cam, all the timing information about when the

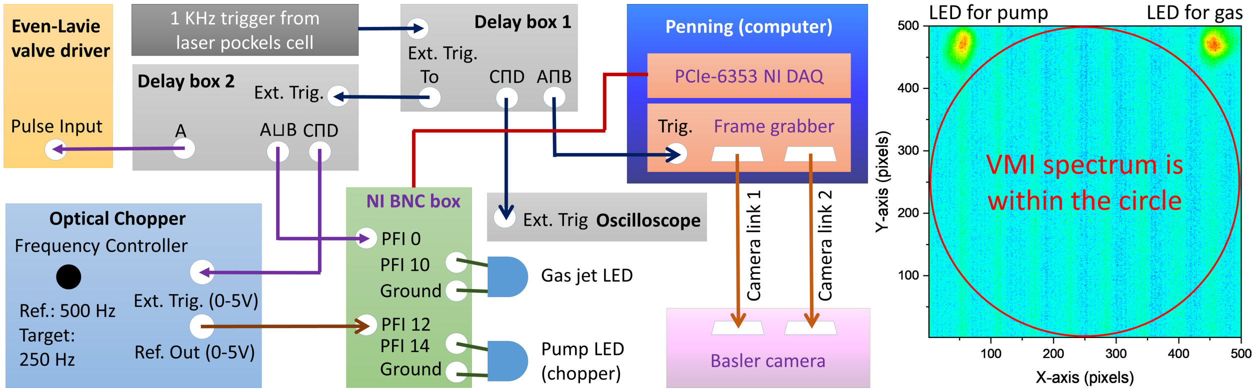

Figure 3.6: *(Left) Timing diagram for synchronization with a frame camera (Basler A504k) in VMI measurements. (Right) LED arrangement in an acquired image. This is a background image with no VMI spectrum of the target gas. The vertical stripes come from camera noise.*

stage is in motion, whether the gas jet is on, and whether the optical chopper is allowing or blocking laser pulses was recorded by a PCIe-6353 NI DAQ card. The information about hits (coordinates, ToA, ToT) together with the arrival time of trigger pulses obtained from the laser were recorded independently by the Tpx3Cam and transferred asynchronously to the computer. To correlate the Tpx3Cam data with the timing information for every shot, the laser pulse trigger supplied to Tpx3Cam was disabled whenever the stage was in motion. The locations and durations of these missing triggers in the Tpx3Cam data provided enough information to correlate and sort the single-shot VMI data with the digital timing information from the DAQ card.

At the beginning, we first run the camera and then the delay stage. At the end, when the scans are done (the delay stage stops), we stop the camera. In Fig. 3.7, we show the time gap between consecutive trigger pulses recorded by the Tpx3Cam. There are three levels of trigger time gap: 500 μs, 10^4 μs and 10^5 μs. 500 μs corresponds to the 2 kHz laser repetition rate and this happens when the delay stage stays at one delay and the data is being acquired. 10^4 μs is the time it takes for the delay stage to move to the next delay in a scan (100 fs step in this example). The longest time gap between triggers, about 3×10^5 μs, is the time it takes for the stage to move from the longest delay to the earliest delay in one scan (about 50 ps in this example). Since we know when each scan starts and finishes, we can synchronize the Tpx3Cam triggers with the timing information about the gas jet and chopper acquired by our PCIe-6353 NI DAQ card and figure out the trigger status of each hit. If for some reason the Tpx3Cam misses some data in between, we can also discard that scan and synchronize with the next scan.

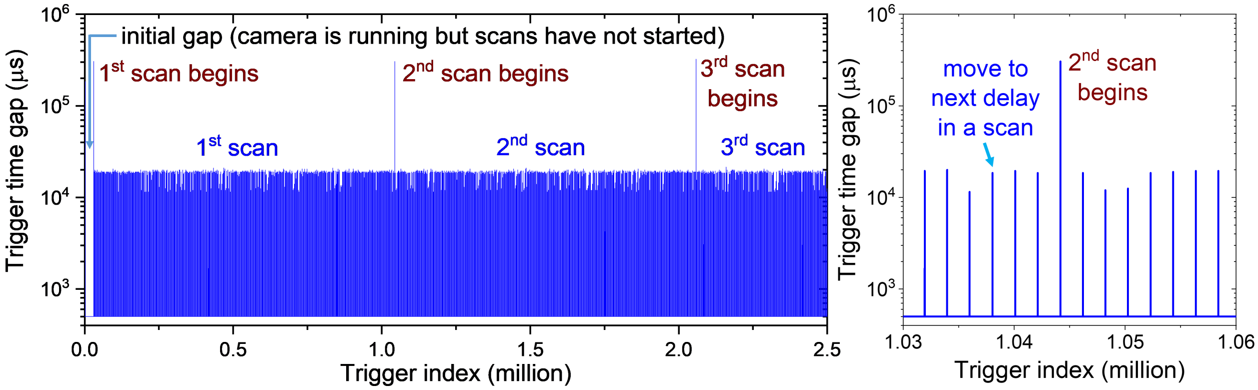

Figure 3.7: *Time gap between consecutive trigger pulses recorded by the Tpx3Cam.*

In Fig. 3.8(a), we demonstrate the performance of single-shot trigger status identification using hits-per-shot histograms. In this measurement, CO_2 molecules are impulsively aligned by a non-resonant pump and then ionized and dissociated by a probe pulse in the VMI spectrometer. We measure the LF 2D angular distribution of the fragment ions $M_{2D}(\vec{k}_{2D}, t)$ by using the Tpx3Cam to read out the signal created by the MCP and fast phosphor screen. The number of hits here is from the whole spectrum, including residual gas which is mostly water. The histogram for each type of trigger should be a smooth one-peak distribution; any mislabeled hits will pile up as a second peak at the wrong place. The absence of a peak in the jet-off histograms at $\sim$ 50 hits per shot, and the contrast between jet-on and jet-off histograms near zero hits per shot, indicate an error rate of no more than one per thousand shots.

Fig. 3.8(b) depicts the total counts of CO^+ for each type of trigger, showing a good signal-to-noise ratio. When the gas jet is on, the number of hits (black solid line and red dotted line) is about 100 times more than that when the gas jet is off (blue dashed line and magenta dashed-dotted line). The signal with the aligning pulse (black line) exhibits a strong delay dependence while the modulation of the signal without the aligning pulse (due to fluctuation in laser intensity and gas density, indicated by the red dotted line) is much weaker.

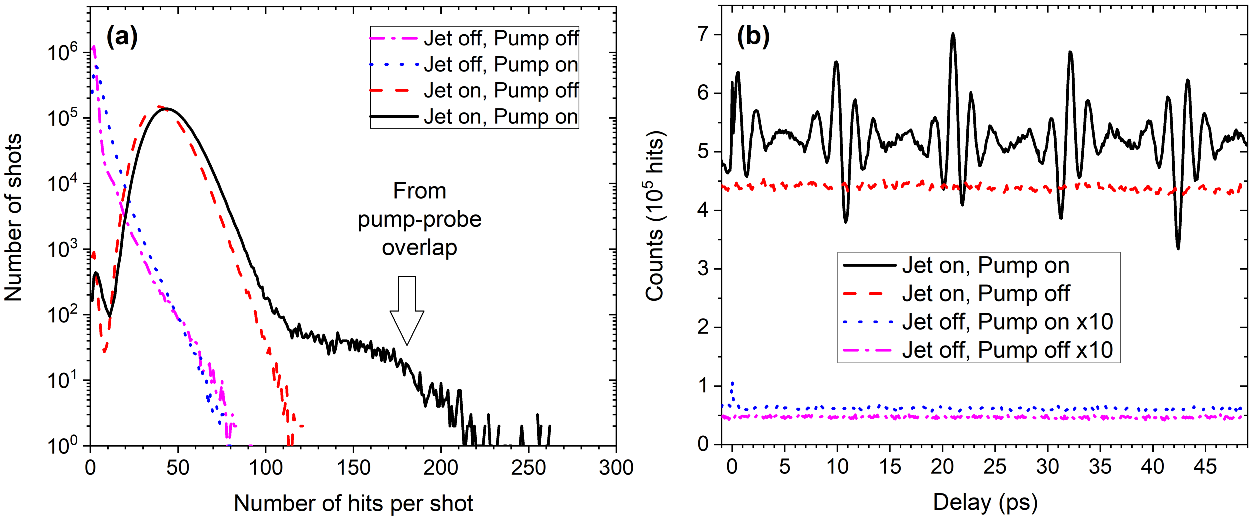

Figure 3.8: *(a) Hits-per-shot histograms for different trigger types of pump-probe-gas combination. (b) Total* CO^+ *counts for each type of trigger.*

Chapter 4

Angle-dependent strong-field ionization of molecules

In this chapter, we further explore the ORRCS method experimentally and statistically. We study the angle dependence of the strong-field non-dissociative single ionization of carbon dioxide (CO_2, a linear molecule) and sulfur dioxide (SO_2, an asymmetric top molecule) probed by linearly and circularly polarized pulses. The angle-dependent ionization probability is extracted from time-domain measurements on an impulsively-excited rotational wave-packet. The results from the measurements with linear and circular polarization are compared for consistency. For CO_2, the angle dependence of the ionization probability by linearly polarized pulses extracted using ORRCS is compared with data obtained from a direct angle-scan measurement. We also compare our results with previous work where there were discrepancies. Throughout this chapter, we discuss in depth the retrieval procedure with data under different experimental conditions and analyze the results from different perspectives of statistical analysis. This will give more experimental evidence and improve the angle-dependent retrieval algorithm on the ORRCS method.

4.1 Angle-dependent strong-field ionization of CO_2

This section is an edited version of the discussion published in Physical Review A[31]. ©APS.

4.1.1 Motivation

Ionization is the first step in many high-order strong-field processes, including high-harmonic generation, above-threshold ionization and laser-induced electron diffraction[25,46,191–196]. However, strong-field ionization (SFI) of molecules is still not well understood. Although there are several models[197–199] that provide accurate intensity-dependent or total ionization yields from atoms at infrared wavelengths, molecular ionization models are still being developed and face many difficulties[32,141,158,193,200,201]. For example, the measured angle-dependent single ionization of N_2 and O_2 can be reproduced by theoretical models[29,202,203], but that is not the case for CO_2. The angular width of the angle-dependent single ionization of CO_2 reported by Pavičić *et al.*[29] appears to be too narrow, with the problem suspected to be in the deconvolution process. Later measurements at different intensity or wavelength were done by Thomann *et al.*[137], Weber *et al.*[129], and the topic is still being discussed actively[29,33,129,131,137,203–213].

In this section, we revisit this problem using the time-domain approach (Sec. 2.2) to retrieve the angle-dependent ionization probability of CO_2 with significantly better angular resolution. We launch a rotational wave-packet created by 1D impulsive alignment using a linearly-polarized non-resonant laser pulse[17,19] and measure the molecular ion yield as a function of delay between the aligning pump and the ionizing probe pulse. We then use a fitting procedure to retrieve the angle-dependent ionization yield. Our goal is to determine this dependence with substantially higher angular resolution than prior measurements[29,129,137] by using cold molecules and multi-pulse alignment. The retrieved angle dependence is compared with data obtained from a direct angle-scan measurement and checked for consistency with results from measurements using circularly polarized ionizing probe pulse through a geometrical transformation. This easy adaptation of the time-domain approach to different ellipticity of laser pulses can be used to explore other dynamics, especially processes triggered by re-collision[20,25,96,129,158,214–216].

4.1.2 Strong-field ionization of CO_2 by linearly polarized pulses

An example of the experimental data and fit to the normalized CO_2^+ yield (see Eq. (3.8)) as a function of delay probed by a 35 fs, 140 TW/cm^2 linearly polarized pulse is shown in Fig. 4.1. The fit with $J_{max} = 4$ according to the expansion in Eq. (2.30) shows excellent agreement with the data. It is estimated from the fit that after the first aligning pulse (250 fs, 4.7 TW/cm^2), the molecular sample reaches a degree of alignment of $\langle\cos^2\theta\rangle \approx 0.73$ (at half-revival), and after the second aligning pulse (100 fs, 14 TW/cm^2), the degree of alignment is improved to $\langle\cos^2\theta\rangle \approx 0.86$. The rotational temperature of the gas is estimated to be about 2 K.

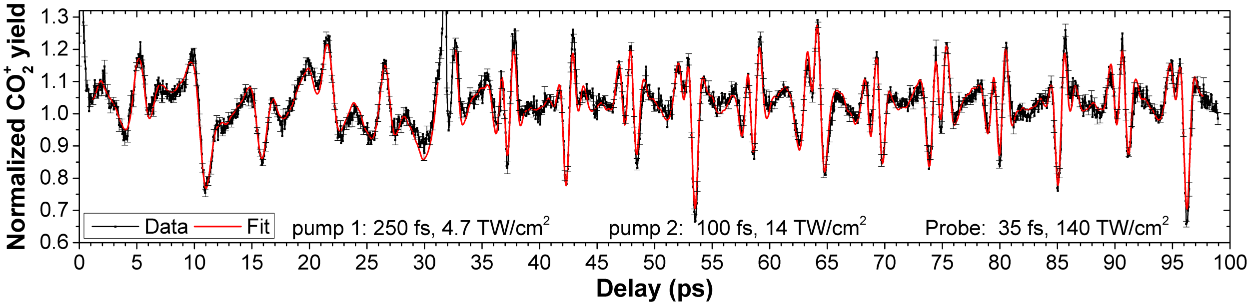

Figure 4.1: *Experimental data and fit to the normalized* CO_2^+ *yield obtained with a linearly polarized probe as a function of delay. The pulse duration and intensity of the first and second aligning pulses are 250 fs, 4.7 TW/cm*^{2} *and 100 fs, 14 TW/cm*^{2}*, respectively. The 100 fs aligning pulse is delayed by 32.25 ps with respect to the 250 fs aligning pulse (3/4 revival of* CO_2*). The ionizing pulse has 35 fs pulse width and 140 TW/cm*^{2} *intensity. Focal spot size and pulse duration for the probe were measured using a camera and FROG, respectively. The intensity was estimated assuming Gaussian spatial and temporal profiles. All pulses are linearly polarized in the same direction.*

We retrieved the angle-dependent single-ionization probability from the delay-dependent data before and after the second aligning pulse in Fig. 4.1 separately to study how the retrieval depends on the degree of alignment. Fig. 4.2 shows the retrieved angle-dependent ionization probability and how it changes with different values of J_{max} in Eq. (2.31). In this section, we use $R^{lin}(\theta)$ for the angle dependent probability, where the superscript indicates the polarization of the ionizing pulse. In panel (a), with a high degree of alignment $\langle\cos^2\theta\rangle \approx$

0.86, the high order C_J coefficients can be determined reliably to be small and have little contribution to the retrieved angle-dependent ionization probability $R^{\mathrm{lin}}(\theta)$. In other words, $R^{\mathrm{lin}}(\theta)$ converges for $J_{max} \geq 4$. In panel (b), with $\langle \cos^2 \theta \rangle \approx 0.73$, the higher coefficients are less reliable, and the retrieved angle-dependent ionization probability $R^{\mathrm{lin}}(\theta)$ varies wildly with the expansion. Although the fit to the delay-dependent data converges in both cases, the extracted angular distribution in the case of a lower degree of alignment is inconsistent since there can be more parameters in the fitting function than we can reliably determine.

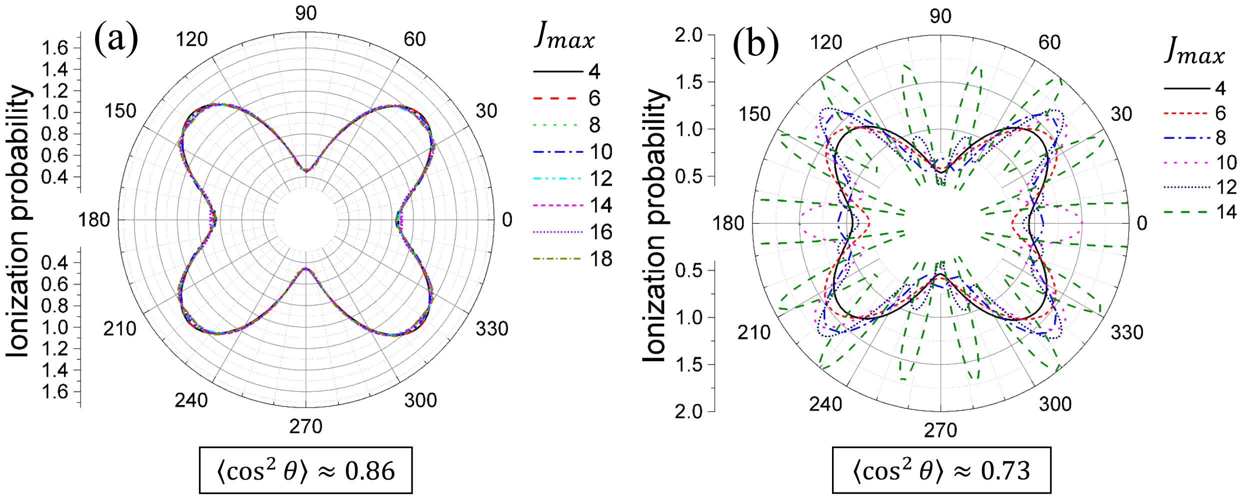

Figure 4.2: *Angle-dependent single-ionization probability of* CO_2 *retrieved from the delay-dependent data in Fig. 4.1 for two different degrees of alignment and different orders of the expansion in Legendre polynomials according to Eq. (2.30). With* $\langle \cos^2 \theta \rangle \approx 0.86$ *(panel a), the high order coefficients can be determined reliably to be small and have little contribution to the retrieved angle-dependent ionization probability* $R^{\mathrm{lin}}(\theta)$*. With* $\langle \cos^2 \theta \rangle \approx 0.73$ *(panel b), the higher coefficients are less reliable, and the retrieved angle-dependent ionization probability* $R^{\mathrm{lin}}(\theta)$ *varies wildly with the expansion.*

We also performed angle-scan measurements[29] where the ionization yield $Y(\alpha)$ was measured as a function of angle α between polarization axes of the aligning pump pulses and the ionizing probe pulse. For these measurements, the pump-pulse polarization axis is fixed but probe-pulse polarization is rotated by a half-wave plate mounted on a computer-controlled motorized rotational stage. In the case of a high degree of alignment, the molecular axis distribution will be narrow, which makes $Y(\alpha)$ a fair representation of $R^{\mathrm{lin}}(\theta)$.

The raw data is shown in Fig. 4.3(b) without using any deconvolution or fitting procedure.

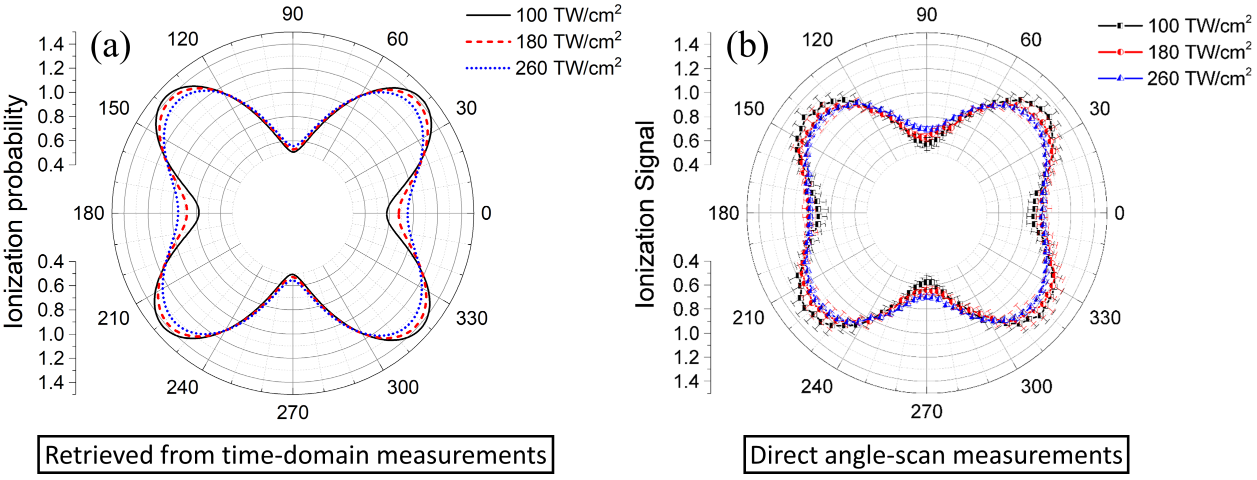

Figure 4.3: *Panel (a) shows the angle-dependent ionization probability* $R^{\text{lin}}(\theta)$ *retrieved from time-domain measurements for different probe intensities. The estimated degree of molecular alignment is* $\langle\cos^2\theta\rangle \approx 0.87$ *in all cases. The expansion in Eq. (2.30) was truncated at* $J_{max} = 6$. *Using the same pump pulses, panel (b) shows measured ionization yield* $Y(\alpha)$ *as a function of angle* α *between polarization axes of the aligning pump pulses and the ionizing probe pulse at peak alignment (42.5 ps after the second pump) with no deconvolution or fitting. While* $R^{\text{lin}}(\theta)$ *is four-fold symmetric,* $Y(\alpha)$ *was measured over* 2π *and has not been symmetrized.*

The error bars in the ionization yields represent the standard deviation from results of repeated experimental scans under the same conditions. As expected from a higher degree of molecular alignment, our $Y(\alpha)$ have sharper features compared to previous data[29,129] (which did not show a clear dip at 0°) and can be considered as a better representation of $R^{\text{lin}}(\theta)$. Although $R^{\text{lin}}(\theta)$ is sharper than $Y(\alpha)$ since the molecular axis distribution is deconcolved, they both have the same basic structure.

Despite having a higher degree of molecular alignment as compared to previous experiments[29,129,137], our deconvolved angle-dependent ionization probability $R^{\text{lin}}(\theta)$ looks broader, with a peak around 40°. Measurements at different intensities (Fig. 4.3(a)) show that the angle dependence of ionization is more isotropic at higher probe intensities. Murray *et al.* theoretically predicted that the exact location of the maximum depends on the laser intensity[208]; however, this variation is too small in our experiment to make any solid conclusions.

4.1.3 Strong-field ionization of CO_2 by circularly polarized pulses

The ORRCS approach is easily adapted to circularly polarized probes if the axial symmetry required for Eq. (2.30) is maintained by making the pump pulses circularly polarized as well. For this polarization geometry and multi-cycle laser pulses, the axis of symmetry is the laser propagation direction rather than the polarization direction. As mentioned in chapter 2, in order to avoid confusion with the linearly polarized case, we use the symbol β for the polar angle between the molecular axis $\vec{m}$ and the propagation vector $\vec{k}_p$. When $\beta = 0°$, the molecules are along $\vec{k}_p$, and we have k-alignment; when $\beta = 90°$, the molecules are in the plane perpendicular to $\vec{k}_p$, and we have planar alignment[157].

Fig. 4.4 shows an example of experimental data and fit to the CO_2^+ ionization yield probed by a circularly polarized pulse as a function of delay (a) and the retrieved angle-dependent ionization probability $R^{\text{cir}}(\beta)$ at different probe intensities (b). $R^{\text{cir}}(\beta)$ is closer to a dumbbell shape in comparison with the butterfly shape of $R^{\text{lin}}(\theta)$. $R^{\text{cir}}(\beta)$ also becomes more isotropic at higher probe intensity. Within the assumption of adiabatic ionization, we can perform a geometrical transformation from the angle-dependent ionization signal by the linearly polarized probe pulse $R^{\text{lin}}(\theta)$ to reproduce the main features of the circular polarization measurements $R^{\text{cir}}(\beta)$[33,158]. For a particular angle β, $R^{\text{cir}}(\beta)$ can be obtained by averaging $R^{\text{lin}}(\theta)$ over all the electric field vectors sweeping the plane perpendicular to $\vec{k}_p$ (see Fig. 4.4(d)). The molecular axis and the electric field can be written as $\vec{m}(0, \sin\beta, \cos\beta)$ and $\vec{E}(\cos\phi, \sin\phi, 0)$, then $\cos\theta = \vec{m} \cdot \vec{E} = \sin\beta \sin\phi$. $R^{\text{cir}}(\beta)$ will then be obtained by replacing $\cos\theta$ in the associated Legendre polynomial expansion of $R^{\text{lin}}(\theta)$ in Eq. (2.30) by $\sin\beta\sin\phi$ and taking the average over ϕ,

$$R^{\text{cir}}(\beta) = \int_0^{2\pi} R^{\text{lin}}(\theta) d\phi = \int_0^{2\pi} \sum_{J=0}^{J_{\text{max}}} C_J P_J(\cos\theta) d\phi = \sum_{J=0}^{J_{\text{max}}} C_J \int_0^{2\pi} P_J(\sin\beta\sin\phi) d\phi. \quad (4.1)$$

The results in Fig. 4.4(b-c) show qualitative consistency between the two independent measurements using linearly and circularly polarized light.

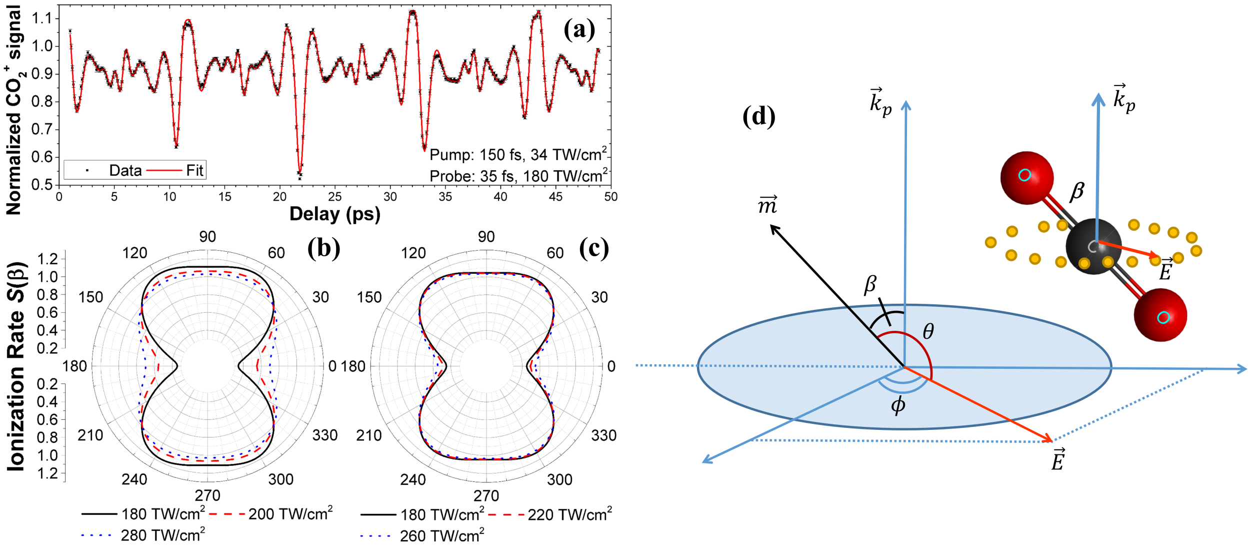

Figure 4.4: *(a) Experimental data and fit to the* CO_2^+ *ionization yield probed by a circularly polarized pulse as a function of delay. These measurements used a single alignment pulse and achieved the degree of alignment* $\langle\cos^2\beta\rangle \approx 0.82$. *As in Fig. 4.2, coefficients up to* $J_{max} = 4$ *were found to be sufficient to represent* $R^{cir}(\beta)$. *(b) The retrieved angle-dependent ionization probability* $R^{\mathrm{cir}}(\beta)$ *for different intensities. (c) Ionization probability* $R^{\mathrm{cir}}(\beta)$ *by a circularly polarized ionizing pulse obtained from the transformation of* $R^{\mathrm{lin}}(\theta)$ *measured with linearly polarized pulses in Sec. 4.1.2. (d) Definition of angles:* θ *is the angle between the molecular axis,* $\vec{m}$, *and the polarization axis.* β *is the angle between the molecular axis and the electric field propagation vector,* $\vec{k}_p$. *Within the assumption of adiabatic ionization, the angle-dependent ionization probability,* $R^{\mathrm{cir}}(\beta)$, *by a circularly polarized ionizing pulse can be obtained by averaging the angle-dependent ionization probability,* $R^{\mathrm{lin}}(\theta)$, *by a linearly polarized ionizing pulse over the plane perpendicular to* $\vec{k}_p$ *(using angle* ϕ*).*

4.2 Angle-dependent strong-field ionization of SO_2

4.2.1 Motivation

In this section, we apply the time-domain approach to retrieve the angle-dependent ionization rates of SO_2, an asymmetric top molecule. We also develop and discuss in-depth the statistical analysis of the fit to avoid overfitting and to determine the appropriate angle dependence. While the angle-dependent ionization of asymmetric top molecules has not been as widely investigated as linear and symmetric top molecules[29,34,130,141,142], results from this work provide more evidence for testing theories and models on the ionization of molecules in a strong field. It may also help further understand other studies where SO_2 has been examined[100,114,132,135,143,217–219].

4.2.2 Non-dissociative ionization of SO_2

An example of the experimental data and a fit to the SO_2^+ single ionization yield as a function of delay probed by a 35 fs, 250 TW/cm^2 linearly polarized pulse is shown in Fig. 4.5. From the TDSE, we calculated the expectation values of the Wigner-D rotation matrices $\langle D_{JK}\rangle(t)$ in Eq. (2.37) up to $J = 8$ and $K = 8$. The model including all 15 coefficients from C_{00} to C_{88} will be considered as the "full model". Since not all the C_{JK} coefficients are equally important and including too many parameters can cause over-fitting, we will discuss how to reduce the "full model" to a parsimonious one.

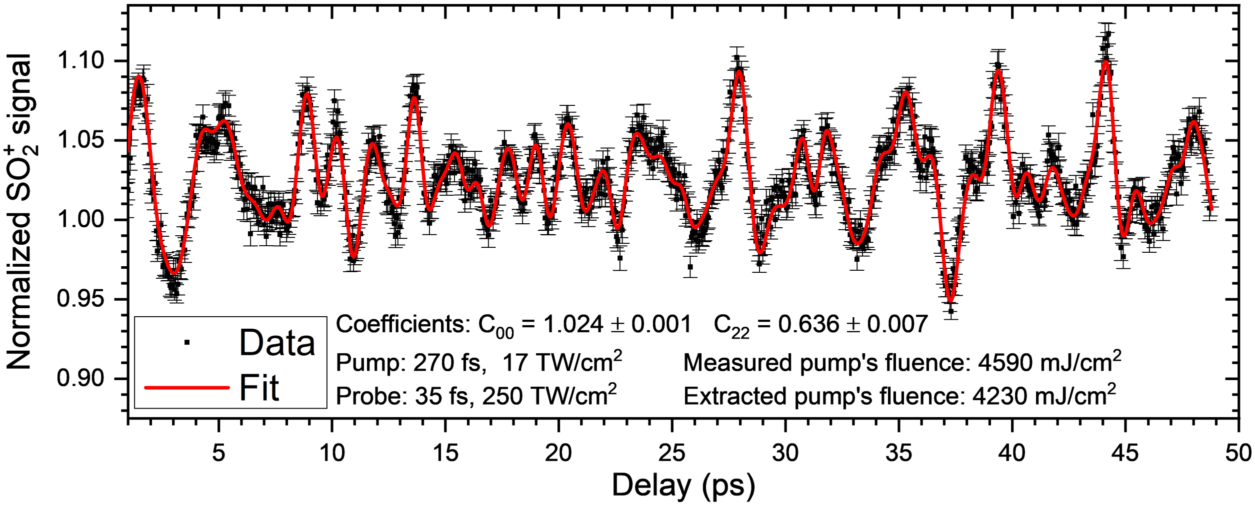

Figure 4.5: *Experimental data and best fit to the delay-dependent single ionization yield* SO_2^+ *with the model including* C_{00} *(isotropic) and* C_{22} *(variable). The aligning pump pulse is estimated to be about 270 fs, 11 TW/cm^2; the ionizing probe pulse is about 35 fs, 250 TW/cm^2. The estimated rotational temperature of the gas is about* 1.8 *K.*

First of all, does the fitting procedure yield a proper global minimum, or in other words, is the solution unique? In Fig. 4.6(a), we plot the dependence of the reduced chi-square of the fit χ^2_{red} in the three-dimensional space of the laser pulse duration, laser intensity, and gas rotational temperature. The surfaces of constant χ^2_{red} values converge globally to a hyperboloid minimum. This is compatible with impulsive alignment where the alignment only depends on the gas temperature and the laser fluence (which is a hyperbola in the two-dimensional space of the laser intensity and pulse duration) as discussed previously in section 2.1.4 of chapter 2. As long as the fit can adequately match the data, this result does not depend on how may coefficients are included in the fit because the contributions from high-order coefficients are typically much smaller than those of the lower-order ones.

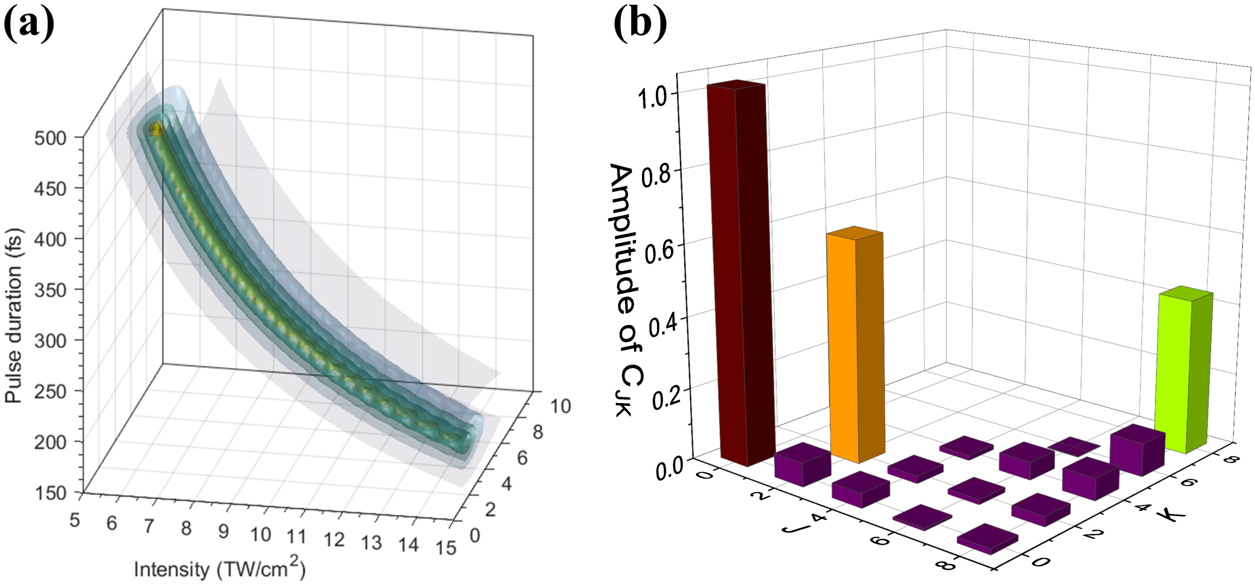

Figure 4.6: *(a) The dependence of the reduced chi-square of the fit, χ^2_{red}, on the aligning pump pulse intensity, pulse duration, and the rotational temperature of the gas. χ^2_{red} is defined as $\frac{1}{N-k-1}\sum_{i=1}^{N}(\hat{y}_i - y_i)^2/\sigma_i^2$ where N is the number of data points and k is the number of coefficients included*[160]*. The surfaces correspond to χ^2_{red} = Min(χ^2_{red})+ constant. From the innermost to the outermost surface, the constants are 0.1, 0.2, 0.5, 1, 2 and 5 respectively. (b) Estimated amplitude of the coefficients in a fit using the "full model". Most of them are close to zero except C_{00}, C_{22} and C_{88}. If C_{88} is eliminated (as discussed in the text), this indicates the convergence of $S(\theta,\chi)$ in both directions. As we include more C_{JK} of higher J and K, the major features of the retrieved $S(\theta,\chi)$ (mostly defined by C_{22}) remain the same.*

In practice, the essential problem of retrieving the angle-dependent ionization rate $S(\theta,\chi)$ is to determine where to truncate the expansion in Eq. (2.35) and then to estimate all the coefficients C_{JK} involved. It is critical since a small modulation in $Y(t)$ can also result in significant change in the retrieved $S(\theta,\chi)$. This truncation depends on the number of coefficients C_{JK} required to describe the true distribution $S(\theta,\chi)$ and the number of coefficients C_{JK} we can reliably determine from the high order coherence of our rotational wave packet. For asymmetric-top molecules, the coefficients C_{JK} are two dimensional (depend on both J

and K), and therefore further complicate the problem. Although there were a few relevant discussions previously[139,143], the goodness of the fit and the truncation of the expansion in Eq. (2.35) are still under investigation.

Our previous discussion on CO_2 (Sec. 4.1) suggests that the convergence of the angle dependence $S(\theta, \chi)$ retrieved from the fit with the expansion in Eq. (2.35) is a good indicator that we have more than enough resolution to retrieve $S(\theta, \chi)$ reliably. The amplitude of all the coefficients in a fit using the "full model" are shown in Fig. 4.6(b), with most of them close to zero except C_{00}, C_{22} and C_{88}. If C_{88} is eliminated (as we shall justify in the following discussions), this shows the convergence of $S(\theta, \chi)$ in both directions. As we include more C_{JK} of higher J and K, the major features of the retrieved $S(\theta, \chi)$ (mostly defined by C_{22}) remain the same.

Table. 4.1 shows the estimated value of the coefficients C_{JK} with their standard deviation, t-value, and p-value obtained from the fit (using R). The p-value indicates the statistical significance of the hypothesis. A smaller p-value implies that the coefficient has a more important contribution to the fit[160,220]. We can construct a nested model of increasing complexity by adding more coefficients to the model in order of increasing p-value and then observe what difference the coefficients make. In the case of SO_2^+, the order of coefficients in the nested model is shown in Table. 4.1.

First, we look at the prediction ability and the stability of the coefficients. The experiment data are randomized and then separated into two parts: the training part (about 60% of the data) and the test part (about 40% of the data). We use the training part to construct the model (i.e., estimate the coefficients by fitting using linear regression), and then use this model to predict the real data in the second part. The root-mean-square error (RMSE) then can be calculated as

$$\mathrm{RMSE} = \sqrt{\frac{1}{N}\sum_{i=1}^{N}(\hat{y}_i - y_i)^2/\sigma_i^2}, \tag{4.2}$$

where y_i is the experimental value of the i^{th} data point, $\hat{y}_i$ is the value predicted by the model built from the training part, and N is the number of points used for testing the model. Repetition of this process a large number of times gives a distribution of the RMSE

Coefficients	Estimate	Std. error	t value	$\Pr(>\lvert t\rvert)$
C_{00}	1.020136	0.001062	960.384	$< 2E - 16$
C_{22}	0.622081	0.006866	90.602	$< 2E - 16$
C_{20}	−0.067405	0.003905	−17.261	$< 2E - 16$
C_{40}	0.041391	0.006421	6.447	$1.83E - 10$
C_{88}	0.435984	0.163993	2.659	0.00798
C_{42}	−0.021002	0.008980	−2.339	0.01955
C_{84}	0.062439	0.030443	2.051	0.04054
C_{64}	0.050034	0.024963	2.004	0.04533
C_{86}	0.093061	0.050924	1.827	0.06795
C_{82}	−0.028396	0.016406	−1.731	0.08381
C_{80}	−0.016068	0.010766	−1.492	0.13593
C_{62}	−0.013690	0.014444	−0.948	0.34349
C_{44}	0.014064	0.020066	0.701	0.48354
C_{60}	−0.006513	0.010291	−0.633	0.52696
C_{66}	−0.001752	0.042349	−0.041	0.96702

Table 4.1: *Estimated values of coefficients with their standard deviation, t-value, and p-value (last column) obtained from R when fitting* SO_2^+ *data using the full model. The coefficients are in order of increasing p-value.*

for a particular model, represented by the mean and the standard deviation. Next, we increase the number of coefficients in the model and repeat the same analysis. This will give us the plot of prediction error as a function of models in Fig.4.7(a). Each time the linear regression fit was done on the training part of the data, values of the coefficients were also recorded. Fig.4.7(b) shows how stable the coefficients are with different data subsets. They converge to a similar distribution of the linear regression fit shown in Table. 4.1.

Since the prediction error, as shown in Fig.4.7(a), does not improve by any significant amount after including the first two variables (C_{22} and C_{20}) in the model, this should be a good place to truncate the expansion. Note that C_{20} and C_{40} are essentially zero and do not contribute much to the final result; the C_{88} coefficient is extremely unstable. We therefore decide to keep only the first variable (C_{22}) and the intercept (C_{00}), although p-values of other coefficients still well surpass the typically-used arbitrary standard of 0.05[139,143,160].

We then rerun the fit using the reduced model above. The extracted coefficients from this reduced model have values very similar to those obtained from the full model in Table. 4.2.

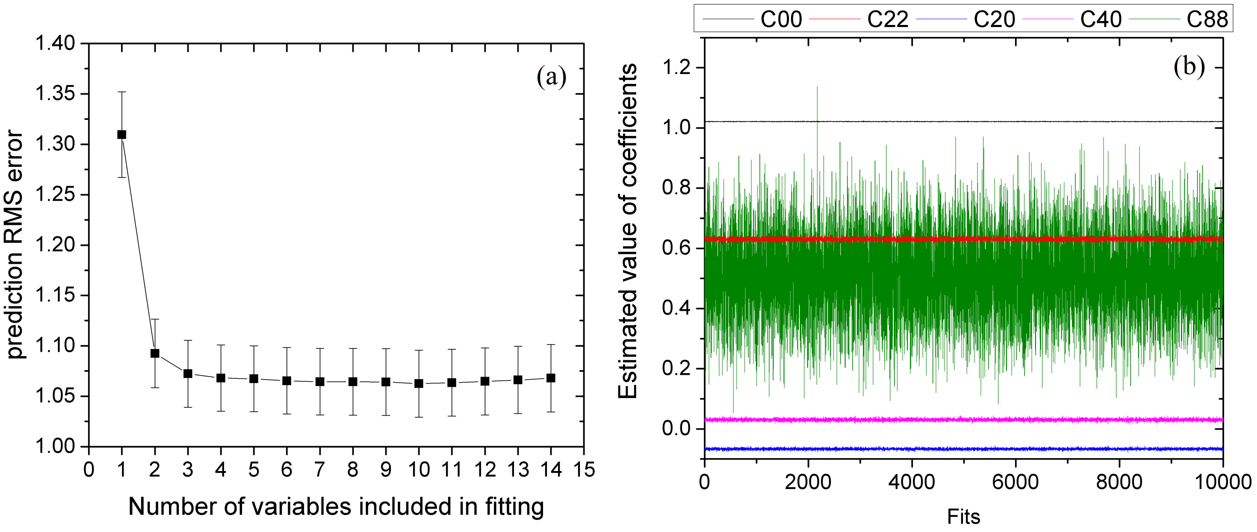

Figure 4.7: *(a) Prediction root-mean-square error of the models (Model n includes the first $n+1$ coefficients in the order mentioned in Table. 4.1). (b) Stability of the coefficients used in* SO_2^+ *fitting when the model consists of only these coefficients.*

The reduced model can explain up to about 90% of the delay scan variation (R-squared = 0.8973). Adding C_{20} and C_{40} increases R-squared to 0.9287 and the full model has R-squared of 0.9342. Fitting with the parsimonious model also yields the same rotational wave packet as before.

Coefficients	Reduced model	Full model
C_{00}	1.0237 ± 0.0006	1.0201 ± 0.0011
C_{20}	–	-0.0674 ± 0.0039
C_{22}	0.6363 ± 0.0070	0.6221 ± 0.0069

Table 4.2: *Comparison of coefficients using the "full model" and the reduced model.*

We have presented a quantitative fitting analysis; next, we would like to discuss some qualitative perspectives of the fit. The isotropic function $\langle D_{00} \rangle$ is always included in the fit, since we compare the angle-dependent ionization rate relative to the ionization of an isotropic distribution of the molecular axis. The resolution of other variables depends on molecular alignment and the experimental noise level ε. In reality, Eq. (2.35) should read

$$Y(t) = \sum_{JK} C_{JK} \langle D_{JK} \rangle (t) + \varepsilon, \tag{4.3}$$

This indicates that useful information can be learned by comparing the contribution of each term $C_{JK}\left\langle D_{JK}\right\rangle$ with the experimental noise level ε. Coefficients such as C_{22} and C_{20} have $C_{JK}\left\langle D_{JK}\right\rangle \gg \varepsilon$ (see Fig. 4.8) and can be determined with high resolution. On the other hand, although C_{88} appears to have better p-value compared to some other coefficients, its contribution $C_{JK}\left\langle D_{JK}\right\rangle \ll \epsilon$ is well below the noise level suggesting its correlation with the data is mostly coincident and that C_{88} cannot be resolved by the experiment.

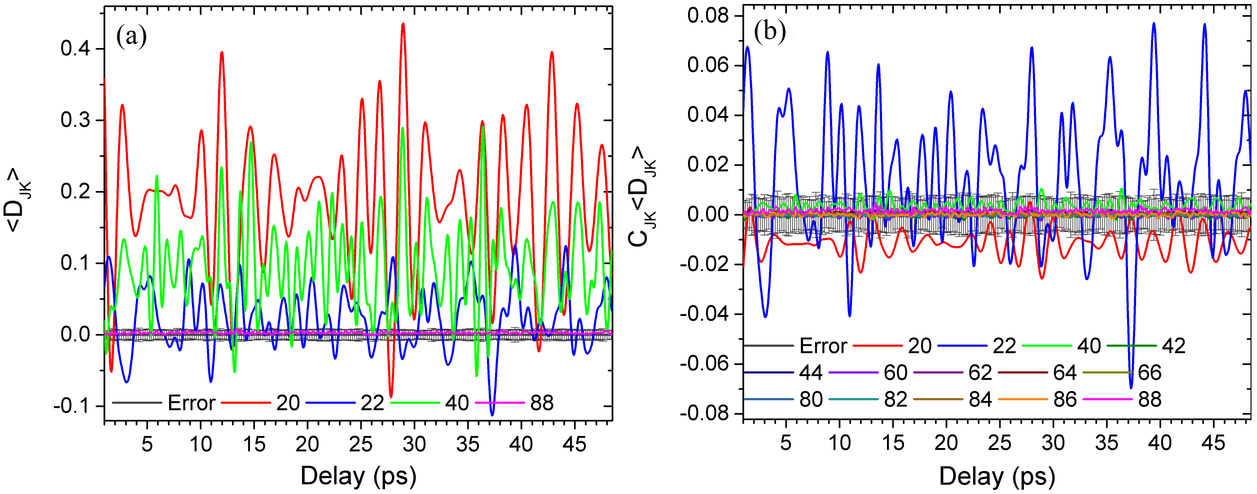

Figure 4.8: *A comparison of* $\left\langle D_{JK}\right\rangle$ *(a) and* $C_{JK}\left\langle D_{JK}\right\rangle$ *(b) with the experimental error of* 1σ *in* SO_2^+ *fit.*

Although the uncertainty of the retrieved angle-dependent ionization rate $S(\theta, \chi)$ is encoded in the uncertainty of the coefficients, it is difficult to quantify directly when multiple coefficients are involved. In order to visualize the uncertainty of $S(\theta, \chi)$, we use bootstrap re-sampling[160]. A bootstrap sample is a random sample of the data taken with replacement, meaning that a selected data point is still available for further selection. The bootstrap sample is the same size as the original data set. By retrieving $S(\theta, \chi)$ from fitting to a large number of bootstrap samples, we can estimate the mean of $S(\theta, \chi)$ and its standard deviation, as shown in Fig. 4.9. It is worth noting that the estimated values for C_{JK} and their standard deviation obtained by bootstrapping converge to those values obtained by linear regression earlier on the original data. For the reduced model, the standard deviation is very small compared to the mean of $S(\theta, \chi)$.

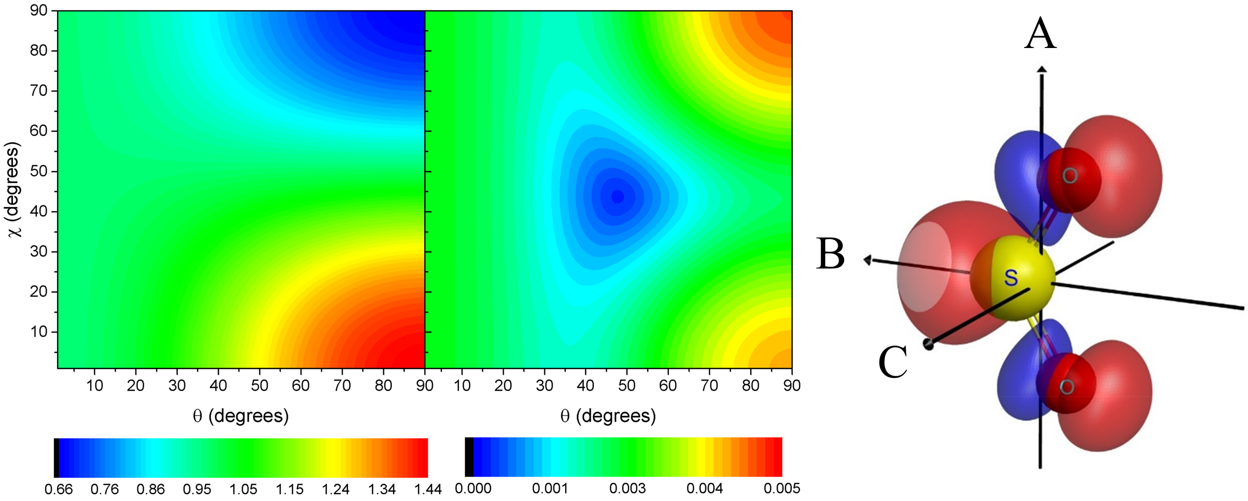

Figure 4.9: *The retrieved 2D angle dependence of the non-dissociative ionization* (SO_2^+) *(left) with the corresponding standard deviation (middle). The right panel shows the density profile of the highest occupied molecular orbital (HOMO) calculated using GAMESS with the Hartree–Fock method and visualized using MacMolPlt*[221].

From the retrieved pattern, we observe the maximum ionization rate at $\theta = 90°$, $\chi = 0°$ (*i.e.*, along the B axis) and the minimum ionization rate at $\theta = 90°$, $\chi = 90°$ (along the C axis). It is in agreement with the density profile of the highest occupied molecular orbital (HOMO), shown in the right panel of Fig. 4.9, where there is high density along the B axis and almost no density along the C axis.

The statistical analysis can help to eliminate fitting pitfalls caused by random error. However, it is also important to notice that the systematic errors, introduced by either our experimental apparatus or the calculation from presumably-known values, are much harder to detect. For example, the components of the polarizability tensor typically cannot be determined with very high accuracy (within about 6% for SO_2 as shown in Table. 4.3). In the case of linear molecules, the uncertainty in polarizability determination only affects the characterization of the laser fluence since only the polarizability anisotropy is involved. However, in the case of asymmetric top molecules, since all the components play roles in the interaction, the uncertainty affects the determination of not only the laser fluence but also the relative spatial distribution of the induced rotational wave packet in different directions. When two or three components are combined, the compounded errors can be pretty high. If one uses the theoretically calculated values[100] of the polarizability components, C_{66} appears to be a significant coefficient with the estimated value of $C_{66} = 1.276 \pm 0.123$ and a p-value of less than 2×10^{-16}. However, since its value changes significantly within the error bar of the polarizability, it cannot be resolved and hence should not be included. If we keep the polarizability floating as a fitting parameter, the ratio of α_2^2 and α_0^2 (see Eq. (2.23)) converges to the experimental value[222] within a few percent.

Polarizabilities	Theory	Experiment
α_{xx}	20.80	19.17 ± 1.15
α_{yy}	18.66	22.99 ± 0.73
α_{zz}	31.32	36.57 ± 1.76

Table 4.3: *Components of polarizability tensor of* SO_2 *in atomic unit. The theory values are from Pabst el al.*[100]*, the experimental values are from Lukins and Ritchie*[222].

Fig. 4.10 shows a comparison of the angle-dependent ionization rate of SO_2 predicted by MO-ADK and retrieved from ORRCS. In panel (a), we calculate the ionization rate of an oriented SO_2 molecule predicted by MO-ADK model using the structure coefficients taken from Zhao *et al.*[223]. In our experiment, the molecules are aligned but not oriented, so we symmetrize the result in panel (a) to get the ionization rate of an aligned molecule, as shown in panel (b). Panel (c) is the ionization rate retrieved from ORRCS (same as Fig. 4.9 but plotted in 3D). There are discrepancies between results from MO-ADK and ORRCS. While the MO-ADK result closely mimics the electron density of the HOMO, giving maximum ionization nearly along the SO bond axis, our experimental result is more isotropic, giving maximum ionization along the B axis. The AC nodal plane also does not show a clear signature along the A axis. Our ORRCS retrieval is in slightly better agreement with the MO-SFA calculation by Chen and He[219], where the ionization along the B axis is much more pronounced compared to MO-ADK. It is worth noting that the mentioned MO-ADK calculation only includes the HOMO, while that might not be the case in the experiment.

Angle-dependent ionization rates of polyatomic molecules predicted by different theories and models very often do not agree. For example, in the work on SFI of 1,3-butadiene (C_4H_6), Mikosch *et al.*[34] shows that MO-ADK and TD-RIS (time-dependent resolution-in-

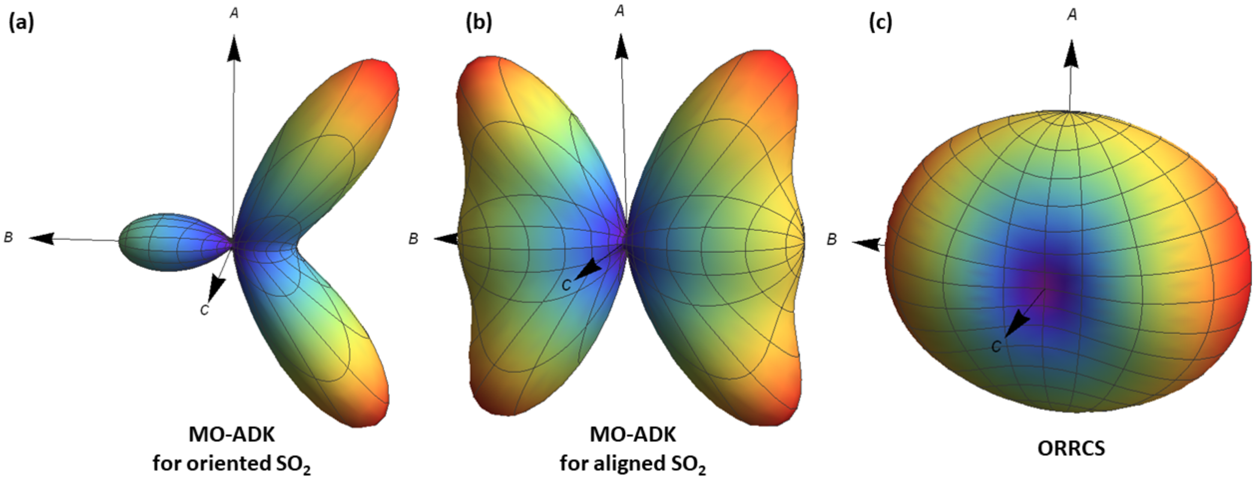

Figure 4.10: *Comparison between the angle-dependent ionization rate of* SO_2 *predicted by MO-ADK and retrieved from ORRCS. (a) Ionization rate of an oriented* SO_2 *molecule using MO-ADK model. (b) Same as (a) but the molecule is aligned, not oriented. (c) Same as (b) but the ionization rate is retrieved from ORRCS.*

ionic-states) predict different locations of minimum and maximum ionization. While MO-ADK closely mimics the electron density of the ionized orbital, showing a strong suppression of ionization along all nodal planes, TD-RIS predicts that suppression occurs only along the nodal plane perpendicular to the molecular plane, with little or no suppression along the π-like nodal plane that lies within the plane of the molecule. This phenomenon is further investigated for several ring-type molecules by Alharbi *et al.*[224]. They show that for furan and thiophene the maximum SFI occurs when the laser is near a nodal plane of the corresponding ionizing orbital. This behavior is different from 2,3-dihydrofuran, which follows the conventional expectation that maximum SFI occurs when the laser is away from nodal planes. This peculiar trend is probably also consistent with our experimental result here on SO_2 as well. Although we only have one nodal plane here, the ionization along the C axis (perpendicular to the molecular plane) is suppressed, and ionization along the A axis (in the molecular plane) does not show any signs of suppression. We also note that the angle-dependent ionization rate of C_2H_4 predicted by MO-ADK[223] also shows a different maximum location compared to MO-SFA[30], where MO-SFA has nicely reproduced the experimental result. More experimental results are crucial for further investigating the problem and building up better theories and models for SFI.

If a circularly polarized probe pulse is used to singly ionize the SO_2 molecule, the peak and trough of the angle dependence ionization rate $S^{\mathrm{cir}}(\theta, \chi)$ is reverse compared to that of the linearly polarized probe pulse as shown in Fig. 4.11. As discussed in chapter 2, in this case, the symmetry axis is the propagation axis $\vec{k}$ of the field, and hence, the angles are expressed with respect to $\vec{k}$ rather than the polarization axis of the field as used for a linearly polarized pulse. This angle-dependent yield pattern also qualitatively reflects the density profile of the HOMO. When $\vec{k}$ points along the C axis ($\theta = 90°$, $\chi = 90°$), the electric field sweeps over the AB plane where almost all of the density is, and the ionization rate is maximum. On the other hand, when $\vec{k}$ points along the B axis ($\theta = 90°$, $\chi = 0°$), the electric field sweeps over the AC plane where there is almost no density and the ionization rate has a minimum.

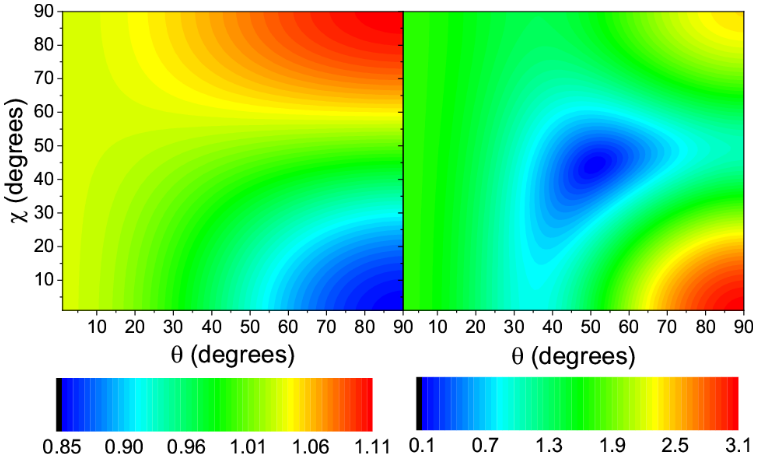

Figure 4.11: *The retrieved 2D angle dependence of the non-dissociative ionization* (SO_2^+) *probed by a circularly polarized pulse (left) with the corresponding standard deviation (multiplied by* 10^3*) (right).*

4.3 Conclusions

We have retrieved the angle dependence of the ionization probability of CO_2 using time-domain measurements on impulsively-excited rotational wave-packets. A high degree of alignment combined with good signal-to-noise ratio allows reliable retrieval of a large number of terms in a Legendre polynomial expansion, resulting in significantly higher resolution than prior measurements. The result is in good agreement with direct angle-scan measurements and is consistent with an independent experiment probed by a circularly polarized pulse. Although our experiment has shown high angular resolution, the angle-dependent ionization probability is mainly determined by the first three coefficients in Eq. (2.30). Coefficients with order higher than 4 were determined to be relatively small. This leads to a fair agreement of our final result with previous works at lower degrees of alignment by Thomann *et al.*[137] and Weber *et al.*[129], where Thomann *et al.* had used the expansion up to $J_{max} = 4$. The angle dependence of the ionization probability tends to have shallower peak-to-trough contrast at higher intensity while maintaining the overall shape.

We also retrieved the angle-dependent ionization rates of SO_2, an asymmetric top molecule, using the time-domain approach. The 2D angle dependence of strong-field non-dissociative ionization of SO_2 was retrieved without three-dimensional alignment and axial recoil approximation. Results from measurements with linearly and circularly polarized pulses are consistent with the density profile of the HOMO. This can provide more insights to further understand higher-order processes following the ionization event, and more data for testing theories and models on ionization of molecules in the strong laser field.

We also discussed in-depth and improved the retrieval algorithm of the ORRCS method. We pointed out that the convergence of the fit with the expansion of the angle dependence in the Legendre or Wigner basis, combined with further statistical analysis, can help in determining of the correct angle dependence. Data with high signal-to-noise ratio obtained by utilizing cold molecules, ultra-high vacuum, and multipulse alignment (see chapter 3) is important for accurately retrieving highly anisotropic distributions. We also discuss the importance of systematic errors with the measurement of polarizability components as an example. While the uncertainty in the determination of polarizability components does not affect the retrieval in linear molecules, it plays an important role in the retrieval of asymmetric top molecules.

The time-domain approach, not limited to molecular symmetry and laser polarization, is a promising method for simultaneously retrieving 2D angle dependence of physical processes and characterizing the rotational wave packet from time-domain measurements. It is the only method that was demonstrated to work for the non-dissociative ionization of asymmetric top molecules. The method shown here can, in principle, be used to characterize SFI at any wavelength. In particular, it would be useful to measure the angle-dependence of SFI using mid-IR lasers, including cases where the laser wavelength coincides with vibrational resonances. This information would be helpful for using LIED[25] to measure the molecular structure.

Chapter 5

Validating the axial-recoil approximation in the dissociation of molecules

In this chapter, we extend the time-domain method to photo-ion momentum measurements, where the axial recoil approximation is often used without validation. Within the axial recoil approximation, the fragments are assumed to recoil along the internuclear axis after the bond breaks. In order to test the validity of this approximation, it is necessary to measure the molecular axis distribution independent of the momentum distribution itself. We show that both of these distributions can be obtained by measuring the momentum distributions of fragments in a pump-probe experiment in which the molecules are impulsively aligned by a non-resonant pump and then dissociated by a probe pulse. The delay-dependent momentum distributions are analyzed using ORRCS to generate a 2D probability distribution function that directly reflects the validity of the axial recoil approximation. Experimentally, we examine the dissociation of CO_2 by a strong field (785 nm) and the dissociation of N_2 by a broadband ultraviolet pulse (262 nm). The work on CO_2 (Sec. 5.1-5.3 and part of Sec. 5.6) is an edited version of the discussions published in Physical Review A[31]. © APS.

5.1 Motivation

In the previous chapter, we discussed non-dissociative single ionization by linear and circularly polarized pulses; in this chapter, we shift our attention to dissociative double ionization by linearly polarized light. In dissociative ionization, not only the ionization probability, but also the angular distribution of the ions carries useful information. For example, the measured momentum distribution of the fragments can be used to reconstruct the molecular axis distribution in experiments with aligned molecules (Sec. 1.2.2) or to reconstruct the body frame of the molecules in measurements of MFPADs using coincident fragment imaging (Sec. 1.2.1). However, this reconstruction may be hampered by probe selectivity (angle-dependent probability of the production of the fragment by the probe) and non-axial recoil[110–114]. Fig. 5.1 shows the directions of the molecular axis $\hat{m}$ and the asymptotic momentum of the fragment ions $\hat{k}$ and the definitions of angles used in the following discussion. The molecular axis is shown at $\phi = 0°$. Due to axial symmetry of the laser field along the polarization axis (linearly polarized light), the value of ϕ is not physically relevant, but we do lose the relevant angle $\phi_k - \phi$ due to this symmetry in the measurement. The molecular axis distribution can be obtained directly from the momentum distribution only if the vectors $\hat{m}$ and $\hat{k}$ coincide.

In this chapter, we demonstrate an experimental method to check whether molecular fragmentation by ultrafast pulses satisfies the axial recoil approximation. The basic idea is that we measure the angular distribution of the fragments as a function of the pump-probe delay and compare it with the distribution of the molecular axis retrieved from the time evolution of the momentum distribution. Making this comparison for many different distributions from the time evolution of the rotational wave packet, we generate a probability distribution function that directly reflects the validity of the axial recoil approximation (the mathematical description is given in section 5.2). Due to the loss of the angle $\phi_k - \phi$ as discussed above, the full probability distribution $S(\vec{m}, \vec{k})$ is reduced to $S(\theta, k, \theta_k)$. The angle-dependent probability of producing the fragment by the probe is also obtained simultaneously from the delay dependence of the fragment yield in the same manner as we analyze angle-dependent ionization, and is used to account for probe selectivity in the analysis. As an example, we discuss the application of this method to the fragmentation of CO_2 by an intense, 35 fs, 785 nm pulse in the following sections.

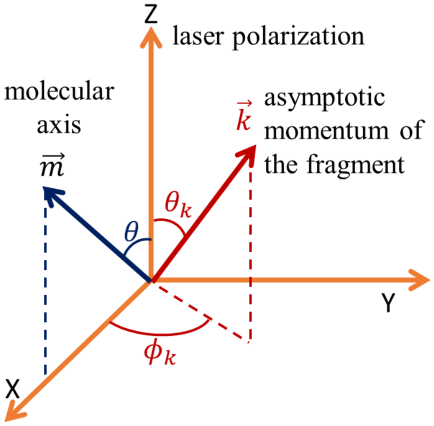

Figure 5.1: *Definition of angles describing the orientation of molecules (polar angle θ and azimuthal angle ϕ) and asymptotic momentum of the fragments (polar angle θ_k and azimuthal angle ϕ_k); Z defines the polarization axis in LF. The molecular axis distribution can be obtained directly from the momentum distribution only if the vectors $\vec{m}$ and $\vec{k}$ coincide. As mentioned in the text, the value of ϕ is not physically relevant, and the relevant angle $\phi_k - \phi$ is lost, so the molecular axis is shown here at an arbitrarily chosen angle $\phi = 0°$.*

In general, $\hat{m}$ should represent the direction of a bond axis (internuclear axis) in the molecule while $\hat{k}$ describes the momenta of the fragments corresponding to that bond, since the axial-recoil approximation applies to a bond and not the molecule. For linear molecules, the molecular axis and the internuclear axis are the same and hence are used interchangeably in this chapter. However, it is worth noting our test of the axial-recoil approximation is not limited only to linear molecules.

5.2 Time-domain approach using ORRCS for momentum measurements

Our goal is to determine the probability distribution $S(\theta, k, \theta_k)$ of the probe pulse producing a fragment ion with momentum k in the direction θ_k from a molecule whose axis is at angle

θ. To facilitate the determination of this function from experimental data, we express the angular dependence in a basis of the product of two Legendre polynomials $P_J(\cos\theta)P_L(\cos\theta_k)$ and the magnitude of the momentum in a discrete Gaussian basis as

$$S(\theta, k, \theta_k) = \sum_{k_0,J,L} A_{k_0JL}\mathrm{e}^{-\frac{(k-k_0)^2}{2\sigma_b^2}} P_J(\cos\theta)P_L(\cos\theta_k), \tag{5.1}$$

where k_0 are the centers of the radial Gaussian functions and σ_b is the width of each of these functions. This choice of basis was motivated by the pBasex algorithm[225] that we use to analyze VMI data.

The delay-dependent momentum distribution of the fragment ion in the LF, $M(k, \theta_k, t)$, is the convolution of $S(\theta, k, \theta_k)$ and the delay-dependent molecular axis distribution, $\rho(\theta, t)$, produced by the aligning pulse,

$$M(k, \theta_k, t) = 2\pi \int \rho\,(\theta, t)\, S(\theta, k, \theta_k) \sin\theta d\theta. \tag{5.2}$$

Substituting Eq. (5.1) into Eq. (5.2), we have

$$M(k, \theta_k, t) = 2\pi \sum_{k_0,J,L} A_{k_0JL} e^{-\frac{(k-k_0)^2}{2\sigma_b^2}} \langle P_J(\cos\theta)\rangle(t) P_L(\cos\theta_k). \tag{5.3}$$

where $\langle P_J(\cos\theta)\rangle(t) = \int \rho(\theta, t)P_J(\cos\theta)\sin\theta \mathrm{d}\theta$ are delay-dependent axis distribution moments.

In this experiment, we do not measure $M(k, \theta_k, t)$ directly but only the 2D projection of the charge sphere on the VMI detector at each delay (see Sec. 3.7 and Sec. 3.8.3). Due to the axial symmetry of the momentum distribution, we can reconstruct $M(k, \theta_k, t)$ from the data by applying the pBasex method[225] at each delay to obtain a set of delay-dependent coefficients $C_{k_0L}(t)$ that represent $M(k, \theta_k, t)$ as

$$M(k, \theta_k, t) = 2\pi \sum_{k_0,L} C_{k_0L}(t) e^{-\frac{(k-k_0)^2}{2\sigma_b^2}} P_L(\cos\theta_k). \tag{5.4}$$

Comparing Eqs. (5.3) and (5.4), we get

$$C_{k_0 L}(t) = \sum_J A_{k_0 J L} \left\langle P_J(\cos\theta) \right\rangle (t), \tag{5.5}$$

which is identical in form to Eq.(2.31) and can be solved in the same manner by linear regression. One important difference is that Eq.(5.5) is a large set of equations (one for each pair of k_0 and L), which allows for additional consistency checks since all the fits should converge to the same rotational wavepacket parameters (pump fluence and rotational temperature).

In the measurements, a channel usually spans a finite range of the radial momentum k (radial width), so we need to integrate over that range of k for each channel. Usually, over the spanned range of k, the channel has the same angular distribution and the integration simply increases the statistics. On the other hand, if the fragment angular distribution behaves differently within the energy spectrum, this indicates that a measurement with higher energy resolution should be done to finely resolve all the involved states or channels.

The fragment angular distribution of a single channel in the LF can also be described in terms of the widely-used asymmetry parameters β_L[145] as

$$M(k, \theta_k, t) = \frac{\sigma(k,t)}{4\pi} \left[1 + \sum_{\text{even L}} \beta_L(k,t) P_L(\cos\theta_k) \right], \tag{5.6}$$

where $\sigma(k,t)$ is the total (angles θ_k and θ integrated) fragmentation cross section; the time dependence comes from the dependence on the molecular axis distribution $\rho(\theta, t)$. Putting Eq. (5.4) and Eq. (5.6) in the same form, the asymmetry parameters—averaged over the range of k for the channel—can be written as

$$\beta_L(\bar{k}, t) = \frac{C_{\bar{k}L}(t)}{C_{\bar{k}0}(t)} \tag{5.7}$$

and the total angle-integrated cross section is $\sigma(\bar{k}, t) = 8\pi^2 C_{\bar{k}0}(t)$.

5.3 Dissociation of CO_2 in a strong field

In this section, we apply the analysis discussed in section 5.2 to the fragmentation of CO_2 by an intense, 35 fs, 785 nm pulse with data acquired by the method described in the section on VMI measurements with the Tpx3Cam (Sec. 3.8.3). At a probe-pulse intensity of 1×10^{15} W/cm^2, CO_2 molecules can be doubly ionized and dissociate into CO^+ and O^+ fragments. The ions corresponding to this channel can be discriminated from other channels in the VMI images using momentum and energy conservation, assuming a Coulomb explosion. This identification, shown in Fig. 5.2, is in good agreement with data from coincidence measurements[226]. In our data, either CO^+ or O^+ can be selected by putting a gate of 300 ns on the recorded ToA. By doing so, we mostly look at the prompt breakup, but there can still be some contribution from long-lived CO_2^{2+}[226]. The raw VMI images in Fig. 5.2 show the asymptotic momentum spectra of CO^+ and O^+ at aligned and antialigned peaks. The circles indicate the range of radial momentum that was integrated over in the analysis.

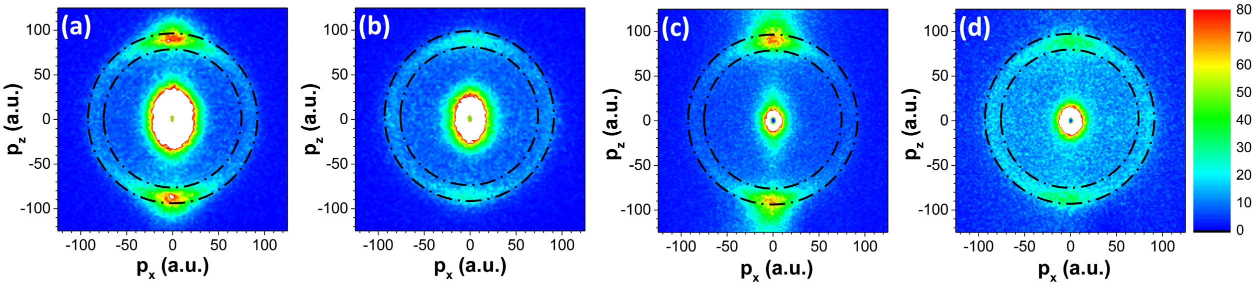

CO^+, aligned, 21.1ps — CO^+, anti-aligned, 42.5ps — O^+, aligned, 21.1ps — O^+, anti-aligned, 42.5ps

Figure 5.2: *VMI images of* CO^+ *and* O^+ *at the aligned (a,c) and antialigned (b,d) peaks. The laser polarization is along the* p_z *direction. The linear color scale expresses the yield of the ions in arbitrary units; the same scale is used in all four images. The circles indicate the regions of interests corresponding to the fragmentation of* CO_2^{2+} *into two singly charged ions (note that a specific channel was selected from the inverted data, not on the raw data). Fragments with low energy coming from singly-charged molecular ion are saturated on the color map for display purposes.*

The time evolution of the asymmetry parameters $\beta_L(k,t)$ and the angle-integrated cross section $\sigma(k,t)$ together with their corresponding fits for CO^+ fragments are shown in Fig. 5.3. We obtained excellent fits up to $L = 14$ with $J_{max} = 14$, although the fits already converge from $J_{max} = 6$ (J_{max} determines the truncation of Eq. (5.1)).

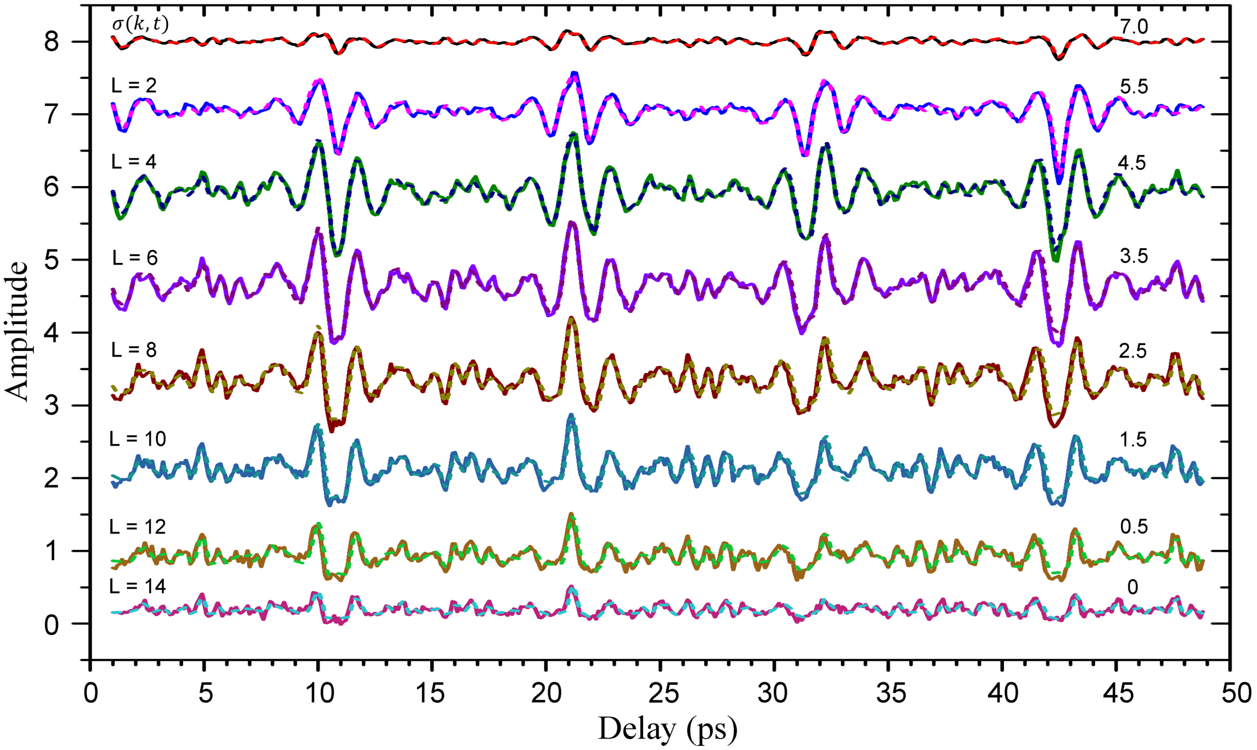

Figure 5.3: *Time evolution of the asymmetry parameters* $\beta_L(k,t)$ *(solid) and the angle-integrated cross section* $\sigma(k,t)$ *together with their corresponding fits (dashed) for* CO$^+$ *fragments at a probe intensity of* 1×10^{15} W/cm^2*. The aligning pump pulse in this case is about* 150 fs*,* 20 TW/cm^2*. The asymmetry parameters are unitless and* $\sigma(k,t)$ *is normalized by its mean. For clarity, each plot was shifted vertically by an amount indicated by the number on the right side.*

A single alignment pump (150 fs, 20 TW/cm^2) was used in this measurement. The fluence of the aligning pulse and the rotational temperature of the gas (around 2 K) are retrieved consistently from fits with different $\beta_L(k,t)$ and $\sigma(k,t)$ for both O$^+$ and CO$^+$ fragments as seen in Fig. 5.4. From these fits, we get A_{k_0JL} coefficients and determine the angle-dependent probability $S(\theta, k, \theta_k)$; the retrieved function is shown in Fig. 5.5(b). While the asymmetry parameters $\beta_L(k,t)$ (and A_{k_0JL} coefficients) determine the angular distribution in the LF (and MF), the probe selectivity $F(\theta)$ is also obtained simultaneously in the measurement by fitting to the time evolution of the angle-integrated cross section $\sigma(k,t)$. $F(\theta)$, which can also be interpreted as the fragmentation rate, is the probability of making a given fragment as a function of molecular orientation (θ) in the laser field as shown in Fig. 5.5(a). $F(\theta)$ can also be obtained by integrating $S(\theta, k, \theta_k)$ over θ_k. Both methods give consistent results.

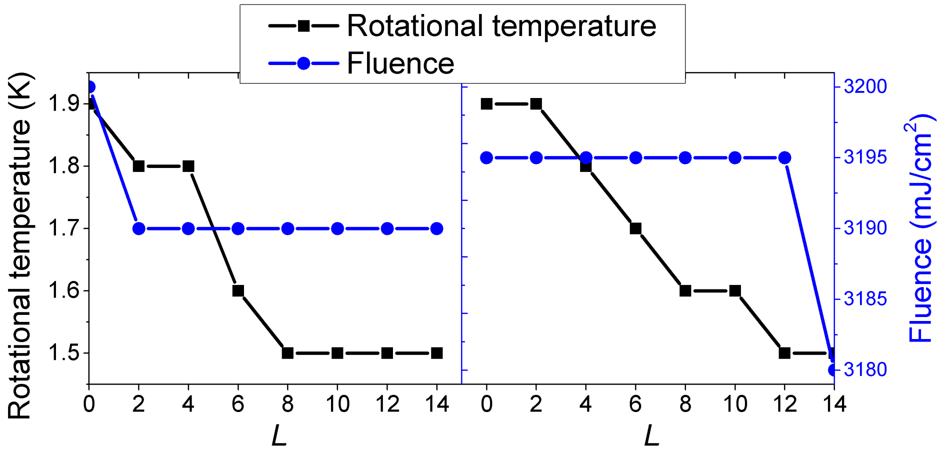

Figure 5.4: *The fluence of the aligning pulse and the rotational temperature of the gas, which determine the rotational wave packet, are retrieved consistently from fits with different asymmetry parameters* $\beta_L(k,t)$ *for both* O^+ *(left panel) and* CO^+ *(right panel) fragments. This indicates the reliability of the retrieval procedure. At the value of* $L = 0$*, since* β_0 *is always 1, we are showing parameters retrieved from the fit on the cross-section* $\sigma(k,t)$ *instead. The role of the fluence and the rotational temperature in the fit was discussed in Sec. 2.2.*

We can now correct for the probe selectivity by normalizing each vertical line of $S(\theta, k, \theta_k)$ by $F(\theta)$. The new function $D(k, \theta_k|\theta)$ shown in Fig. 5.5(c) expresses the conditional probability for a fragment to fly out at θ_k given that the fragment is created from a molecule that was aligned along θ prior to the probe pulse. In this case, since $F(\theta)$ is not a very sharp function (with a maximum to minimum ratio of about 1.7), $D(k, \theta_k|\theta)$ enhances some features (as discussed below) but does not differ significantly from $S(\theta, k, \theta_k)$.

If the asymptotic momentum of the fragment is a good representation of the initial orientation of the neutral molecule, then $\theta_k \approx \theta$ and hence a diagonal band should be observed. However, in the $D(k, \theta_k|\theta)$ plot (Fig. 5.5(c)), there is only a very weak trend along the diagonal line while the major trend peaks along the laser polarization direction ($\theta_k = 0$) regardless of the initial orientation of the molecules. This clearly shows a breakdown of the axial recoil approximation (i.e., the asymptotic momentum angular distribution of the fragment does not reflect the molecular axis distribution before the probe pulse). The molecules are likely to undergo significant realignment during the process.

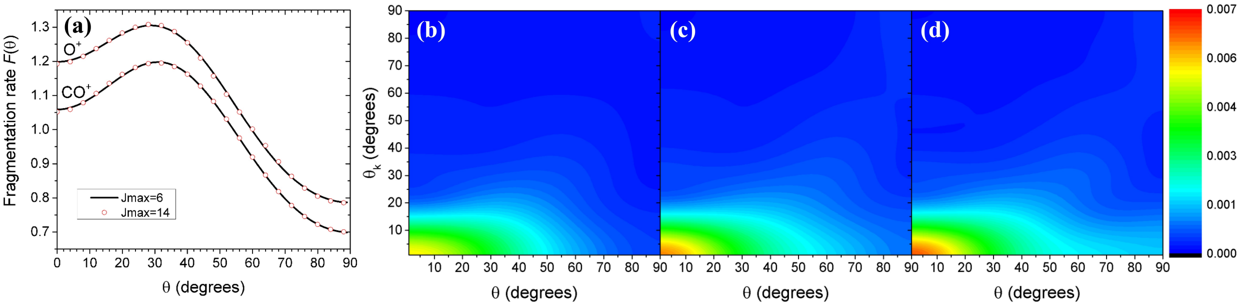

Figure 5.5: *(a) The fragmentation yield $F(\theta)$ expressing the probability of producing the fragment as a function of initial molecular orientation θ relative to the probability from an isotropic ensemble. For display purpose, $F(\theta)$ for O^+ is shifted up by 0.1. (b) Angle-dependent probability $S(\theta, k, \theta_k)$, for the channel indicated in Fig. 5.2, expressing how the angular distribution of the CO^+ fragment depends on the orientation of the molecule relative to the laser polarization. (c) Angle-dependent conditional probability $D(k, \theta_k|\theta)$ expressing the probability for a fragment to fly out at θ_k given that the fragment is created from a molecule that was aligned along θ prior to the probe pulse. (d) $D(k, \theta_k|\theta)$ plot for O^+ fragment coming from the same channel.*

In our experiment, the estimated antialignment peak is sharp with $\langle \cos^2\theta \rangle \approx 0.1$, so molecules are well confined near the plane perpendicular to the polarization axis (horizontal plane). Hence, the distribution should be observed as a line along the p_x axis if the axial-recoil approximation is held strongly, which is not the case as seen from the raw images (Fig. 5.2). Using the retrieved $S(\theta, k, \theta_k)$, we estimate $\langle \cos^2\theta_k \rangle$ of an isotropic distribution measured by this probe on this channel to be about 0.51, in good agreement with the value of 0.506 calculated from the 3D distribution reconstructed by pBasex inversion.

As mentioned in Sec. 3.8.3, the time-stamping pixel detector Tpx3Cam allows us to simultaneously measure all the fragment ions. Analysis of O^+ momenta measured simultaneously (but not in coincidence because the count rate was too high for coincident detection) shows very similar results (see Fig. 5.4 and Fig. 5.5).

It is worth noting that our experiment cannot distinguish whether the realignment happens during the (double-)ionization step ($CO_2 \rightarrow CO_2^{2+}$) or during the subsequent fragmentation of the dication ($CO_2^{2+} \rightarrow CO^+ + O^+$). The result is the total effect from neutral molecules to fragments ($CO_2 \rightarrow CO_2^{2+} \rightarrow CO^+ + O^+$).

We would like to mention that this experiment is closely related to other work on imaging the rotational wave packets using momentum measurements[227–229], since those measurements require the axial recoil of the fragments to a certain extent. While the probe selectivity (angle-dependent ionization probability) has been previously considered and minimized in those pump-probe arrangements, the realignment of molecules in the strong laser field was not discussed explicitly. This effect can be avoided by probing a subset of molecules where the torque exerted by the laser field is small[227] or choosing the observables that are independent of the realignment[229]. In our analysis, it is equivalent to looking at molecules near $\theta_k \approx 90°$. In that vicinity, CO_2 molecules also follow axial-recoil breakup to a certain extent indicated by the local maxima (top-right corners) of the $D(k, \theta_k|\theta)$ plots in Fig. 5.5(c-d).

5.4 An alternative perspective

In the previous section, we presented a method to generate a 2D probability distribution. This method is powerful, providing complete information about the dependence of the dissociation of molecules on their initial orientations in the laser field. However, the method also requires high-quality fits for many high-order asymmetry parameters β. This may not be possible in some cases where the count rate is low. In this section, we use a slightly different approach that provides less information but does not require fitting to all the asymmetry parameters.

Let us recall all the elements we need to validate the axial-recoil approximation: the molecular axis distribution of molecules, the angle-dependent fragmentation probability, and the distribution of the fragment ions. As discussed before, an ORRCS fit on the time-dependent yield of the fragment simultaneously gives us the first two elements (the time-dependent molecular axis distribution of molecules and the angle-dependent fragmentation probability) (see Sec. 2.2.1), and the VMI measurements of the fragment ions would give us a convoluted effect of all three elements (see Eq. (5.2)). If the molecules follow axial-recoil dissociation, the distribution of the fragment ions after accounting for the angle-dependent fragmentation rate should reflect the molecular axis distribution. We will plot both of them for comparison. Using this approach, we only need to do one ORRCS fit on the delay-dependent yield of the channel.

Mathematically, Eq. (5.2) can be written as

$$M(k,\theta_k,t) = 2\pi \int \rho\left(\theta,t\right) F(k,\theta) D(\theta,k,\theta_k|\theta) \sin\theta d\theta, \tag{5.8}$$

where we have replaced $S(\theta,k,\theta_k)$ with the product of the angle-dependent fragmentation rate $F(k,\theta)$ and the 2D probability function describing dissociation $D(\theta,k,\theta_k|\theta)$ as discussed in Sec. 5.3. If we have axial-recoil dissociation, the molecule initially at angle θ will produce fragments at angle $\theta_k = \theta$ and $D(\theta,k,\theta_k|\theta)$ will become

$$D(\theta,k,\theta_k|\theta) = \frac{1}{2\pi\sin\theta}\delta(\theta-\theta_k). \tag{5.9}$$

Substituting this into Eq. (5.8), we have

$$M(k,\theta_k,t) = \int \rho\left(\theta,t\right) F(k,\theta)\delta(\theta-\theta_k) d\theta, \tag{5.10}$$

or equivalently,

$$\rho\left(\theta,t\right) = \frac{M(k,\theta_k,t)}{F(k,\theta)}. \tag{5.11}$$

In the next section, we will use this method to evaluate the dissociation of N_2 by broadband ultraviolet pulses.

5.5 Dissociation of N_2 by broadband ultraviolet pulses

In this section, we study the dissociation of N_2 by UV pulses. N_2 is a diatomic molecule and does not have vibrational modes that make the molecule nonlinear like CO_2. The probe field is much weaker compared to the strong field used in the CO_2 experiment (Sec. 5.3), hence, we expect the realignment of molecules during the pulse to be much weaker. Fig. 5.6 shows the distributions of N^+ fragments recorded with our VMI spectrometer under different probe intensities of (a) 3 TW/cm^2, (b) 6 TW/cm^2, and (c) 9 TW/cm^2.

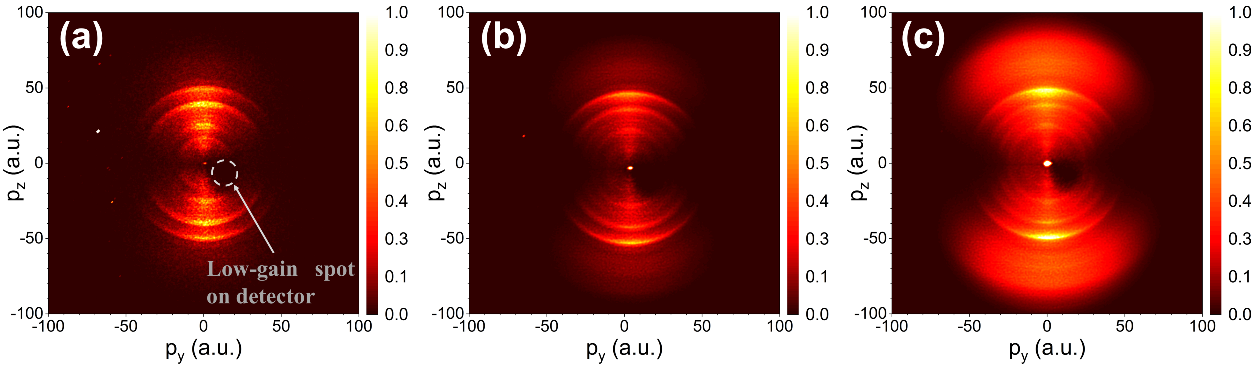

Figure 5.6: *Distributions of* N$^+$ *fragments recorded under different probe intensities of (a)* 3 TW/cm^2*, (b)* 6 TW/cm^2*, and (c)* 9 TW/cm^2.

In these images, a series of sharp rings of N$^+$ ions appear from low intensity. At higher intensities, we see more and more contribution from a broader feature at higher energy (momentum above 50 a.u.). The dot at the image center is from N_2^{2+}. It is brighter at higher intensities suggesting that the broad, high energy N$^+$ lobe is the product of double ionization ($N_2^{2+} \rightarrow N^+ + N^+$). A comparison of the momentum distribution of N$^+$ between the 3ω (262 nm) and the ω (785 nm) probes is shown in Fig. 5.7. This calibration, in good agreement with previous measurements[230–232], confirms that the high kinetic energy N$^+$ ions appear in the range of the double ionization products. We will focus on this channel where the range of selection is indicated by the white circles in panel Fig. 5.7(c).

Following our standard ORRCS scheme, we use fundamental pulses (785 nm, 150 fs, 17.4 TW/cm^2) to align cold N_2 molecules ($\approx$ 6 K) and then use UV pulses (262 nm, 190 fs, 9 TW/cm^2) to ionize them. We record images of N$^+$ fragments as a function of pump-probe delay with our VMI spectrometer. Fig. 5.8(a-c) show a strong modulation of the N$^+$ distributions with the rotational wave packet at alignment (a, $t = 3.95$ ps), a transient distribution (b, $t = 6.9$ ps), and antialignment (c, $t = 8.1$ ps).

We invert the VMI image at each delay step using the pBasex method, obtaining the angle-integrated cross section $\sigma(\bar{k}, t)$ and the asymmetry parameters $\beta_L(\bar{k}, t)$ as described in Sec. 5.2. However, now, we only do the ORRCS fit on $\sigma(\bar{k}, t)$, not on $\beta_L(\bar{k}, t)$. As shown in

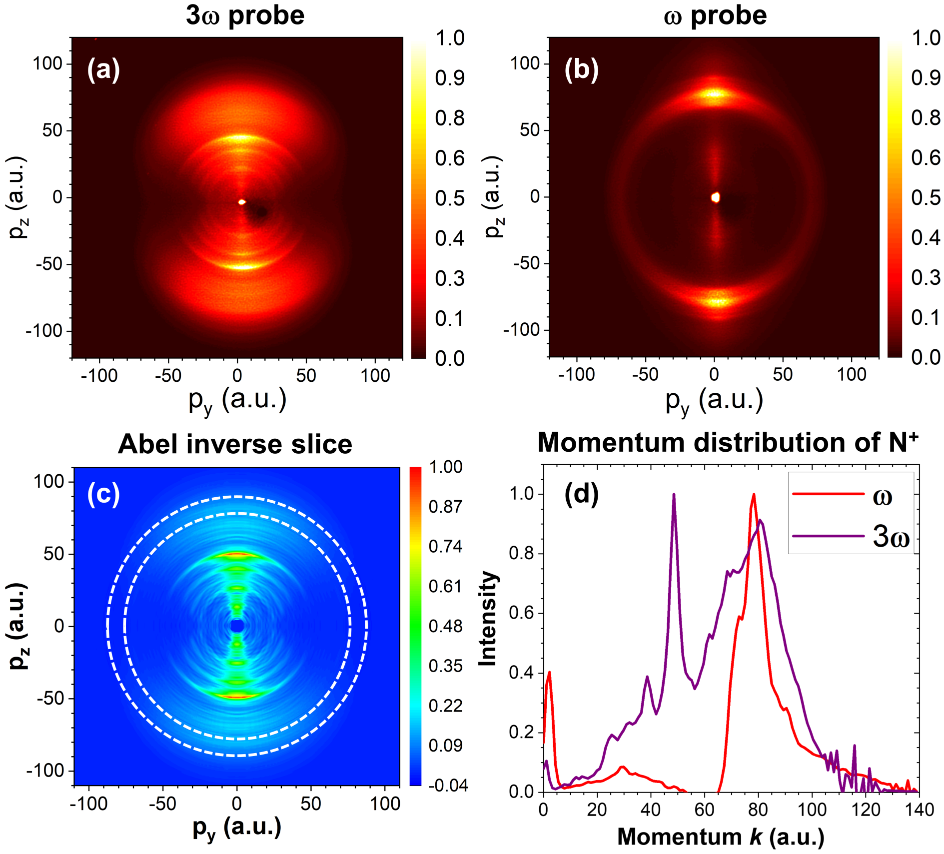

Figure 5.7: N$^+$ *image with 3 ω probe (a), and ω probe (b). (c) Abel inverse slice of (a). (d) Momentum distributions of* N$^+$ *fragments dissociated by ω and 3 ω pulses.*

Fig. 5.8, an ORRCS fit on $\sigma(\bar{k}, t)$ (d) simultaneously gives us the pump parameters and gas temperature that determine the rotational wave packet (150 fs, 17.4 TW/cm^2, 6 K), and the angle-dependent fragmentation rate $F(\bar{k}, \theta)$ (e). The retrieval of the rotational wave packet is consistent with other channels. The probability of fragmentation for molecules along the laser polarization is about 20 times higher than for molecules perpendicular to the laser polarization.

The asymmetry parameters $\beta_L(\bar{k}, t)$ allow us to reconstruct the 3D distribution $M(\bar{k}, \theta_k, t)$ of N$^+$ fragments for the channel. We correct this distribution with the angle-dependent fragmentation rate $F(\bar{k}, \theta)$ as in Eq. (5.11). A direct comparison of this quantity with the molecular axis distribution obtained from the fit is shown in Fig. 5.9. We can see, in panel (a), that the yield-corrected distribution of N$^+$ fragments (upper half) reflects the main

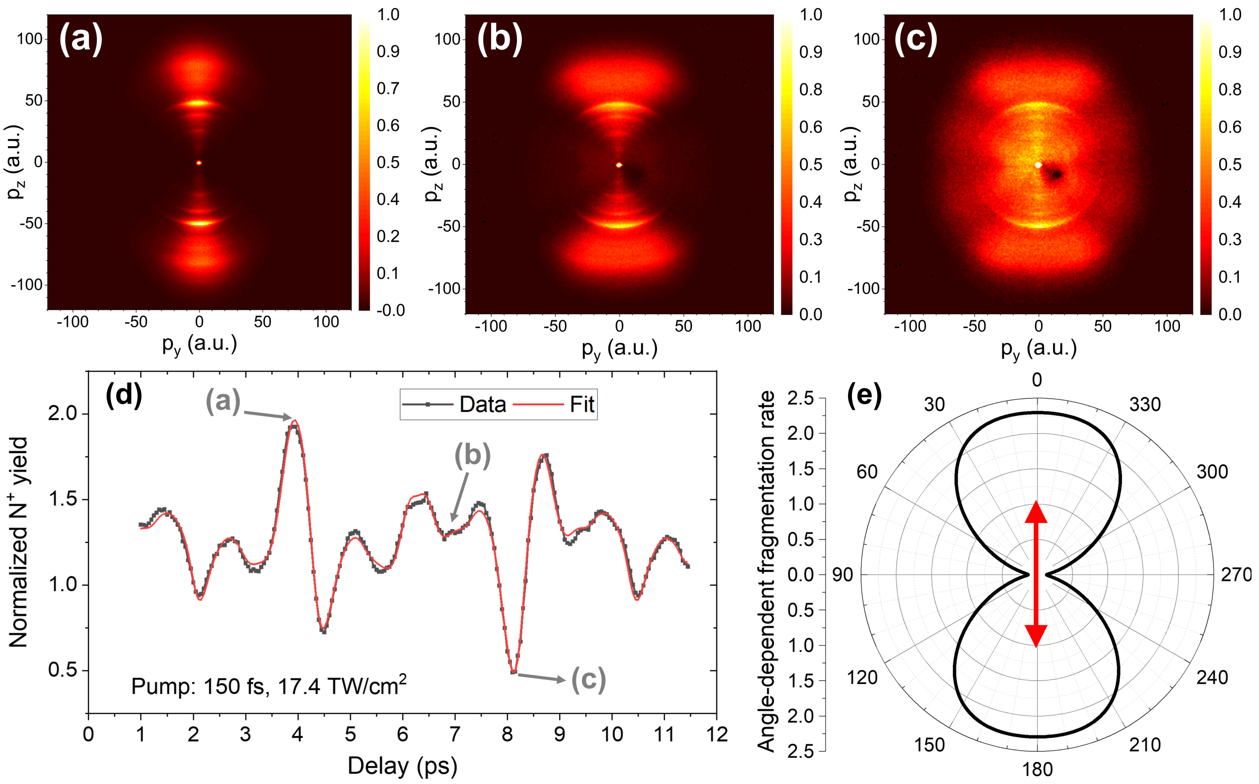

Figure 5.8: *(a-c) Images of* N^+ *fragments at aligned (a), transient (b) and antialigned (c) distributions. (d) Data and fit on the normalized* N^+ *yield. (e) The angle-dependent fragmentation rate obtained from the fit.*

features of the molecular axis distribution $\rho(\theta, t)$ (lower half). In the distribution of N^+ fragments, the features near $\theta_k = 0°$ are more intense, while the features near $\theta_k = 90°$ are less intense compared to the corresponding features in $\rho(\theta, t)$. Some features also move closer to the polarization axis $\theta_k = 0°$. These can be seen more clearly in the polar plots in panel (b-d) where the distribution of N^+ fragments tends to exaggerate peaks close to the laser polarization axis. At $t = 6.90$ ps, the peak near $\theta = 30°$ in $\rho(\theta, t)$ also appears closer to $\theta_k = 20°$ in the N^+ distributions.

We perform the same analysis for all the channels. Fig. 5.9(e-g) show the yield-corrected distributions of N^+ fragments for all the channels at aligned (e), transient (f), and antialigned (g) distributions. While the distributions of high energy N^+ ions (momentum greater than 50 a.u.) vary and mimic the distributions of the molecular axis, the distributions of low energy N^+ ions (momentum lower than 50 a.u.) always peak along the laser polarization

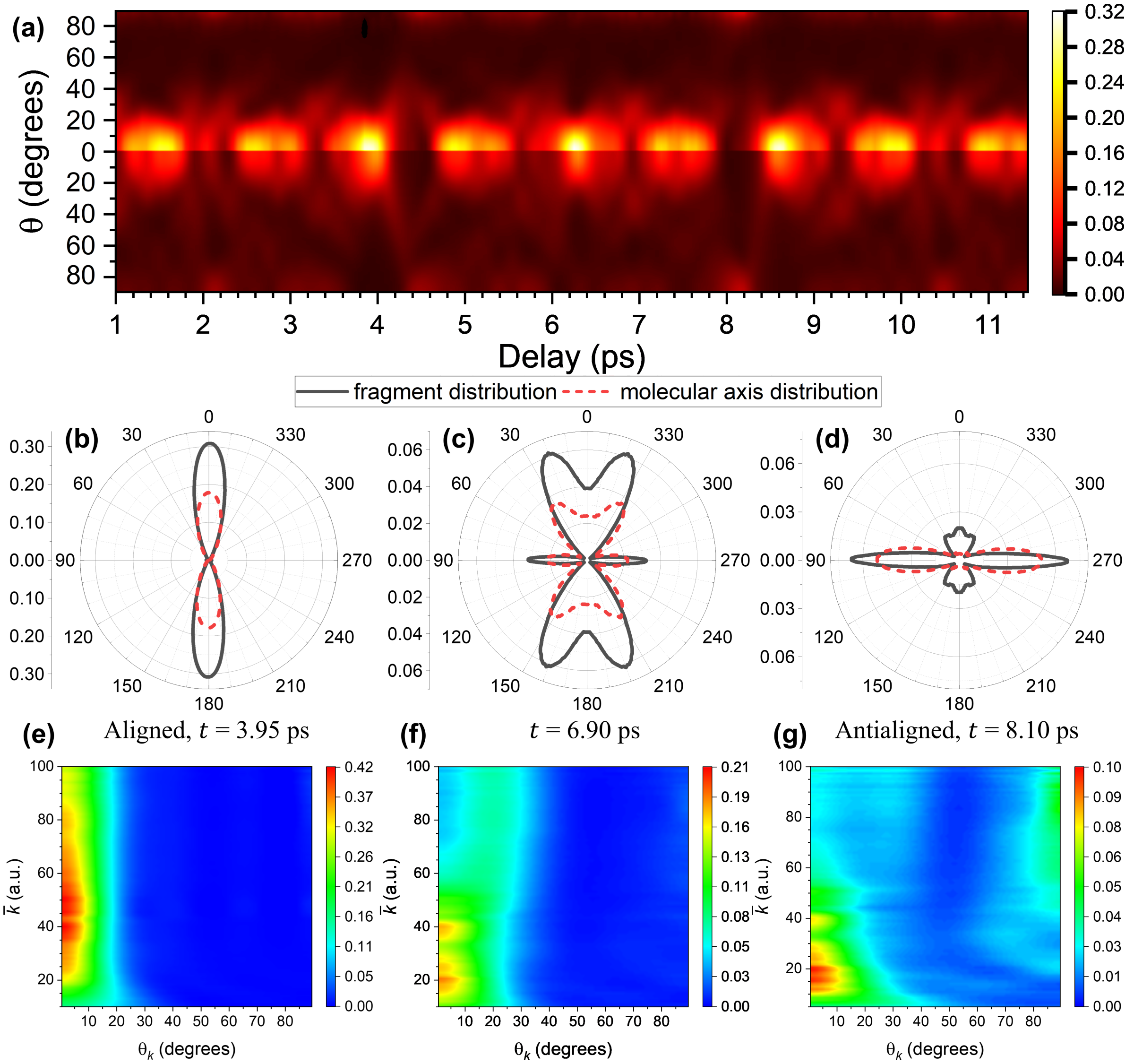

Aligned, t = 3.95 ps

t = 6.90 ps

Antialigned, t = 8.10 ps

Figure 5.9: *A comparison between distributions of the molecular axis and the* N^+ *fragments (a). (b-d) Slices of (a) at aligned (b), transient (c), and antialigned (d) distributions. (e-g) Distributions of* N^+ *fragments for all the channels at the same time as (b-d).*

axis ($\theta = 0°$).

The series of low energy N^+ rings are interesting features that are not observed in strong-field dissociation (see Fig. 5.7). They appear at low probe intensity, and energetically they can come from different vibrational levels of the C state of the cation[233,234], whereas the A and B states of the cation are stable. However, since the predissociation lifetimes of these vibrational levels are from tens of picoseconds to nanoseconds[234], the molecules should forget their initial orientations and the distributions of N^+ ions should not peak along the laser polarization axis as we observe in this experiment. We also observe a transition in the angle-dependent fragmentation rate from a dumbbell shape perpendicular to the polarization axis to a butterfly shape and then to a peanut shape along the polarization axis as the energy of these N^+ fragments gets higher (see Fig. 5.10). This suggests that a light-induced coupling might be involved[235]. However, the picture is not clear to us yet with our available data; the mechanism of producing these rings still needs further investigation, for example, with probes at different wavelengths. It would be interesting to be able to identify the origin of these states and discover why they behave differently.

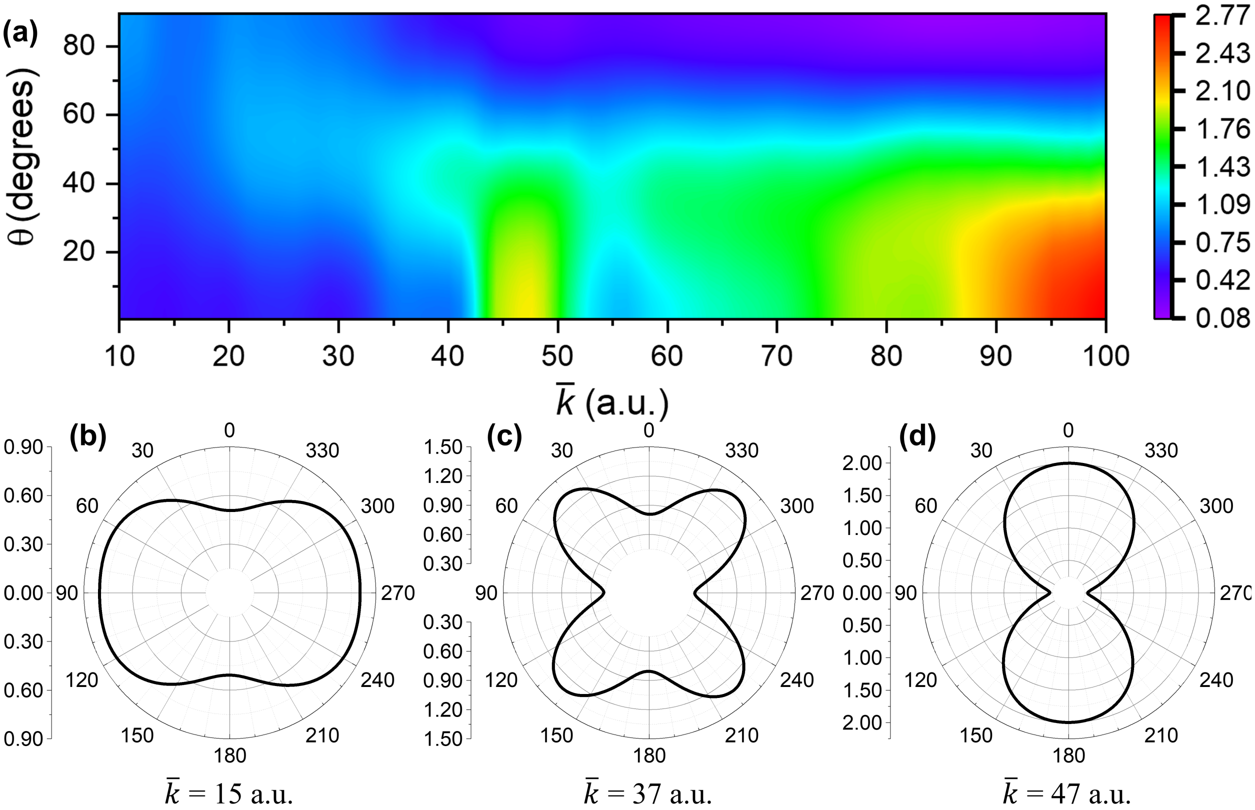

$\bar{k}$ = 15 a.u. $\bar{k}$ = 37 a.u. $\bar{k}$ = 47 a.u.

Figure 5.10: *(a) Angle-dependent fragmentation rate as a function of N^+ momentum. (b-d) Vertical slices of (a) at momentum $\bar{k} = 15$ a.u. (b), $\bar{k} = 37$ a.u. (c) and $\bar{k} = 47$ a.u. (d).*

5.6 Conclusions

We have developed a method to retrieve the probability function $S(\theta, k, \theta_k)$ that describes how the ejection of fragments depends on the orientation of the molecule. This method provides a quantitative check of the axial-recoil approximation. As demonstrated, the axial-recoil approximation does not hold for the $CO_2^{2+} \rightarrow CO^+ + O^+$ channel that we observed at 1×10^{15} W/cm^2. The molecules are likely to undergo significant realignment during the ionization and fragmentation process. Although in these strong-field experiments we cannot point out exactly when the realignment happens, the idea that we proposed would be very useful for experiments using a weak-field probe (say, x-ray) or short pulses, since the re-alignment effect of the probe before ionization will be negligible. In that case, the result will be purely the angle dependence of the light-induced dynamical (ionization, fragmentation, etc.) processes. For CO_2, however, short pulses (<20 fs) can excite vibrations in the electronic ground state of the neutral via far-off-resonance two-photon Raman scattering[236].

We also introduce another approach that requires less fitting for measurements with lower statistics. This approach does not provide the information at the single-molecule level as the previous one but still gives us valuable insights about the dissociation process by comparing the distributions of the molecular axis and the fragment ions. We use this approach to analyze the dissociation of N_2 in the UV field. The distribution of N^+ ions from the double ionization channel ($N_2^{2+} \rightarrow N^+ + N^+$) reflects fairly well the molecular axis distribution, although there is still some realignment in the field (possibly because our UV probe pulse is fairly long). The single ionization channel ($N_2^+ \rightarrow N^+ + N$), on the other hand, does not reflect the molecular axis distribution and always peaks along the polarization axis. The single ionization channel shows a series of rings that are not observed in strong-field ionization. These rings have different angle-dependent fragmentation rates. The origin of these rings still needs further investigation.

These momenta analyses do not require a charged partner and can be applied to dissociative ionization of singly-charged ions. An extension of this method to pulses of different ellipticity can give more insights to understand processes triggered by re-collision[20,129,158].

This information usually cannot be obtained by other means. In our axially symmetric measurements, only the polar angle dependence can be retrieved while the azimuthal angle is averaged. In order to complete the MF ion angular distributions, 3D momentum spectra without axial symmetry of the molecular axis distribution (by using elliptically polarized pump pulses, for example) are required. Such information can be measured directly by using the Tpx3Cam due to the 1.56 ns time resolution of the detector (in combination with a fast phosphor screen and a uniform field spectrometer), or it can be reconstructed using computed tomography[237–239].

Chapter 6

Alignment-dependent photoelectron angular distributions

In this chapter, we probe the time-dependent ionization dynamics of impulsively-excited rotational wave packets of N_2, CO_2, and C_2H_4 using broadband ultraviolet pulses centered at 262 nm. Photoelectron momentum distributions recorded by velocity map imaging show a strong dependence on alignment, on multiphoton order, and on the electronic and vibrational states of the cation. We show that substantial information about the molecular-frame photoelectron angular distribution can be obtained from the high-order laboratory-frame asymmetry parameters without any prior knowledge of the photoionization process. We also compare few-photon ionization with one-photon ionization and strong-field ionization. An edited version of the discussion in this chapter has been submitted to the Physical Review A journal.

6.1 Introduction

Photoelectron spectroscopy has long been an important method to study atomic and molecular structure and dynamics. With advances in ultrafast light sources in a wide range of wavelengths, time-resolved photoelectron energy and angular momentum measurements have become an essential tool for probing chemical transformations in real-time[26,27,209,240–246]. Photoelectron-photoion coincidence measurements and molecular alignment techniques have also enabled these measurements to be made in the molecular frame, which provides access to the symmetries of electronic states involved[22,247–254]. Following a theoretical framework built for single-photon ionization[156,255–259], Marceau *et al.* have shown that "complete" measurements—wherein the phases and magnitudes of all the relevant photoionization matrix elements are determined—of single-photon ionization of linear molecules is possible with the use of impulsively-excited rotational wave packets[140]. The development of such techniques for larger classes of molecules and photoionization processes will enhance the power of photoelectron spectroscopy as a tool for a detailed understanding of molecular dynamics.

In this work, we report the time-dependent few-photon ionization of impulsively-excited rotational wave packets of molecules (N_2, CO_2, C_2H_4) by broadband ultraviolet (UV) pulses ($\approx$ 262 nm). Without a theoretical framework in the few-photon ionization regime akin to the one used by Marceau *et al.*[140] for single-photon ionization, extracting all the ionization dynamical parameters is beyond the scope of this work. However, we show that it is possible to independently determine the time-dependent molecular axis distributions and separate their averaging effects from the lab-frame photoelectron angular distribution (LFPAD) even without a detailed understanding of the ionization process. This allows us to simultaneously retrieve angle-dependent ionization rates and partial molecular-orientation-dependent photoionization differential cross sections that are closely related to molecular-frame photoelectron angular distributions (MFPADs). We also found that few-photon ionization shares many interesting similarities with one-photon and strong-field ionization (SFI). We hope our results will motivate more theoretical work on few-photon ionization to complete our picture of ionization processes.

6.2 Methodology

Experimentally, we use the fundamental pulse (785 nm, 150 fs) to align the molecules and the third harmonic (≈ 262 nm, ≈190 fs) generated via double- and sum-frequency mixing stages in β-BBO crystals (see Sec. 3.2) to ionize them. We measure the photoelectron momentum distributions with our VMI spectrometer and record these images with the Baser 504k camera (Sec. 3.8.2). The normalization of the recorded data was discussed in Sec. 3.7. From this data, we would like to determine the alignment-resolved LFPAD (AR-LFPAD), which is the photoionization differential cross section (DCS) that depends on both the photoelectron energy and the orientation of the molecule in the laser field. Our approach is similar to the one used for photoion momentum distributions in chapter 5, but with a different interpretation of physical quantities.

The AR-LFPAD is denoted by $d\sigma/d\theta d\theta_k dk$, where σ is the photoionization cross section, k is the magnitude of the electron momentum, θ_k is the polar angle between the laser polarization axis and the electron momentum, and θ is the polar angle between the laser polarization axis and the molecular axis (see Fig. 6.1). Note that the axial symmetry of the measurement about the laser polarization axis precludes the determination of the dependence on azimuthal angles. The AR-LFPAD can be expressed as a linear combination in the basis of the product of two Legendre polynomials $P_J(\cos\theta)P_L(\cos\theta_k)$ for the angular dependence,

$$\frac{d\sigma}{d\theta d\theta_k dk} = \sum_{JL} A_{JL}(k) P_J(\cos\theta) P_L(\cos\theta_k). \tag{6.1}$$

The AR-LFPAD can be normalized to the alignment-resolved photoelectron spectrum (AR-PES)[260] $R(k,\theta)$ to highlight the distribution of electrons at each molecular orientation. We call it the yield-corrected AR-LFPAD (YCAR-LFPAD) and write it as

$$S(\theta, k, \theta_k) = \frac{1}{R(k,\theta)} \frac{d\sigma}{d\theta d\theta_k dk}, \tag{6.2}$$

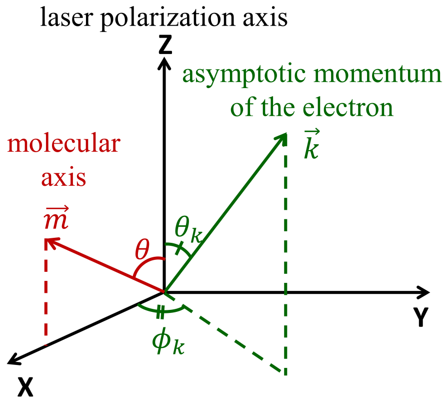

Figure 6.1: *All angles are defined in the LF where Z is the laser polarization axis, and X is the laser propagation direction. The molecular axis is described by the polar angle θ and the azimuthal angle ϕ. The asymptotic photoelectron momentum is described by the polar angle θ_k, the azimuthal angle ϕ_k and the magnitude k of the momentum. The angle ϕ is not physically relevant, and the relevant angle $\phi_k - \phi$ is lost because of the axial symmetry of the measurement, so the molecular axis is shown here at an arbitrarily chosen angle $\phi = 0°$. We would like to determine the AR-LFPAD, $d\sigma/d\theta d\theta_k dk$, which is the photoionization DCS that depends on both the photoelectron energy and the orientation of the molecule in the laser field. This AR-LFPAD is closely related to the MFPAD, as discussed in the text.*

where $R(k,\theta)$ can be obtained either by integrating the AR-LFPAD[260] in Eq. (6.1) over θ_k,

$$R(k,\theta) = \frac{d\sigma}{d\theta dk} = \int \frac{d\sigma}{d\theta d\theta_k dk} \sin\theta_k d\theta_k, \tag{6.3}$$

or by applying linear regression fitting to the delay-dependent yield of the corresponding channel[30,31,97,139,141,142] as shown in chapter 4. We check both methods for consistency. For each particular energy (determined by the momentum k), $R(k,\theta)$ can also be interpreted as the likelihood of ionization as a function of θ.

As discussed in the literature[140,156,255,257,258], in the LF, the time-resolved LFPAD, $d\sigma(t)/d\theta_k dk$, is a sum of the AR-LFPAD, $d\sigma/d\theta d\theta_k dk$, weighted by the delay-dependent molecular axis distribution, $\rho(\theta,t)$, illustrating the averaging effect on the observed LFPADs,

$$\frac{d\sigma(t)}{d\theta_k dk} = 2\pi \int \rho(\theta,t) \frac{d\sigma}{d\theta d\theta_k dk} \sin\theta d\theta. \tag{6.4}$$

or equivalently,

$$\frac{d\sigma(t)}{d\theta_k dk} = 2\pi \sum_L \left[\sum_J A_{JL}(k) \langle P_J(\cos\theta) \rangle (t) \right] P_L(\cos\theta_k), \tag{6.5}$$

where the AR-LFPAD was replaced by the expansion in Eq. (6.1). A more detailed discussion of these equations is provided in Appendix A.2 (see Eq. (A.11) and Eq. (A.13)).

The three-dimensional (3D) LFPAD at each delay, $d\sigma(t)/d\theta_k dk$, can be reconstructed from the VMI data by applying an Abel inversion using the pBasex method[225] due to the axial symmetry of the momentum distribution,

$$\frac{d\sigma(t)}{d\theta_k dk} = 2\pi \sum_L C_L(k,t) P_L(\cos\theta_k), \tag{6.6}$$

where

$$C_L(k,t) = \sum_{k_0} C_{k_0 L}(t) e^{-\frac{(k-k_0)^2}{2\sigma_b^2}}, \tag{6.7}$$

k_0 and σ_b are the centers and the width of the radial Gaussian functions, and $C_{k_0 L}(t)$ is a set of delay-dependent coefficients obtained via pBasex.

By comparing Eq. (6.5) and Eq. (6.6), we have the relation between the delay-dependent coefficients, $C_L(k,t)$, and the coefficients $A_{JL}(k)$ needed to determine the AR-LFPAD as

$$C_L(k,t) = \sum_J A_{JL}(k) \left\langle P_J(\cos\theta) \right\rangle (t). \tag{6.8}$$

This equation can be solved using ORRCS[30,31,139], as discussed in chapter 2. A brief discussion of the ORRCS method follows.

We calculate $\left\langle P_J(\cos\theta) \right\rangle (t)$ by solving the time-dependent Schrödinger equation (TDSE) for rigid rotors. By fitting the calculated $\left\langle P_J(\cos\theta) \right\rangle (t)$ to the experimentally-obtained delay-dependent coefficients $C_L(k,t)$, the coefficients $A_{JL}(k)$ can be determined. The fit is done over a grid of different pump laser intensities, pulse durations, and gas rotational temperatures near the measured values to ensure the accuracy in these calibrations. The main result is that we can simultaneously determine all three quantities: the AR-LFPAD $S(\theta, k, \theta_k)$, the AR-PES $R(k, \theta)$ and the rotational wave packet $\rho(\theta, t)$. $S(\theta, k, \theta_k)$ and $R(k, \theta)$ are determined through $A_{JL}(k)$ by using Eq. (6.1) and Eq. (6.3), while $\rho(\theta, t)$ is determined by the best-fit estimations of the pump-laser fluence and the rotational temperature of the gas and by the TDSE calculation of the rotational wave packet using these parameters. The averaging over the axis-distribution moments is incoherent[140,156,255,257,258], so polar plots of the angle-dependent ionization rates throughout this paper are physical. The experimental uncertainty is propagated through each step of the data analysis assuming no covariance between quantities (details can be found in Appendix A.1).

The asymmetry parameters[145] β_L can be written in terms of the C_L coefficients as

$$\beta_L(k, t) = \frac{C_L(k, t)}{C_0(k, t)} \tag{6.9}$$

and the angle-integrated cross section is $\sigma(k, t) = 8\pi^2 C_0(k, t)$. In practice, we need to integrate over a finite range (radial width) of the radial momentum k that each channel spans.

In general, the fully-resolved LFPAD (FR-LFPAD) can be written as

$$\frac{d\sigma}{dk\, d\Omega\, d\Omega_k} = \left| \left\langle \psi^e \psi^{\text{ion}} \middle| \hat{\mathbf{O}} \middle| \psi^{\text{i}} \right\rangle \right|^2, \tag{6.10}$$

where ψ^{i} is the initial state of the molecule, ψ^e is the final state of the photoelectron, ψ^{ion} is the state of the corresponding ion, and $\hat{\mathbf{O}}$ is the light-induced coupling between the initial and the final state of the wave function (for example, in one-photon ionization, it is the dipole). $d\Omega$ expresses the dependence on θ and ϕ, and $d\Omega_k$ expresses the dependence on θ_k and ϕ_k. This FR-LFPAD is equivalent to the MFPAD (or the MF interferogram). Both contain the same information since no averaging has been done, and rotation does not affect the shape of the distribution. They can be transformed into one another by a rotation connecting the two frames.

To fully characterize the photoionization dynamics and fully describe the MFPAD (i.e., perform a ‘complete’ experiment), one needs to determine the magnitudes and phases of all the involved matrix elements[261]. It has been theoretically[257] and experimentally[140] demonstrated that, in the case of one-photon ionization by linearly polarized light of a linear molecule, a measurement with cylindrical symmetry provides enough information to do so, but there is no framework for other cases. Hence, we focus on obtaining best-fit estimates for $A_{JL}(k)$, which determine the AR-LFPAD. These coefficients carry partial but important information about the photoionization process.

We would like to point out two limitations in the information contained in the $A_{JL}(k)$. The first is that the AR-LFPAD does not contain information about the ϕ-dependence, where ϕ is the azimuthal angle about the laser polarization axis. This information is lost because of the cylindrical symmetry of the LF measurement (see Appendix A.2, Eq. (A.11) and Eq. (A.13)). The second is that, since we do not identify the relevant matrix elements, the AR-LFPAD is truncated based on the convergence of the fit in Eq. (6.8) (as discussed in chapter 4) rather than on angular momentum constraints. Using this procedure, we are still able to reconstruct the MF interferograms (or MFPADs) as mentioned by Marceau *et al.*[140] with an average about the laser polarization axis without any prior knowledge of the photoionization process.

6.3 Results and discussions

6.3.1 Nitrogen

In this experiment, cold nitrogen molecules (N_2 at a rotational temperature $\approx$ 6 K), from the supersonic expansion of a gas mixture of 2% N_2 in He, are aligned by a pump pulse (150 fs, 34 TW/cm^2, 800 nm) and then ionized by a third harmonic pulse at different delays. Fig. 6.2 shows the raw photoelectron VMI spectra for isotropic, aligned, and anti-aligned distributions (a-c), and the energy-calibrated spectrum (d). By comparing with spectroscopic data[262], we can identify photoelectrons ionized into several ionic states with different numbers of photons absorbed as shown in (d). A strong dependence of the PADs on the alignment, on electronic and vibrational states of the cation, and on photon-numbers can be seen already in raw VMI images (a-c).

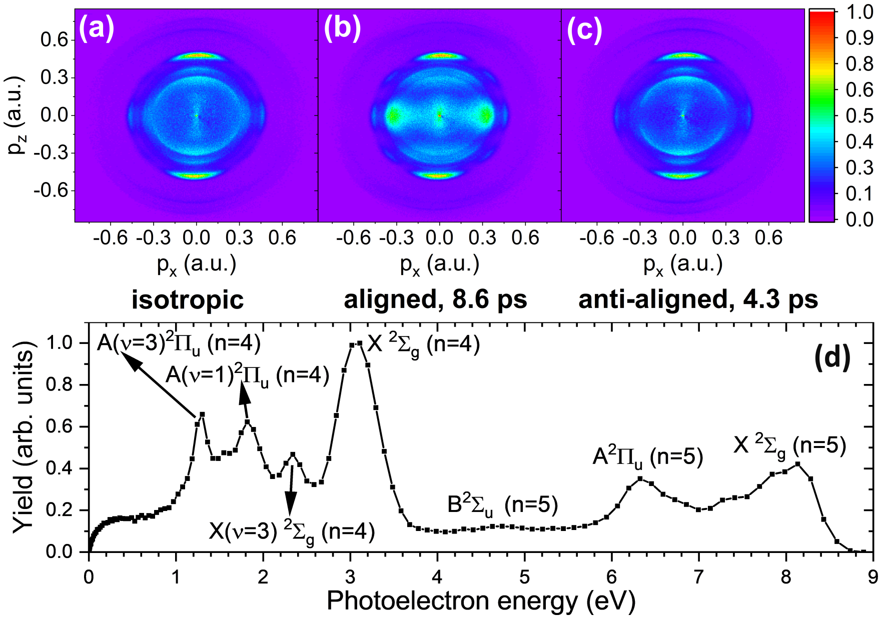

Figure 6.2: *VMI images of the photoelectron momentum from* N_2 *at the isotropic (a), aligned (b), and anti-aligned (c) distributions. The laser polarization is along the* p_z *direction. The linear color scale expresses the yield of the electrons in arbitrary units; the same scale is used in all images. Using the pBasex algorithm*[225]*, the VMI image of the isotropic distribution is converted to energy and angular distributions as shown in (d), with ionic states and photon numbers (n) identified using spectroscopic data*[262]*.*

As discussed in Sec. 6.2, we can reconstruct the delay-dependent 3D LFPADs by applying the pBasex inversion algorithm[225] to the VMI image at each delay. These distributions are described, through Eq. (6.6), by a set of delay-dependent coefficients, $C_L(k, t)$. The modulations of the LFPADs of different channels as the wave packet evolves are depicted more clearly in delay-momentum maps of these coefficients in Fig. 6.3(a).

By applying regression analysis[31] to the delay-dependent yield, we retrieve the relative AR-PES (see Eq. (6.3)) as shown in Fig. 6.3(b). Each vertical line is the angle-dependent ionization rate at a specific photoelectron momentum (k), normalized to ionization from an isotropic distribution. The energy-integrated angle-dependent ionization rate has a peanut shape and peaks along the laser polarization axis ($\theta = 0°$). Petretti *et al.* have theoretically

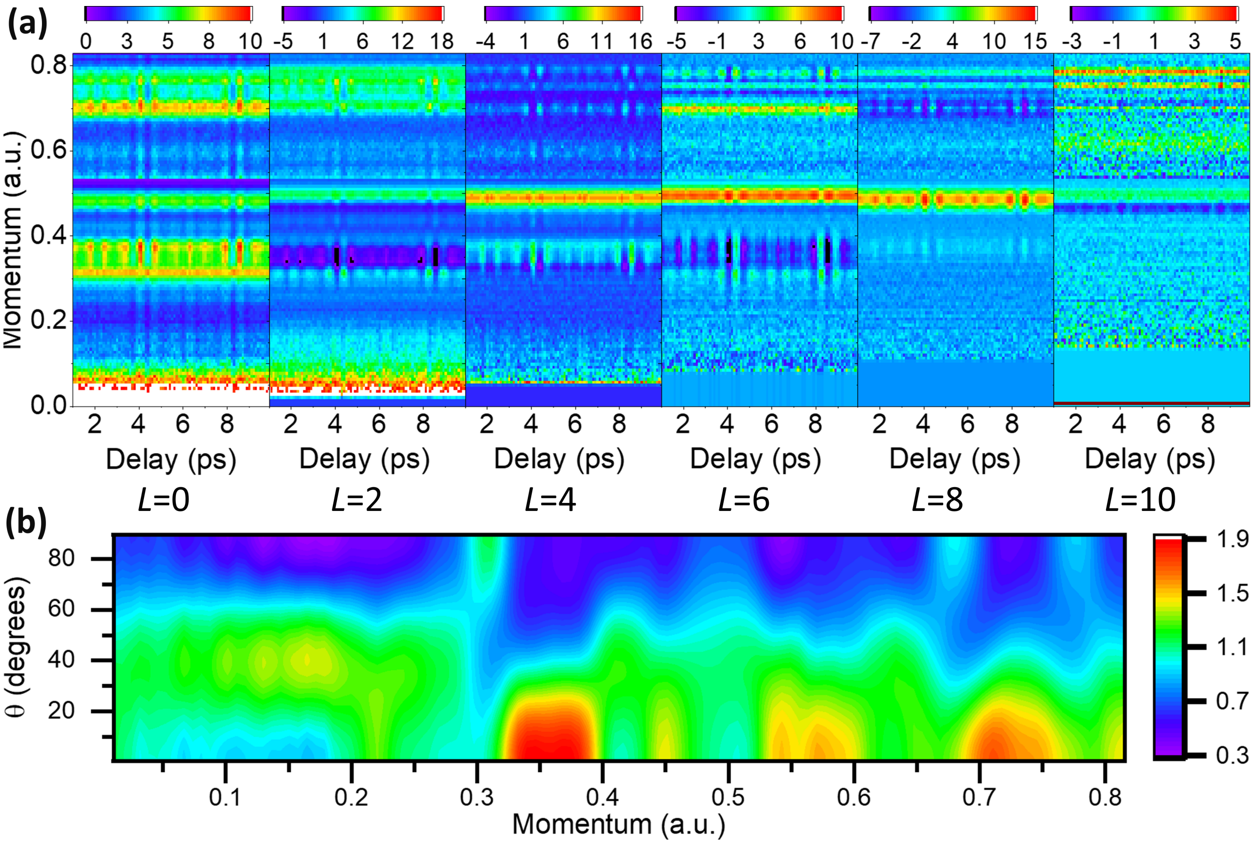

Figure 6.3: *(a) Delay-momentum maps of the pBasex coefficients. These coefficients describe the modulation of the time-resolved LFPAD as a function of the electron asymptotic momentum (k) and the pump-probe delay (t) through Eq. (6.6). Signals for $k > 0.53$ a.u. were multiplied by 10 for clarity. We implemented the Nyquist theorem by dropping the low k, high L basis functions, i.e., data near the center of the image (low k) do not have enough resolution to resolve complex angular structure (high L). (b) The AR-PES (see Eq. (6.3)). Each 1-D vertical slice is the angle-dependent ionization rate at a specific photoelectron momentum (k), which describes how the ionization yield at different orientations of the molecular axis (θ) compares to the ionization yield from an isotropic distribution.*

predicted the wavelength- and alignment-dependent photoionization of N_2[263] by weighting the angle-dependent contributions of ionization from different orbitals. At 266 nm, the ionization rate of HOMO−1 with π_u symmetry peaks perpendicular to the molecular axis and contributes significantly to the total ionization rate. The discrepancy with our results suggests further considerations are needed, such as the role of the intermediate and excited states, or a different weighting (of the angle-integrated cross-section) between channels.

The 4-photon ionization to the ground state, $X^2\Sigma_g$, of the ion is presented in Fig. 6.4.

Panel (a) shows the average delay-dependent coefficients, $C_L(k,t)$, and their corresponding fits. We observed strong modulation of these coefficients as a function of delay, and obtained good fits using linear regression through Eq. (6.8). With these fits, we retrieved the coefficients $A_{JL}(k)$ and thus determined the angle-dependent ionization rate (Fig. 6.4(b)) and the YCAR-LFPAD (Fig. 6.4(c)). Tables of the $A_{JL}(k)$ coefficients for all channels presented in the paper are provided in Appendix A.3.

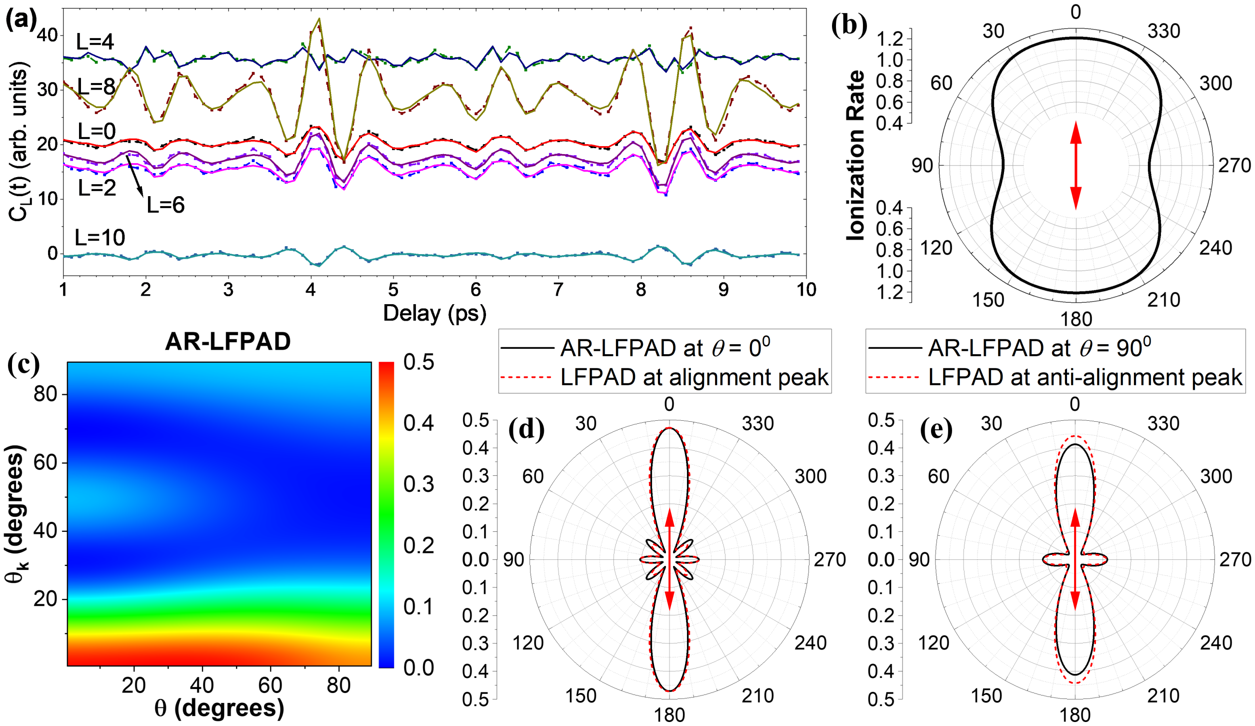

Figure 6.4: *Results for ionization of* $\mathrm{N_2}$ *into the* $\mathrm{X^2\Sigma_g}(n=4)$ *ionic state: (a) The delay-dependent pBasex coefficients,* $C_L(t)$*, (dashed with square symbol) and their corresponding fits (solid) as described in Eq. (6.8). From these fits, we can retrieve the angle-dependent ionization rate (b) and the YCAR-LFPAD (c). The angle-dependent ionization rate looks similar to the previous result from SFI*[29]*. We compare the AR-LFPAD slice at* $\theta = 0°$ *with the LFPAD at the alignment peak in (d), and the AR-LFPAD slice at* $\theta = 90°$ *with the LFPAD at the anti-alignment peak in (e). The angle in these polar plots (d-e) is* θ_k*. Their similarities indicate these measurements in the LF are a good representation of the MF. The laser polarization axis is indicated by the red arrow.*

The angle-dependent ionization rate in this case looks similar to the previous result from SFI by Pavičić *et al.*[29], and hence, still reflects the σ_g symmetry of the highest occupied molecular orbitals (HOMO). In Fig. 6.4(c), the YCAR-LFPAD $S(\theta,k,\theta_k)$ shows a transition from a three-lobe structure at $\theta \approx 0°$ to a two-lobe structure at $\theta_k \approx 90°$. When the molecule is parallel to the laser polarization direction ($\theta \approx 0°$), the PAD shows three peaks at $\theta_k \approx 0°$ (along the laser polarization axis), $\theta_k \approx 90°$ (perpendicular to the laser polarization axis) and $\theta_k \approx 50°$. When the molecule is perpendicular to the laser polarization direction ($\theta \approx 90°$), the PAD still shows the peaks at $\theta_k \approx 0°$ and $\theta_k \approx 90°$, but the peak at $\theta_k \approx 50°$ that is seen near $\theta = 0°$ has faded away.

Fig. 6.4 also shows the comparison between the LFPAD at peak alignment (Fig. 6.4(d), dashed line) and anti-alignment (Fig. 6.4(e), dashed line) with the YCAR-LFPAD, $S(\theta, k, \theta_k)$, at $\theta = 0°$ (Fig. 6.4(d), solid line) and $\theta = 90°$ (Fig. 6.4(e), solid line). The similarity of the AR-LFPAD at $\theta = 0°$ and the LFPAD at peak alignment suggests that, at this degree of alignment ($\langle \cos^2 \theta \rangle_{\mathrm{max}} \approx 0.78$), the measurement of LFPADs gets very close to the MFPADs. This can serve as a useful test case to benchmark different methods of constructing the MFPADs. Direct measurements of 3D LFPADs without the axial symmetry using tomographic imaging techniques[237–239] would then be a useful comparison though a simultaneous rotation of the polarization axes of two different wavelengths can be a challenge.

Similar results for 4-photon ionization into three vibrational levels ($\nu = 1 - 3$) of the first excited state of the ion, $\mathrm{A}^2\Pi_\mathrm{u}$, are presented in Fig. 6.5. In comparison with ionization into the ground state, $\mathrm{X}^2\Sigma_\mathrm{g}(n = 4)$, the angle-dependent ionization rates show a significant contribution from the perpendicular orientation that was not observed in Fig. 6.4(b). The ionization rates become more isotropic for higher vibrational levels.

In general, the diagonal trend in the YCAR-LFPAD shows that electrons from ionization to the first excited state of the ion, $\mathrm{A}^2\Pi_\mathrm{u}$, are distributed mainly perpendicular to the molecular axis ($\theta_k \approx 90° - \theta$), which may be connected to the π_u symmetry of the HOMO-1 orbital. This signature was not reflected clearly in the ionization rates. This strong dependence on the molecular orientation is completely different from the distribution of electrons ionized into the ground state, $\mathrm{X}^2\Sigma_\mathrm{g}(n = 4)$.

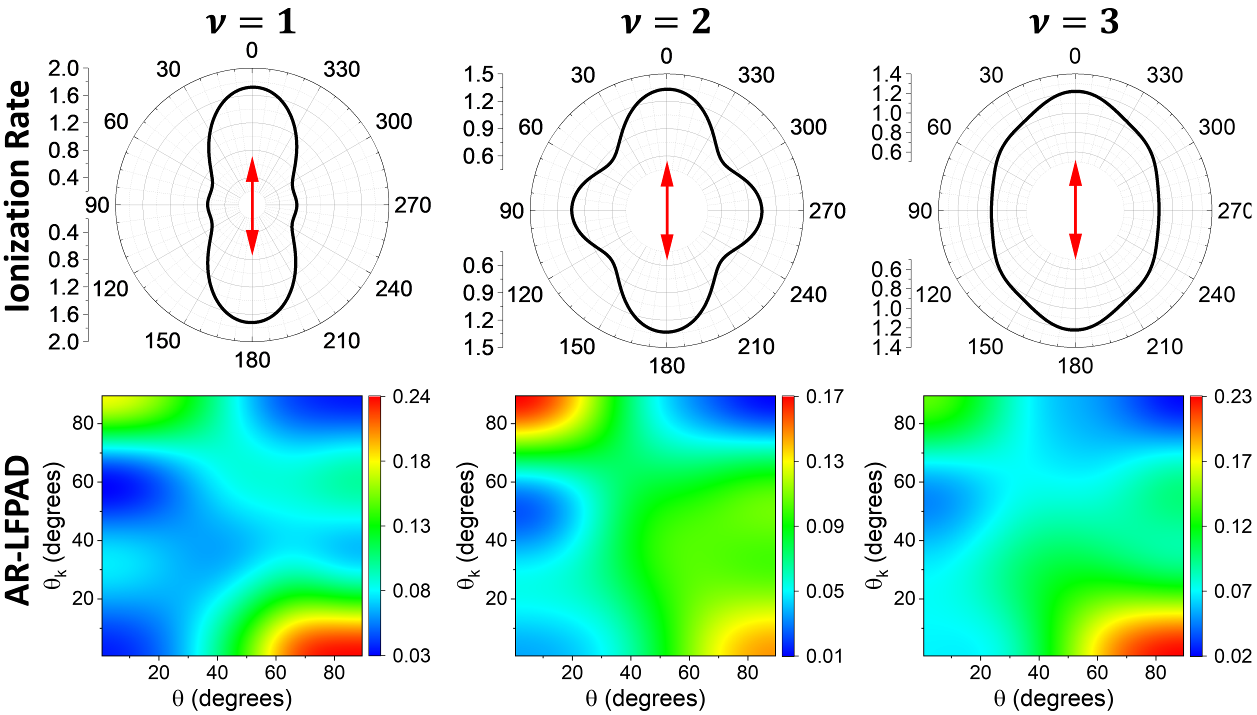

Figure 6.5: *Results for ionization of* N_2 *into three different vibrational levels of the first excited state* $A^2\Pi_u(n = 4)$ *of the cation: (Top) The angle-dependent ionization rate. (Bottom) The YCAR-LFPAD* $S(\theta, k, \theta_k)$. *Different vibrational levels are* $\nu = 1 - 3$ *from left to right, respectively.*

6.3.2 Carbon dioxide

In the case of carbon dioxide (CO_2), cold molecules (≈ 4 K), from the supersonic expansion of a gas mixture of 0.5% CO_2 in He, are aligned with a pump pulse (about 150 fs, 13 TW/cm^2, 800 nm) and then ionized by a third harmonic pulse.

We observed a dominant channel at electron energy ≈ 0.4 eV, corresponding to three-photon ionization into the ground state, $X^2\Pi_g$, of the cation. In Fig. 6.6, raw VMI images in panels (a) and (b) already show distinguishable features in directions parallel and perpendicular to the laser polarization axis. The delay-dependent coefficients, $C_L(k, t)$, and their corresponding fits are shown in panel (d). We obtained strong modulations and good fits up to $L = 6$ while higher-order coefficients are much smaller.

Here, the angle-dependent ionization rate in panel (c) still has a butterfly shape, similar to the previous results from SFI[31,131], although the dip at 0° is less pronounced. The angle-resolved YCAR-LFPAD, $S(\theta, k, \theta_k)$, in panel (e) is also fairly symmetric about $\theta \approx 45°$.

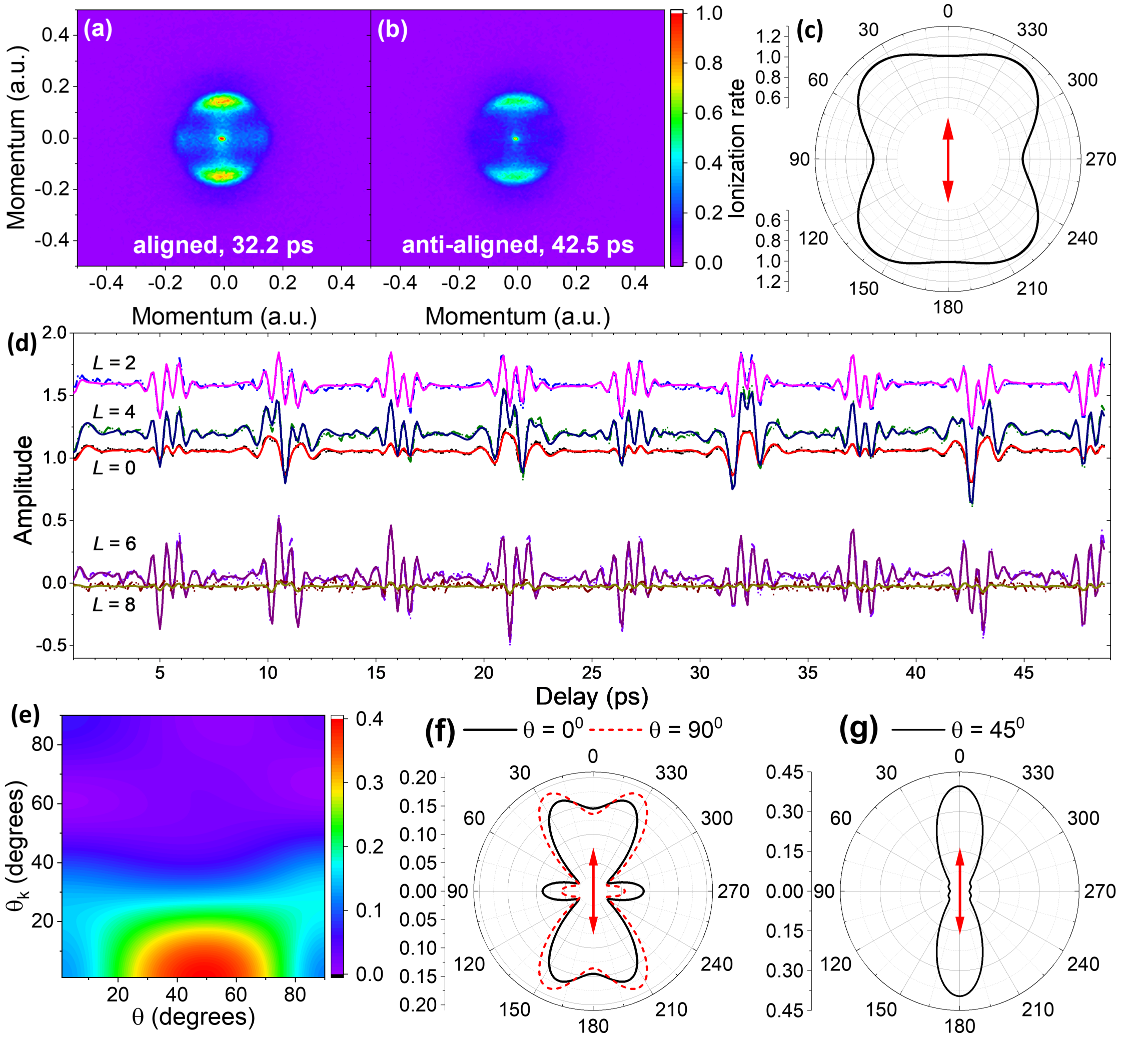

Figure 6.6: *Three-photon ionization of* CO_2 *into the ground state* $X^2\Pi_g$ *of the ion. (a,b) VMI electron images at the alignment (a) and anti-alignment (b) peaks. (c) The angle-dependent ionization rate. (d) The delay-dependent coefficients* $C_L(k,t)$ *(dashed) and their corresponding fits (solid) for the channel. k is averaged over a range of 0.12 to 0.19 a.u. (e) The YCAR-LFPAD. (f,g) Slices of the YCAR-LFPAD at* $\theta = 0°$ *and* $90°$ *(f), and at* $45°$ *(g). The laser polarization axis is indicated by the red arrow.*

Three slices of the YCAR-LFPAD at $\theta = 0°$, $45°$ and $90°$ are presented in panel (f-h). Slices at $\theta = 0°$ and $90°$ have a butterfly shape together with a peak perpendicular to the laser polarization axis ($\theta_k = 90°$), while the slice at $\theta = 45°$ has a peanut shape with no feature at ($\theta_k = 90°$). All these observed features suggest that the PADs still reflect the π-symmetry of the HOMO.

6.3.3 Ethylene

The analysis that we presented is general and can be extended for different types of molecule and laser polarization. For asymmetric top molecules, both Euler angles, θ and χ, are needed to describe the relative orientation between the molecule and a linearly polarized laser field[30] as discussed in sec. 2.1.2. In the MF, these Euler angles, θ and χ, are the polar and azimuthal angles describing the laser polarization vector. In practice, however, the YCAR-LFPAD reconstruction requires a much larger set of expansion coefficients $A_{JKL}(k)$ to be determined and a more sophisticated interpretation[264]. In this section, we limit our discussion to the AR-PES (or the molecular-frame angle- and energy-dependent ionization rate), $R(k, \theta, \chi)$. Unlike in the work by Makhija *et al.*[30], where the ions were measured to deduce $R(k, \theta, \chi)$ for SFI, in few-photon ionization and by using the VMI technique, we can separately determine $R(k, \theta, \chi)$ for multiple channels with electrons corresponding to different states of the cations.

A measurement was made on ethylene (C_2H_4) where rotationally cold molecules ($\approx$ 4 K), from the supersonic expansion of a gas mixture of 0.5% target gas in He, are aligned with a pump pulse (about 200 fs, 4 TW/cm^2, 800 nm) and then ionized by a third harmonic pulse. The photoelectron spectrum shows two distinct channels, with the electron energies $\approx$ 3.7 eV and $\approx$ 1.4 eV, corresponding to three-photon ionization into the ground state, $\tilde{\mathrm{X}}^2\mathrm{B}_{3\mathrm{u}}$, and the first excited state, $\tilde{\mathrm{A}}^2\mathrm{B}_{3\mathrm{g}}$, of the ion as shown in panels (a) and (b) of Fig. 6.7. By fitting to the delay-dependent yields of these two channels using linear regression (c), we can retrieve the full molecular-frame angle-dependent ionization rates, $R(\theta, \chi)$, that depend on both Euler angles for each channel[30,31,139] as shown in panels (d) and (e).

The results share many similarities with previous measurements in the SFI regime[30]. The ionization probability into the ground state, $\tilde{\mathrm{X}}^2\mathrm{B}_{3\mathrm{u}}$, has a maximum at $\theta = 90°$ and $\chi = 90°$. This is similar to the angle-dependent probability of the non-dissociative strong-field ionization obtained by measuring the $C_2H_4^+$ ion, which was assigned to the removal of an electron from the HOMO[30]. On the other hand, the ionization into the first excited state, $\tilde{\mathrm{A}}^2\mathrm{B}_{3\mathrm{g}}$, prefers molecules aligned near $\theta = 45°$ and $\chi = 0°$. This is similar to the

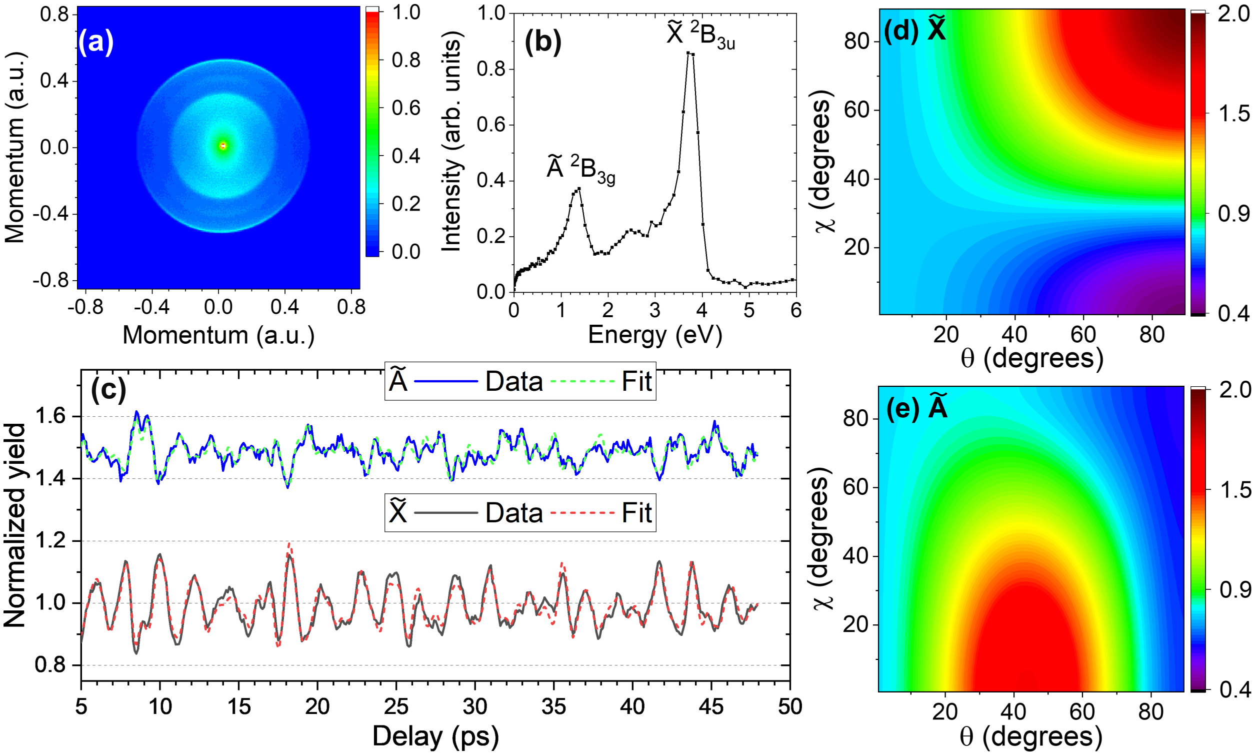

Figure 6.7: *Results on three-photon ionization of* C_2H_4 *into the ground state* $\tilde{X}^2B_{3u}$ *and the first excited state* $\tilde{A}^2B_{3g}$ *of the ion. The top panel shows an example of a VMI electron image (a) and the calibrated energy with ionic states identified by using spectroscopic data*[265] *(b). (c) The delay-dependent electron yields of the two channels and their corresponding fits. The first excited state,* $\tilde{A}^2B_{3g}$*, was shifted up by 0.5 for clarity. The bottom pannel shows the angle-dependent ionization rates,* $R(\theta, \chi)$*, of the ground state (d) and the excited state (e).*

angle-dependent probability of the dissociative ionization in the strong field obtained by measuring the $C_2H_3^+$ and $C_2H_2^+$ ions, which was previously assigned to removing a HOMO-1 electron[30].

6.4 Conclusions

We have investigated the time-dependent ionization dynamics of impulsively-excited rotational wave packets of molecules using broadband UV pulses for ionization and fundamental 785 nm pulses for alignment. The PADs show a strong dependence on alignment, on multiphoton order, and on electronic and vibrational state, indicating that these PADs are sensitive to molecular structure and dynamics.

We have shown that, without prior knowledge of the photoionization process, partial but substantial information about the MFPAD (with an average about the laser polarization axis) can still be retrieved from the highly anisotropic laboratory-frame data using a fitting algorithm. This partial MFPAD, or a large set of extracted coefficients describing it, can be compared with theory to better understand multiphoton ionization of molecules. The determination of a full MFPAD, together with complex matrix elements describing the electronic coherences and ionization dynamics, requires further developments of a proper ionization model and a complex theoretical framework, especially for different types of molecules and polarization geometries. A better understanding of the MFPAD is necessary since time-resolved MFPAD is a promising probe of molecular dynamical processes.

Few-photon ionization is in the middle regime between the better-understood one-photon ionization and SFI. In many cases, we found similarities between the angle-dependent ionization rates by a few photons and by a strong field. In SFI, the widely used MO-ADK model connects the angle-dependent ionization rate to the shape and the symmetry of the molecular orbitals[32]; however, such a connection has not been established in the few-photon ionization regime. In a one-photon process, the transition is either parallel or perpendicular, and the angle dependence of the ionization rate can only be either $\cos^2\theta$ or $\sin^2\theta$ since the ionization yield only depends on the second-order moment of the molecular axis distribution. n-photon ionization allows a resolution up to the $2n^{\text{th}}$-order moment[156], which can reveal more details if one can decode the relationship between the angle-dependent ionization rate and the molecular states. On the other hand, the PADs in few-photon ionization are very sensitive to molecular structure and dynamics, which is similar to one-photon ionization, while electrons in a strong field are typically distributed along the laser polarization and are less sensitive to the molecular dynamics. More investigations in the few-photon ionization regime are needed to complete our picture of ionization processes and to gain the advantages of the knowledge we obtained from the other two regimes.

Chapter 7

Concluding remarks

In this dissertation, we have systematically investigated and developed the time-domain method for retrieving the angle dependence of multiple processes. By performing different statistical analyses and independent experiments, we tested the stability and consistency of the ORRCS retrieval algorithm. We realized that the convergence of the retrieved angle dependence signal serves as a good indicator for determining the appropriate fitting model. We also noted that the retrieval is sensitive to both the statistical and the systematic errors introduced in the experiment and theory. We retrieved the angle-dependent strong-field ionization of CO_2 (a linear molecule) and SO_2 (an asymmetric top molecule), addressing the discrepancies between previous experiments and theories on CO_2 and giving more experimental evidence on asymmetric top molecules with SO_2.

We expanded the time-domain approach to momentum measurements and applied this new analysis to the dissociation and photoionization of molecules. In the dissociation of molecules, we showed how the dissociation depends on the initial orientation of the molecule and used this information to test the axial-recoil approximation. The dissociative double ionization of CO_2 by a strong 800 nm laser pulse does not follow axial recoil break up while the dissociative double ionization of N_2 by a 262 nm pulse shows a clear imprint of the initial molecular distributions in the final angular distributions of the fragment ions. We will perform further experiments using high-resolution Fourier transform and coincident imaging techniques to understand the origin of the low energy N^+ and to complete our angle- and channel-resolved experiment. In photoionization of molecules, we retrieved the orientation-resolved photoelectron angular distributions of N_2, CO_2, and C_2H_4 in the few-photon ionization regime. In this regime, the angle-dependent ionization rates show similarities with strong-field ionization, while angular distributions of the photoelectrons still reflect the symmetry of the molecular orbitals similar to single-photon ionization.

During the exploration of the time-domain approach, we also discovered that, unlike the majority of linear molecules, the delay-dependent yield of O_2^+ in a pump-probe experiment, where the pump non-resonantly aligns the molecules and the probe singly ionizes them, is not periodic (Fig. 7.1). The reason is that oxygen has a triplet ground state, its nuclear rotational angular momentum is coupled to its electronic spin angular momentum, and the spins of the two unpaired electrons are also coupled. Due to these couplings, the alignment pulse excites both rotation and spin dynamics in oxygen molecules. The rotational wave packet is no longer "purely rotational", and the delay-dependent ionization yield is non-periodic. The effect of these couplings has not been measured in previous experiments on impulsively aligned O_2[29,266] since it is only important for a few small values of the total angular momentum ($J \leq 7$)[267]. With our cold molecular beam, almost all the molecules are in the lowest rotational state ($N = 1$, where N is the rotational angular momentum quantum number, and even-N states are forbidden by nuclear spin statistics), and thus a significant signature of these couplings was observed. Our 200 ps long delay scan provides sufficient resolution (≈ 0.167 cm^{-1} or ≈ 20.7 μeV) to resolve spin splitting of the rotational levels in the $X^3\Sigma_g^-$ ground state of the neutral. We have updated our ORRCS analysis to account for this phenomenon. The analysis has been done, and the manuscript is being prepared. Recently, we became aware that Sonoda *et al.* just published a related theoretical analysis on this phenomenon[268]. Another interesting result was also observed for a strong ionizing pump and a weak probe. Our VMI delay scans show a dominant contribution from a single vibrational level ($\nu = 4$ in the $b\ ^4\Sigma_g^-$ state of the O_2^+ cation) for near-zero kinetic energy O^+ fragments. This clear evidence of the residual ionic wave packet in the $b\ ^4\Sigma_g^-$ state provides valuable insights into the laser-induced dissociation of O_2[232,269–271] and strongly supports the three-state model by Xue *et al.*[272]. This also poses a general question: will we observe a similar phenomenon with other molecules, or are we limited by the coincidence of the curve crossings and thresholds in O_2^+? These results on oxygen will be reported in later publications.

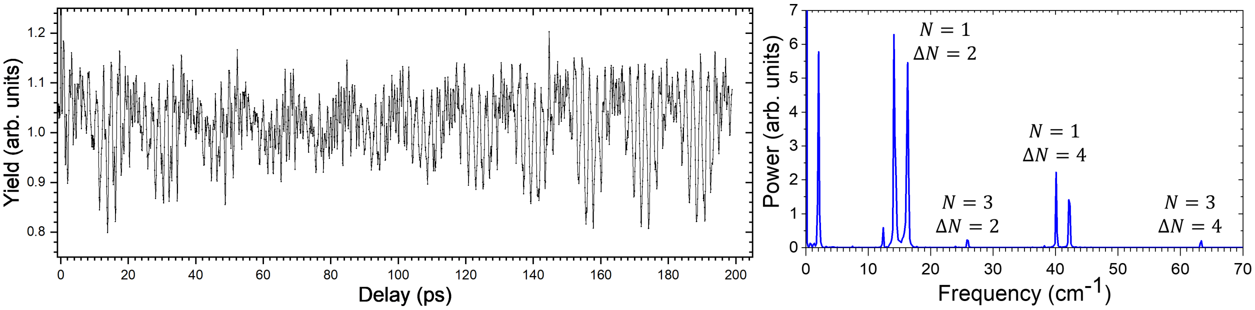

Figure 7.1: *Left: Delay-dependent* O_2^+ *ionization yield. The alignment pulse was 210 fs, 6 TW/cm*^{2}*, and the ionization pulse was 40 fs, 40 TW/cm*^{2}*. Right: Fourier spectrum of the ionization yield. Lines correspond to energy differences between states with a definite phase relation (quantum beats). N indicates the lower energy state.*

The time-domain approach, equipped with cold gas-phase molecules and the VMI spectrometer, is a powerful tool to enable angle- and channel-resolved investigations for a wide range of physical and chemical processes. This capability can be greatly expanded when combined with other techniques such as coincident imaging and high-resolution Fourier spectroscopy, making high-resolution channel-resolved molecular-frame measurements possible. To realize this idea in the setup with a COLTRIMS spectrometer and the incoming high repetition rate laser, we plan to build a continuous, cold jet source using cryogenic cooling and molecular entrainment[273].

We also would like to apply our method to other ultrafast probes. In our laboratory, an apparatus for single-photon ionization of molecules from an HHG-based source was constructed. We expect to finish commissioning and to start a preliminary experiment in summer 2021. Single-photon ionization is a well-understood process; we expect that the detailed information provided by the orientation-resolved photoelectron angular distributions retrieved using this setup can help us understand the dynamics of linear and asymmetric top molecules. On a different note, recently, an investigation on applying ORRCS to extract the body-frame molecular geometry from ultrafast gas-phase diffraction has been reported[274]. The possibility of imaging cationic states by independently performing both diffraction imaging and coincident measurements has also been initially explored[275]. Diffraction imaging provides the molecular structure; however, extracting structural information for many unknown fragments from the averaged diffraction patterns is so far not possible. Coincident ion mass spectrometry can complement this by providing information such as kinetic energy release and branching ratios. The detected fragments and branching ratios form the basis functions for retrieving the structures. If we do an align-ionize measurement of the ion yields, different ionization channels could have different angle dependences, and thus have different delay-dependent yields. In the end, we have branching ratios that change with delay. The align-ionize-diffraction signal will be a linear combination of these delay dependences since they add incoherently and can be separated by linear regression using the delay-dependent ionization yields as the basis functions. In addition, 2D data with a lot more information can be obtained from diffraction patterns of aligned molecules.

We believe that the time-domain approach developed in this work can be helpful in many areas of ultrafast physics and chemistry. With the recent rapid development of high repetition rate ultrafast probes, we expect that many measurements using x-ray free-electron laser and electron beams will have the capability to apply our method and gain valuable insights into molecular structures and dynamics in the near future. This approach to molecular-frame measurements contributes a step toward monitoring and controlling chemical reactions in real time, one of the main goals of ultrafast atomic, molecular, and optical physics.

Bibliography

[1] G. H. C. New, Rep. Prog. Phys. **46**, 877 (1983), URL https://doi.org/10.1088/0034-4885/46/8/001.

[2] P. M. W. French, Rep. Prog. Phys. **58**, 169 (1995), URL https://doi.org/10.1088/0034-4885/58/2/001.

[3] A. M. Weiner, *Ultrafast optics* (John Wiley & Sons, Inc, 2009).

[4] K. Yamane, Z. Zhang, K. Oka, R. Morita, M. Yamashita, and A. Suguro, Opt. Lett. **28**, 2258 (2003), URL https://doi.org/10.1364/OL.28.002258.

[5] A. L. Cavalieri, E. Goulielmakis, B. Horvath, W. Helml, M. Schultze, M. Fieß, V. Pervak, L. Veisz, V. S. Yakovlev, M. Uiberacker, et al., New J. Phys. **9**, 242 (2007), URL https://doi.org/10.1088/1367-2630/9/7/242.

[6] S. Rausch, T. Binhammer, A. Harth, J. Kim, R. Ell, F. X. Kärtner, and U. Morgner, Opt. Express **16**, 9739 (2008), URL https://doi.org/10.1364/OE.16.009739.

[7] J. Li, J. Lu, A. Chew, S. Han, J. Li, Y. Wu, H. Wang, S. Ghimire, and Z. Chang, Nat. Commun. **11**, 2748 (2020), URL https://doi.org/10.1038/s41467-020-16480-6.

[8] M. Y. Ivanov, R. Kienberger, A. Scrinzi, and D. M. Villeneuve, J. Phys. B: At. Mol. Opt. **39**, R1 (2005), URL https://doi.org/10.1088/0953-4075/39/1/r01.

[9] F. Frank, C. Arrell, T. Witting, W. A. Okell, J. McKenna, J. S. Robinson, C. A. Haworth, D. Austin, H. Teng, I. A. Walmsley, et al., Rev. Sci. Instrum. **83**, 071101 (2012), URL https://doi.org/10.1063/1.4731658.

[10] L. Gallmann, C. Cirelli, and U. Keller, Annu. Rev. Phys. Chem. **63**, 447 (2012), URL https://doi.org/10.1146/annurev-physchem-032511-143702.

[11] J. Xu, C. I. Blaga, P. Agostini, and L. F. DiMauro, J. Phys. B: At. Mol. Opt. **49**, 112001 (2016), URL `https://doi.org/10.1088/0953-4075/49/11/112001`.

[12] M. Nisoli, P. Decleva, F. Calegari, A. Palacios, and F. Martín, Chem. Rev. **117**, 10760 (2017), URL `https://doi.org/10.1021/acs.chemrev.6b00453`.

[13] P. M. Kraus, M. Zürch, S. K. Cushing, D. M. Neumark, and S. R. Leone, Nat. Rev. Chem. **2**, 82 (2018), URL `https://doi.org/10.1038/s41570-018-0008-8`.

[14] E. Lindroth, F. Calegari, L. Young, M. Harmand, N. Dudovich, N. Berrah, and O. Smirnova, Nat. Rev. Phys. **1**, 107 (2019), URL `https://doi.org/10.1038/s42254-019-0023-9`.

[15] R. Schoenlein, T. Elsaesser, K. Holldack, Z. Huang, H. Kapteyn, M. Murnane, and M. Woerner, Philos. T. R. Soc. A **377**, 20180384 (2019), URL `https://royalsocietypublishing.org/doi/abs/10.1098/rsta.2018.0384`.

[16] L. Ma, H. Yong, J. D. Geiser, A. Moreno Carrascosa, N. Goff, and P. M. Weber, Struct. Dynam. **7**, 034102 (2020), URL `https://doi.org/10.1063/4.0000010`.

[17] H. Stapelfeldt and T. Seideman, Rev. Mod. Phys. **75**, 543 (2003), URL `https://link.aps.org/doi/10.1103/RevModPhys.75.543`.

[18] S. Pabst, Eur. Phys. J. Spec. Top. **221**, 1 (2013), URL `https://doi.org/10.1140/epjst/e2013-01819-x`.

[19] C. P. Koch, M. Lemeshko, and D. Sugny, Rev. Mod. Phys. **91**, 035005 (2019), URL `https://link.aps.org/doi/10.1103/RevModPhys.91.035005`.

[20] D. Baykusheva and H. J. Wörner, Phys. Rev. X **8**, 031060 (2018), URL `https://link.aps.org/doi/10.1103/PhysRevX.8.031060`.

[21] D. Baykusheva, D. Zindel, V. Svoboda, E. Bommeli, M. Ochsner, A. Tehlar, and H. J. Wörner, P. Natl. A. Sci. **116**, 23923 (2019), URL `https://www.pnas.org/content/116/48/23923`.

[22] J. B. Williams, C. S. Trevisan, M. S. Schöffler, T. Jahnke, I. Bocharova, H. Kim, B. Ulrich, R. Wallauer, F. Sturm, T. N. Rescigno, et al., Phys. Rev. Lett. **108**, 233002 (2012), URL `https://link.aps.org/doi/10.1103/PhysRevLett.108.233002`.

[23] J. Küpper, S. Stern, L. Holmegaard, F. Filsinger, A. Rouzée, A. Rudenko, P. Johnsson, A. V. Martin, M. Adolph, A. Aquila, et al., Phys. Rev. Lett. **112**, 083002 (2014), URL `https://link.aps.org/doi/10.1103/PhysRevLett.112.083002`.

[24] J. Yang and M. Centurion, Struct. Chem. **26**, 1513 (2015), URL `https://link.springer.com/content/pdf/10.1007/s11224-015-0650-4.pdf`.

[25] B. Wolter, M. G. Pullen, A.-T. Le, M. Baudisch, K. Doblhoff-Dier, A. Senftleben, M. Hemmer, C. D. Schröter, J. Ullrich, T. Pfeifer, et al., Science **354**, 308 (2016), URL `http://science.sciencemag.org/content/354/6310/308`.

[26] D. Dill, J. Chem. Phys. **65**, 1130 (1976), URL `https://doi.org/10.1063/1.433187`.

[27] Y.-I. Suzuki, J. Phys. B: At. Mol. Opt. **41**, 215204 (2008), URL `https://iopscience.iop.org/article/10.1088/0953-4075/41/21/215204`.

[28] P. B. Corkum, Phys. Rev. Lett. **71**, 1994 (1993), URL `https://link.aps.org/doi/10.1103/PhysRevLett.71.1994`.

[29] D. Pavičić, K. F. Lee, D. M. Rayner, P. B. Corkum, and D. M. Villeneuve, Phys. Rev. Lett. **98**, 243001 (2007), URL `https://link.aps.org/doi/10.1103/PhysRevLett.98.243001`.

[30] V. Makhija, X. Ren, D. Gockel, A.-T. Le, and V. Kumarappan, *Orientation resolution through rotational coherence spectroscopy* (2016), `arXiv:1611.06476`.

[31] H. V. S. Lam, S. Yarlagadda, A. Venkatachalam, T. N. Wangjam, R. K. Kushawaha, C. Cheng, P. Svihra, A. Nomerotski, T. Weinacht, D. Rolles, et al., Phys. Rev. A **102**, 043119 (2020), URL `https://link.aps.org/doi/10.1103/PhysRevA.102.043119`.

[32] X. M. Tong, Z. X. Zhao, and C. D. Lin, Phys. Rev. A **66**, 033402 (2002), URL https://link.aps.org/doi/10.1103/PhysRevA.66.033402.

[33] P. Krause and H. B. Schlegel, J. Phys. Chem. Lett. **6**, 2140 (2015), URL https://doi.org/10.1021/acs.jpclett.5b00929.

[34] J. Mikosch, A. E. Boguslavskiy, I. Wilkinson, M. Spanner, S. Patchkovskii, and A. Stolow, Phys. Rev. Lett. **110**, 023004 (2013), URL https://link.aps.org/doi/10.1103/PhysRevLett.110.023004.

[35] N. H. Burnett, H. A. Baldis, M. C. Richardson, and G. D. Enright, Appl. Phys. Lett. **31**, 172 (1977), URL https://doi.org/10.1063/1.89628.

[36] A. McPherson, G. Gibson, H. Jara, U. Johann, T. S. Luk, I. A. McIntyre, K. Boyer, and C. K. Rhodes, J. Opt. Soc. Am. B **4**, 595 (1987), URL http://josab.osa.org/abstract.cfm?URI=josab-4-4-595.

[37] M. Ferray, A. L'Huillier, X. F. Li, L. A. Lompre, G. Mainfray, and C. Manus, J. Phys. B: At. Mol. Opt. **21**, L31 (1988), URL https://doi.org/10.1088/0953-4075/21/3/001.

[38] K. J. Schafer, B. Yang, L. F. DiMauro, and K. C. Kulander, Phys. Rev. Lett. **70**, 1599 (1993), URL https://link.aps.org/doi/10.1103/PhysRevLett.70.1599.

[39] M. Uiberacker, T. Uphues, M. Schultze, A. J. Verhoef, V. Yakovlev, M. F. Kling, J. Rauschenberger, N. M. Kabachnik, H. Schröder, M. Lezius, et al., Nature **446**, 627 (2007), URL https://doi.org/10.1038/nature05648.

[40] S. Baker, J. S. Robinson, C. A. Haworth, H. Teng, R. A. Smith, C. C. Chirilă, M. Lein, J. W. G. Tisch, and J. P. Marangos, Science **312**, 424 (2006), URL https://science.sciencemag.org/content/312/5772/424.

[41] P. B. Corkum and F. Krausz, Nat. Phys. **3**, 381 (2007), URL https://doi.org/10.1038/nphys620.

[42] J. Itatani, J. Levesque, D. Zeidler, H. Niikura, H. Pépin, J. C. Kieffer, P. B. Corkum, and D. M. Villeneuve, Nature **432**, 867 (2004), URL `https://doi.org/10.1038/nature03183`.

[43] T. Kanai, S. Minemoto, and H. Sakai, Nature **435**, 470 (2005), URL `https://doi.org/10.1038/nature03577`.

[44] J. B. Bertrand, H. J. Wörner, P. Hockett, D. M. Villeneuve, and P. B. Corkum, Phys. Rev. Lett. **109**, 143001 (2012), URL `https://link.aps.org/doi/10.1103/PhysRevLett.109.143001`.

[45] C. Jin, J. B. Bertrand, R. R. Lucchese, H. J. Wörner, P. B. Corkum, D. M. Villeneuve, A.-T. Le, and C. D. Lin, Phys. Rev. A **85**, 013405 (2012), URL `https://link.aps.org/doi/10.1103/PhysRevA.85.013405`.

[46] X. Ren, V. Makhija, A.-T. Le, J. Troß, S. Mondal, C. Jin, V. Kumarappan, and C. Trallero-Herrero, Phys. Rev. A **88**, 043421 (2013), URL `https://link.aps.org/doi/10.1103/PhysRevA.88.043421`.

[47] P. M. Kraus, D. Baykusheva, and H. J. Wörner, Phys. Rev. Lett. **113**, 023001 (2014), URL `https://link.aps.org/doi/10.1103/PhysRevLett.113.023001`.

[48] B. K. McFarland, J. P. Farrell, P. H. Bucksbaum, and M. Gühr, Science **322**, 1232 (2008), URL `https://science.sciencemag.org/content/322/5905/1232`.

[49] J. Troß, X. Ren, V. Makhija, S. Mondal, V. Kumarappan, and C. A. Trallero-Herrero, Phys. Rev. A **95**, 033419 (2017), URL `https://link.aps.org/doi/10.1103/PhysRevA.95.033419`.

[50] P. M. Kraus, O. I. Tolstikhin, D. Baykusheva, A. Rupenyan, J. Schneider, C. Z. Bisgaard, T. Morishita, F. Jensen, L. B. Madsen, and H. J. Wörner, Nat. Commun. **6**, 7039 (2015), URL `https://doi.org/10.1038/ncomms8039`.

[51] P. M. Kraus, Y. Arasaki, J. B. Bertrand, S. Patchkovskii, P. B. Corkum, D. M. Villeneuve, K. Takatsuka, and H. J. Wörner, Phys. Rev. A **85**, 043409 (2012), URL https://link.aps.org/doi/10.1103/PhysRevA.85.043409.

[52] P. M. Kraus, S. B. Zhang, A. Gijsbertsen, R. R. Lucchese, N. Rohringer, and H. J. Wörner, Phys. Rev. Lett. **111**, 243005 (2013), URL https://link.aps.org/doi/10.1103/PhysRevLett.111.243005.

[53] A. Rupenyan, P. M. Kraus, J. Schneider, and H. J. Wörner, Phys. Rev. A **87**, 031401 (2013), URL https://link.aps.org/doi/10.1103/PhysRevA.87.031401.

[54] D. Baykusheva, P. M. Kraus, S. B. Zhang, N. Rohringer, and H. J. Wörner, Faraday Discuss. **171**, 113 (2014), URL http://dx.doi.org/10.1039/C4FD00018H.

[55] Y. Huang, C. Meng, X. Wang, Z. Lü, D. Zhang, W. Chen, J. Zhao, J. Yuan, and Z. Zhao, Phys. Rev. Lett. **115**, 123002 (2015), URL https://link.aps.org/doi/10.1103/PhysRevLett.115.123002.

[56] S. B. Schoun, A. Camper, P. Salières, R. R. Lucchese, P. Agostini, and L. F. DiMauro, Phys. Rev. Lett. **118**, 033201 (2017), URL https://link.aps.org/doi/10.1103/PhysRevLett.118.033201.

[57] A.-T. Le, R. R. Lucchese, S. Tonzani, T. Morishita, and C. D. Lin, Phys. Rev. A **80**, 013401 (2009), URL https://link.aps.org/doi/10.1103/PhysRevA.80.013401.

[58] M. V. Frolov, N. L. Manakov, T. S. Sarantseva, and A. F. Starace, Phys. Rev. A **83**, 043416 (2011), URL https://link.aps.org/doi/10.1103/PhysRevA.83.043416.

[59] A. D. Shiner, B. E. Schmidt, C. Trallero-Herrero, H. J. Wörner, S. Patchkovskii, P. B. Corkum, J.-C. Kieffer, F. Légaré, and D. M. Villeneuve, Nat. Phys. **7**, 464 (2011), URL https://doi.org/10.1038/nphys1940.

[60] H. Mark and R. Wierl, Zeitschrift für Physik **60**, 741 (1930), URL https://doi.org/10.1007/BF01339959.

[61] L. Pauling and L. O. Brockway, J. Am. Chem. Soc. **57**, 2684 (1935), URL https://doi.org/10.1021/ja01315a103.

[62] M. Centurion, J. Phys. B: At. Mol. Opt. **49**, 062002 (2016), URL https://doi.org/10.1088/0953-4075/49/6/062002.

[63] R. Srinivasan, V. Lobastov, C.-Y. Ruan, and A. Zewail, Helvetica Chimica Acta **86**, 1761 (2003), URL https://onlinelibrary.wiley.com/doi/abs/10.1002/hlca.200390147.

[64] J. C. Williamson, J. Cao, H. Ihee, H. Frey, and A. H. Zewail, Nature **386**, 159 (1997), URL https://doi.org/10.1038/386159a0.

[65] H. Ihee, V. A. Lobastov, U. M. Gomez, B. M. Goodson, R. Srinivasan, C.-Y. Ruan, and A. H. Zewail, Science **291**, 458 (2001), URL https://science.sciencemag.org/content/291/5503/458.

[66] P. Reckenthaeler, M. Centurion, W. Fuß, S. A. Trushin, F. Krausz, and E. E. Fill, Phys. Rev. Lett. **102**, 213001 (2009), URL https://link.aps.org/doi/10.1103/PhysRevLett.102.213001.

[67] X. Shen, J. P. F. Nunes, J. Yang, R. K. Jobe, R. K. Li, M.-F. Lin, B. Moore, M. Niebuhr, S. P. Weathersby, T. J. A. Wolf, et al., Struct. Dynam. **6**, 054305 (2019), URL https://doi.org/10.1063/1.5120864.

[68] Y. Xiong, K. J. Wilkin, and M. Centurion, Phys. Rev. Research **2**, 043064 (2020), URL https://link.aps.org/doi/10.1103/PhysRevResearch.2.043064.

[69] A.-T. Le, M. Centurion, and C. D. Lin, *Elements of Structure Retrieval in Ultrafast Electron and Laser-induced Electron Diffraction from Aligned Polyatomic Molecules* (Royal Society of Chemistry, 2018), chap. 13, pp. 462–493, Theoretical and Computational Chemistry Series, ISBN 978-1-78801-266-9, URL https://doi.org/10.1039/9781788012669-00462.

[70] C. J. Hensley, J. Yang, and M. Centurion, Phys. Rev. Lett. **109**, 133202 (2012), URL https://link.aps.org/doi/10.1103/PhysRevLett.109.133202.

[71] J. Yang, V. Makhija, V. Kumarappan, and M. Centurion, Struct. Dynam. **1**, 044101 (2014), URL https://doi.org/10.1063/1.4889840.

[72] J. Yang, M. Guehr, X. Shen, R. Li, T. Vecchione, R. Coffee, J. Corbett, A. Fry, N. Hartmann, C. Hast, et al., Phys. Rev. Lett. **117**, 153002 (2016), URL https://link.aps.org/doi/10.1103/PhysRevLett.117.153002.

[73] J. Yang, X. Zhu, T. J. A. Wolf, Z. Li, J. P. F. Nunes, R. Coffee, J. P. Cryan, M. Gühr, K. Hegazy, T. F. Heinz, et al., Science **361**, 64 (2018), URL https://science.sciencemag.org/content/361/6397/64.

[74] J. Yang, J. Beck, C. J. Uiterwaal, and M. Centurion, Nat. Commun. **6**, 8172 (2015), URL https://doi.org/10.1038/ncomms9172.

[75] J. Yang, M. Guehr, T. Vecchione, M. S. Robinson, R. Li, N. Hartmann, X. Shen, R. Coffee, J. Corbett, A. Fry, et al., Nat. Commun. **7**, 11232 (2016), URL https://doi.org/10.1038/ncomms11232.

[76] T. J. A. Wolf, D. M. Sanchez, J. Yang, R. M. Parrish, J. P. F. Nunes, M. Centurion, R. Coffee, J. P. Cryan, M. Gühr, K. Hegazy, et al., Nature Chemistry **11**, 504 (2019), URL https://doi.org/10.1038/s41557-019-0252-7.

[77] J. P. F. Nunes and M. Centurion (Academic Press, 2019), vol. 68 of *Advances In Atomic, Molecular, and Optical Physics*, pp. 39–73, URL https://www.sciencedirect.com/science/article/pii/S1049250X19300023.

[78] J. Yang, X. Zhu, J. P. F. Nunes, J. K. Yu, R. M. Parrish, T. J. A. Wolf, M. Centurion, M. Gühr, R. Li, Y. Liu, et al., Science **368**, 885 (2020), URL https://science.sciencemag.org/content/368/6493/885.

[79] T. Zuo, A. Bandrauk, and P. Corkum, Chem. Phys. Lett. **259**, 313 (1996), URL https://www.sciencedirect.com/science/article/pii/0009261496007865.

[80] M. Meckel, D. Comtois, D. Zeidler, A. Staudte, D. Pavičić, H. C. Bandulet, H. Pépin, J. C. Kieffer, R. Dörner, D. M. Villeneuve, et al., Science **320**, 1478 (2008), URL https://science.sciencemag.org/content/320/5882/1478.

[81] T. Morishita, A.-T. Le, Z. Chen, and C. D. Lin, Phys. Rev. Lett. **100**, 013903 (2008), URL https://link.aps.org/doi/10.1103/PhysRevLett.100.013903.

[82] Z. Chen, A.-T. Le, T. Morishita, and C. D. Lin, Phys. Rev. A **79**, 033409 (2009), URL https://link.aps.org/doi/10.1103/PhysRevA.79.033409.

[83] J. Xu, C. I. Blaga, A. D. DiChiara, E. Sistrunk, K. Zhang, Z. Chen, A.-T. Le, T. Morishita, C. D. Lin, P. Agostini, et al., Phys. Rev. Lett. **109**, 233002 (2012), URL https://link.aps.org/doi/10.1103/PhysRevLett.109.233002.

[84] C. I. Blaga, J. Xu, A. D. DiChiara, E. Sistrunk, K. Zhang, P. Agostini, T. A. Miller, L. F. DiMauro, and C. D. Lin, Nature **483**, 194 (2012), URL https://doi.org/10.1038/nature10820.

[85] J. Xu, Z. Chen, A.-T. Le, and C. D. Lin, Phys. Rev. A **82**, 033403 (2010), URL https://link.aps.org/doi/10.1103/PhysRevA.82.033403.

[86] J. Xu, C. I. Blaga, K. Zhang, Y. H. Lai, C. D. Lin, T. A. Miller, P. Agostini, and L. F. DiMauro, Nat. Commun. **5**, 4635 (2014), URL https://doi.org/10.1038/ncomms5635.

[87] M. G. Pullen, B. Wolter, A.-T. Le, M. Baudisch, M. Hemmer, A. Senftleben, C. D. Schröter, J. Ullrich, R. Moshammer, C. D. Lin, et al., Nat. Commun. **6**, 7262 (2015), URL https://doi.org/10.1038/ncomms8262.

[88] M. G. Pullen, B. Wolter, A.-T. Le, M. Baudisch, M. Sclafani, H. Pires, C. D. Schröter,

J. Ullrich, R. Moshammer, T. Pfeifer, et al., Nat. Commun. **7**, 11922 (2016), URL https://doi.org/10.1038/ncomms11922.

[89] B. Wolter, M. G. Pullen, M. Baudisch, M. Sclafani, M. Hemmer, A. Senftleben, C. D. Schröter, J. Ullrich, R. Moshammer, and J. Biegert, Phys. Rev. X **5**, 021034 (2015), URL https://link.aps.org/doi/10.1103/PhysRevX.5.021034.

[90] K. Amini, M. Sclafani, T. Steinle, A.-T. Le, A. Sanchez, C. Müller, J. Steinmetzer, L. Yue, J. R. Martínez Saavedra, M. Hemmer, et al., P. Natl. A. Sci. **116**, 8173 (2019), URL https://www.pnas.org/content/116/17/8173.

[91] E. T. Karamatskos, G. Goldsztejn, S. Raabe, P. Stammer, T. Mullins, A. Trabattoni, R. R. Johansen, H. Stapelfeldt, S. Trippel, M. J. J. Vrakking, et al., J. Chem. Phys. **150**, 244301 (2019), URL https://doi.org/10.1063/1.5093959.

[92] F. Krečinić, P. Wopperer, B. Frusteri, F. Brauße, J.-G. Brisset, U. De Giovannini, A. Rubio, A. Rouzée, and M. J. J. Vrakking, Phys. Rev. A **98**, 041401 (2018), URL https://link.aps.org/doi/10.1103/PhysRevA.98.041401.

[93] Y. Ito, R. Carranza, M. Okunishi, R. R. Lucchese, and K. Ueda, Phys. Rev. A **96**, 053414 (2017), URL https://link.aps.org/doi/10.1103/PhysRevA.96.053414.

[94] Y. Ito, C. Wang, A.-T. Le, M. Okunishi, D. Ding, C. D. Lin, and K. Ueda, Struct. Dynam. **3**, 034303 (2016), URL https://doi.org/10.1063/1.4952602.

[95] H. Fuest, Y. H. Lai, C. I. Blaga, K. Suzuki, J. Xu, P. Rupp, H. Li, P. Wnuk, P. Agostini, K. Yamazaki, et al., Phys. Rev. Lett. **122**, 053002 (2019), URL https://link.aps.org/doi/10.1103/PhysRevLett.122.053002.

[96] F. Schell, T. Bredtmann, C. P. Schulz, S. Patchkovskii, M. J. J. Vrakking, and J. Mikosch, Sci. Adv. **4** (2018), URL https://advances.sciencemag.org/content/4/5/eaap8148.

[97] H. Hu, S. Kangaparambi, M. Dorner-Kirchner, V. Hanus, A. Baltuška, M. Kitzler-Zeiler, and X. Xie, Phys. Rev. A **103**, 013114 (2021), URL https://link.aps.org/doi/10.1103/PhysRevA.103.013114.

[98] C. Yu, H. Wei, X. Wang, A.-T. Le, R. Lu, and C. D. Lin, Sci. Rep. **5**, 15753 (2015), URL https://doi.org/10.1038/srep15753.

[99] M. Chergui and A. H. Zewail, Chem. Phys. Chem. **10**, 28 (2009), URL https://chemistry-europe.onlinelibrary.wiley.com/doi/abs/10.1002/cphc.200800667.

[100] S. Pabst, P. J. Ho, and R. Santra, Phys. Rev. A **81**, 043425 (2010), URL https://link.aps.org/doi/10.1103/PhysRevA.81.043425.

[101] F. Filsinger, G. Meijer, H. Stapelfeldt, H. N. Chapman, and J. Küpper, Phys. Chem. Chem. Phys. **13**, 2076 (2011), URL http://dx.doi.org/10.1039/C0CP01585G.

[102] S. Stern, L. Holmegaard, F. Filsinger, A. Rouzée, A. Rudenko, P. Johnsson, A. V. Martin, A. Barty, C. Bostedt, J. Bozek, et al., Faraday Discuss. **171**, 393 (2014), URL http://dx.doi.org/10.1039/C4FD00028E.

[103] J. M. Glownia, A. Natan, J. P. Cryan, R. Hartsock, M. Kozina, M. P. Minitti, S. Nelson, J. Robinson, T. Sato, T. van Driel, et al., Phys. Rev. Lett. **117**, 153003 (2016), URL https://link.aps.org/doi/10.1103/PhysRevLett.117.153003.

[104] A. Moreno Carrascosa, T. Northey, and A. Kirrander, Phys. Chem. Chem. Phys. **19**, 7853 (2017), URL http://dx.doi.org/10.1039/C6CP06793J.

[105] T. Kierspel, A. Morgan, J. Wiese, T. Mullins, A. Aquila, A. Barty, R. Bean, R. Boll, S. Boutet, P. Bucksbaum, et al., J. Chem. Phys. **152**, 084307 (2020), URL https://doi.org/10.1063/1.5133963.

[106] J. Eland, Int. J. Mass Spec. Ion Phys. **8**, 143 (1972), URL https://www.sciencedirect.com/science/article/pii/0020738172800044.

[107] A. Landers, T. Weber, I. Ali, A. Cassimi, M. Hattass, O. Jagutzki, A. Nauert, T. Osipov, A. Staudte, M. H. Prior, et al., Phys. Rev. Lett. **87**, 013002 (2001), URL `https://link.aps.org/doi/10.1103/PhysRevLett.87.013002`.

[108] J. Ullrich, R. Moshammer, A. Dorn, R. Dörner, L. P. H. Schmidt, and H. Schmidt-Böcking, Rep. Prog. Phys. **66**, 1463 (2003), URL `https://doi.org/10.1088/0034-4885/66/9/203`.

[109] X. M. Tong, Z. X. Zhao, A. S. Alnaser, S. Voss, C. L. Cocke, and C. D. Lin, J. Phys. B: At. Mol. Opt. **38**, 333 (2005), URL `https://doi.org/10.1088/0953-4075/38/4/002`.

[110] J. G. Underwood, I. Procino, L. Christiansen, J. Maurer, and H. Stapelfeldt, Rev. Sci. Instrum. **86**, 073101 (2015), URL `https://doi.org/10.1063/1.4922137`.

[111] L. Christensen, L. Christiansen, B. Shepperson, and H. Stapelfeldt, Phys. Rev. A **94**, 023410 (2016), URL `https://link.aps.org/doi/10.1103/PhysRevA.94.023410`.

[112] D. Reedy, J. B. Williams, B. Gaire, A. Gatton, M. Weller, A. Menssen, T. Bauer, K. Henrichs, P. Burzynski, B. Berry, et al., Phys. Rev. A **98**, 053430 (2018), URL `https://link.aps.org/doi/10.1103/PhysRevA.98.053430`.

[113] Z. L. Streeter, F. L. Yip, R. R. Lucchese, B. Gervais, T. N. Rescigno, and C. W. McCurdy, Phys. Rev. A **98**, 053429 (2018), URL `https://link.aps.org/doi/10.1103/PhysRevA.98.053429`.

[114] K. Lin, X. Hu, S. Pan, F. Chen, Q. Ji, W. Zhang, H. Li, J. Qiang, F. Sun, X. Gong, et al., J. Phys. Chem. Lett. **11**, 3129 (2020), URL `https://doi.org/10.1021/acs.jpclett.0c00599`.

[115] K. H. Kramer and R. B. Bernstein, J. Chem. Phys. **42**, 767 (1965), URL `https://doi.org/10.1063/1.1696004`.

[116] P. R. Brooks, Science **193**, 11 (1976), URL https://science.sciencemag.org/content/193/4247/11.

[117] S. Kaesdorf, G. Schönhense, and U. Heinzmann, Phys. Rev. Lett. **54**, 885 (1985), URL https://link.aps.org/doi/10.1103/PhysRevLett.54.885.

[118] T. P. Rakitzis, A. J. van den Brom, and M. H. M. Janssen, Science **303**, 1852 (2004), URL https://science.sciencemag.org/content/303/5665/1852.

[119] D. Normand, L. A. Lompre, and C. Cornaggia, J. Phys. B: At. Mol. Opt. **25**, L497 (1992), URL https://doi.org/10.1088/0953-4075/25/20/001.

[120] B. Friedrich and D. Herschbach, Phys. Rev. Lett. **74**, 4623 (1995), URL https://link.aps.org/doi/10.1103/PhysRevLett.74.4623.

[121] T. Seideman, J. Chem. Phys. **103**, 7887 (1995), URL https://doi.org/10.1063/1.470206.

[122] W. Kim and P. M. Felker, J. Chem. Phys. **104**, 1147 (1996), URL https://doi.org/10.1063/1.470770.

[123] H. Sakai, C. P. Safvan, J. J. Larsen, K. M. Hilligsøe, K. Hald, and H. Stapelfeldt, J. Chem. Phys. **110**, 10235 (1999), URL https://doi.org/10.1063/1.478039.

[124] J. J. Larsen, K. Hald, N. Bjerre, H. Stapelfeldt, and T. Seideman, Phys. Rev. Lett. **85**, 2470 (2000), URL https://link.aps.org/doi/10.1103/PhysRevLett.85.2470.

[125] S. S. Viftrup, V. Kumarappan, S. Trippel, H. Stapelfeldt, E. Hamilton, and T. Seideman, Phys. Rev. Lett. **99**, 143602 (2007), URL https://link.aps.org/doi/10.1103/PhysRevLett.99.143602.

[126] T. Seideman, Phys. Rev. Lett. **83**, 4971 (1999), URL https://link.aps.org/doi/10.1103/PhysRevLett.83.4971.

[127] F. Rosca-Pruna and M. J. J. Vrakking, Phys. Rev. Lett. **87**, 153902 (2001), URL https://link.aps.org/doi/10.1103/PhysRevLett.87.153902.

[128] S. J. Yun, C. M. Kim, J. Lee, and C. H. Nam, Phys. Rev. A **86**, 051401 (2012), URL https://link.aps.org/doi/10.1103/PhysRevA.86.051401.

[129] S. Weber, M. Ivanov, and J. Marangos, J. Mod. Optic. **60**, 1379 (2013), URL https://doi.org/10.1080/09500340.2013.814925.

[130] J. Mikosch, C. Z. Bisgaard, A. E. Boguslavskiy, I. Wilkinson, and A. Stolow, J. Chem. Phys. **139**, 024304 (2013), URL https://doi.org/10.1063/1.4812787.

[131] C. Marceau, J. B. Bertrand, P. Peng, H. J. Wörner, P. B. Corkum, and D. M. Villeneuve, J. Phys. B: At. Mol. Opt. **53**, 084006 (2020), URL https://iopscience.iop.org/article/10.1088/1361-6455/ab7643.

[132] K. F. Lee, D. M. Villeneuve, P. B. Corkum, A. Stolow, and J. G. Underwood, Phys. Rev. Lett. **97**, 173001 (2006), URL https://link.aps.org/doi/10.1103/PhysRevLett.97.173001.

[133] A. Rouzée, S. Guérin, O. Faucher, and B. Lavorel, Phys. Rev. A **77**, 043412 (2008), URL https://link.aps.org/doi/10.1103/PhysRevA.77.043412.

[134] X. Ren, V. Makhija, and V. Kumarappan, Phys. Rev. Lett. **112**, 173602 (2014), URL https://link.aps.org/doi/10.1103/PhysRevLett.112.173602.

[135] A. Korobenko and V. Milner, Phys. Rev. Lett. **116**, 183001 (2016), URL https://link.aps.org/doi/10.1103/PhysRevLett.116.183001.

[136] P. M. Felker, J. Phys. Chem. **96**, 7844 (1992), URL https://doi.org/10.1021/j100199a005.

[137] I. Thomann, R. Lock, V. Sharma, E. Gagnon, S. T. Pratt, H. C. Kapteyn, M. M. Murnane, and W. Li, J. Phys. Chem. A **112**, 9382 (2008), URL http://dx.doi.org/10.1021/jp8023414.

[138] C. Vozzi, M. Negro, F. Calegari, G. Sansone, M. Nisoli, S. De Silvestri, and S. Stagira, Nat. Phys. **7**, 822 (2011), URL https://doi.org/10.1038/nphys2029.

[139] X. Wang, A.-T. Le, Z. Zhou, H. Wei, and C. D. Lin, Phys. Rev. A **96**, 023424 (2017), URL https://link.aps.org/doi/10.1103/PhysRevA.96.023424.

[140] C. Marceau, V. Makhija, D. Platzer, A. Y. Naumov, P. B. Corkum, A. Stolow, D. M. Villeneuve, and P. Hockett, Phys. Rev. Lett. **119**, 083401 (2017), URL https://link.aps.org/doi/10.1103/PhysRevLett.119.083401.

[141] P. Sándor, A. Sissay, F. m. c. Mauger, P. M. Abanador, T. T. Gorman, T. D. Scarborough, M. B. Gaarde, K. Lopata, K. J. Schafer, and R. R. Jones, Phys. Rev. A **98**, 043425 (2018), URL https://link.aps.org/doi/10.1103/PhysRevA.98.043425.

[142] P. Sándor, A. Sissay, F. Mauger, M. W. Gordon, T. T. Gorman, T. D. Scarborough, M. B. Gaarde, K. Lopata, K. J. Schafer, and R. R. Jones, J. Chem. Phys. **151**, 194308 (2019), URL https://doi.org/10.1063/1.5121711.

[143] L. S. Spector, M. Artamonov, S. Miyabe, T. Martinez, T. Seideman, M. Guehr, and P. H. Bucksbaum, Nat. Commun. **5**, 3190 (2014), URL https://www.nature.com/articles/ncomms4190.pdf.

[144] V. Makhija, Ph.D. thesis, Kansas State University (2014).

[145] R. N. Zare, *Angular Momentum: Understanding Spatial Aspects in Chemistry and Physics* (John Wiley & Sons, Inc, 1988).

[146] C. V. Winter, Physica **20**, 274 (1954), URL https://www.sciencedirect.com/science/article/pii/S0031891454800413.

[147] T. Seideman, J. Chem. Phys. **115**, 5965 (2001), URL https://doi.org/10.1063/1.1400131.

[148] J. Ortigoso, M. Rodríguez, M. Gupta, and B. Friedrich, J. Chem. Phys. **110**, 3870 (1999), URL https://doi.org/10.1063/1.478241.

[149] K. Nakajima, H. Abe, and Y. Ohtsuki, J. Phys. Chem. A **116**, 11219 (2012), URL https://doi.org/10.1021/jp3052054.

[150] X. Ren, V. Makhija, H. Li, M. F. Kling, and V. Kumarappan, Phys. Rev. A **90**, 013419 (2014), URL https://link.aps.org/doi/10.1103/PhysRevA.90.013419.

[151] A. A. Søndergaard, Ph.D. thesis, Aarhus University (2016).

[152] X. Ren, Ph.D. thesis, Kansas State University (2013).

[153] T. Vieillard, F. Chaussard, F. Billard, D. Sugny, O. Faucher, S. Ivanov, J.-M. Hartmann, C. Boulet, and B. Lavorel, Phys. Rev. A **87**, 023409 (2013), URL https://link.aps.org/doi/10.1103/PhysRevA.87.023409.

[154] J. Ma, H. Zhang, B. Lavorel, F. Billard, J. Wu, C. Boulet, J.-M. Hartmann, and O. Faucher, Phys. Rev. A **101**, 043417 (2020), URL https://link.aps.org/doi/10.1103/PhysRevA.101.043417.

[155] S. Ramakrishna and T. Seideman, Phys. Rev. Lett. **95**, 113001 (2005), URL https://link.aps.org/doi/10.1103/PhysRevLett.95.113001.

[156] P. Hockett, New J. Phys. **17**, 023069 (2015), URL https://doi.org/10.1088%2F1367-2630%2F17%2F2%2F023069.

[157] C. T. L. Smeenk, L. Arissian, A. V. Sokolov, M. Spanner, K. F. Lee, A. Staudte, D. M. Villeneuve, and P. B. Corkum, Phys. Rev. Lett. **112**, 253001 (2014), URL https://link.aps.org/doi/10.1103/PhysRevLett.112.253001.

[158] P. Hoerner and H. B. Schlegel, J. Phys. Chem. A **121**, 1336 (2017), URL https://doi.org/10.1021/acs.jpca.6b11415.

[159] V. Makhija, X. Ren, and V. Kumarappan, Phys. Rev. A **85**, 033425 (2012), URL https://link.aps.org/doi/10.1103/PhysRevA.85.033425.

[160] M. Kuhn and K. Johnson, *Applied Predictive Modeling* (Springer-Verlag New York, 2013).

[161] L. Holmegaard, S. S. Viftrup, V. Kumarappan, C. Z. Bisgaard, H. Stapelfeldt, E. Hamilton, and T. Seideman, Phys. Rev. A **75**, 051403 (2007), URL https://link.aps.org/doi/10.1103/PhysRevA.75.051403.

[162] U. Even, EPJ Tech. Instrum. **2**, 17 (2015), URL https://doi.org/10.1140/epjti/s40485-015-0027-5.

[163] S.-F. Zhao, A.-T. Le, C. Jin, X. Wang, and C. D. Lin, Phys. Rev. A **93**, 023413 (2016), URL https://link.aps.org/doi/10.1103/PhysRevA.93.023413.

[164] E. W. Moon, Ph.D. thesis, Kansas State University (2009).

[165] D. Strickland and G. Mourou, Opt. Commun. **56**, 219 (1985), URL https://www.sciencedirect.com/science/article/pii/0030401885901208.

[166] P. Maine, D. Strickland, P. Bado, M. Pessot, and G. Mourou, IEEE J. Quantum Elect. **24**, 398 (1988).

[167] R. Trebino, K. W. DeLong, D. N. Fittinghoff, J. N. Sweetser, M. A. Krümbugel, B. A. Richman, and D. J. Kane, Rev. Sci. Instrum. **68**, 3277 (1997), URL https://doi.org/10.1063/1.1148286.

[168] B. Schaefer, E. Collett, R. Smyth, D. Barrett, and B. Fraher, Am. J. Phys. **75**, 163 (2007), URL https://doi.org/10.1119/1.2386162.

[169] M. Hillenkamp, S. Keinan, and U. Even, J. Chem. Phys. **118**, 8699 (2003), URL https://doi.org/10.1063/1.1568331.

[170] D. Levy, Science **214**, 263 (1981).

[171] L. D. Carr, D. DeMille, R. V. Krems, and J. Ye, New J. Phys. **11**, 055049 (2009), URL https://doi.org/10.1088/1367-2630/11/5/055049.

[172] T. E. Wall, J. Phys. B: At. Mol. Opt. **49**, 243001 (2016), URL `https://doi.org/10.1088/0953-4075/49/24/243001`.

[173] V. Kumarappan, C. Z. Bisgaard, S. S. Viftrup, L. Holmegaard, and H. Stapelfeldt, J. Chem. Phys. **125**, 194309 (2006), URL `https://doi.org/10.1063/1.2388273`.

[174] D. R. Miller, *Free jet sources* (Oxford University Press, 1988), chap. 2, pp. 14–54, Atomic and molecular beam methods, ISBN 0-19-504280-8.

[175] D. M. Morse, *Supersonic beam sources. In Dunning, F., & Hulet, R. (Ed.), Atomic, molecular, and optical physics: Atoms and molecules (Experimental methods in the physical sciences; v. 29B) (pp. 21-47)* (San Diego: Academic Press, 1996).

[176] M. Belan, S. De Ponte, and D. Tordella, Phys. Rev. E **82**, 026303 (2010), URL `https://link.aps.org/doi/10.1103/PhysRevE.82.026303`.

[177] D. W. Chandler and P. L. Houston, J. Chem. Phys. **87**, 1445 (1987), URL `https://doi.org/10.1063/1.453276`.

[178] A. T. J. B. Eppink and D. H. Parker, Rev. Sci. Instrum. **68**, 3477 (1997), URL `https://doi.org/10.1063/1.1148310`.

[179] D. H. Parker, B. L. G. Bakker, R. Delmdahl, T. Berg, and A. T. J. B. Eppink, *Velocity Map Imaging: Technique and Applications to O_2 Photodissociation* (American Chemical Society, 2000), vol. 770 of *ACS Symposium Series*, pp. 56–67, ISBN 9780841236905, 0, URL `https://doi.org/10.1021/bk-2001-0770.ch004`.

[180] N. G. Kling, D. Paul, A. Gura, G. Laurent, S. De, H. Li, Z. Wang, B. Ahn, C. H. Kim, T. K. Kim, et al., J. Instrum. **9**, P05005 (2014).

[181] A. Vajdi, Master's thesis, Kansas State University (2015).

[182] A. Zhao, M. van Beuzekom, B. Bouwens, D. Byelov, I. Chakaberia, C. Cheng, E. Maddox, A. Nomerotski, P. Svihra, J. Visser, et al., Rev. Sci. Instrum. **88**, 113104 (2017).

[183] A. Nomerotski, Nucl. Instrum. Meth. A **937**, 26 (2019), URL http://www.sciencedirect.com/science/article/pii/S0168900219306667.

[184] B.-Y. Chang, R. C. Hoetzlein, J. A. Mueller, J. D. Geiser, and P. L. Houston, Rev. Sci. Instrum. **69**, 1665 (1998), URL https://doi.org/10.1063/1.1148824.

[185] M. Fisher-Levine and A. Nomerotski, J. Instrum. **11**, C03016 (2016), URL https://iopscience.iop.org/article/10.1088/1748-0221/11/03/C03016/pdf.

[186] A. Nomerotski, I. Chakaberia, M. Fisher-Levine, Z. Janoška, P. Takács, and T. Tsang, J. Instrum. **12**, C01017 (2017), URL https://iopscience.iop.org/article/10.1088/1748-0221/12/01/C01017/pdf.

[187] T. Poikela, J. Plosila, T. Westerlund, M. Campbell, M. D. Gaspari, X. Llopart, V. Gromov, R. Kluit, M. V. Beuzekom, F. Zappon, et al., J. Instrum. **9**, C05013 (2014), URL https://iopscience.iop.org/article/10.1088/1748-0221/9/05/C05013/pdf.

[188] B. van der Heijden, J. Visser, M. van Beuzekom, H. Boterenbrood, S. Kulis, B. Munneke, and F. Schreuder, J. Instrum. **12**, C02040 (2017), URL https://iopscience.iop.org/article/10.1088/1748-0221/12/02/C02040/pdf.

[189] M. Fisher-Levine et al., J. Synchrotron Radiat. **25**, 336 (2018), URL http://journals.iucr.org/s/issues/2018/02/00/ve5079/index.html.

[190] L. J. Fransinski, K. Codling, and P. A. Hatherly, Science **246**, 1029 (1989), URL https://science.sciencemag.org/content/246/4933/1029.

[191] A. Rupenyan, P. M. Kraus, J. Schneider, and H. J. Wörner, Phys. Rev. A **87**, 033409 (2013), URL https://link.aps.org/doi/10.1103/PhysRevA.87.033409.

[192] H. Timmers, Z. Li, N. Shivaram, R. Santra, O. Vendrell, and A. Sandhu, Phys. Rev. Lett. **113**, 113003 (2014), URL https://link.aps.org/doi/10.1103/PhysRevLett.113.113003.

[193] A.-T. Le, H. Wei, C. Jin, and C. D. Lin, J. Phys. B: At. Mol. Opt. **49**, 053001 (2016), URL https://iopscience.iop.org/article/10.1088/0953-4075/49/5/053001.

[194] L. He, P. Lan, A.-T. Le, B. Wang, B. Wang, X. Zhu, P. Lu, and C. D. Lin, Phys. Rev. Lett. **121**, 163201 (2018), URL https://link.aps.org/doi/10.1103/PhysRevLett.121.163201.

[195] F. Krečinić, P. Wopperer, B. Frusteri, F. Brauße, J.-G. Brisset, U. De Giovannini, A. Rubio, A. Rouzée, and M. J. J. Vrakking, Phys. Rev. A **98**, 041401 (2018), URL https://link.aps.org/doi/10.1103/PhysRevA.98.041401.

[196] Y. He, L. He, P. Lan, B. Wang, L. Li, X. Zhu, W. Cao, and P. Lu, Phys. Rev. A **99**, 053419 (2019), URL https://link.aps.org/doi/10.1103/PhysRevA.99.053419.

[197] A. M. Perelomov, V. S. Popov, and V. Terentév, JETP **23**, 924 (1965), URL http://www.jetp.ac.ru/cgi-bin/dn/e_064_06_1191.pdf.

[198] M. V. Ammosov, N. B. Delone, and V. P. Krainov, JETP **64**, 1191 (1986), URL http://www.jetp.ac.ru/cgi-bin/dn/e_064_06_1191.pdf.

[199] A. Becker and F. H. M. Faisal, J. Phys. B: At. Mol. Opt. **38**, R1 (2005), URL https://iopscience.iop.org/article/10.1088/0953-4075/38/3/R01.

[200] N. I. Shvetsov-Shilovski, M. Lein, and L. B. Madsen, Phys. Rev. A **98**, 023406 (2018), URL https://link.aps.org/doi/10.1103/PhysRevA.98.023406.

[201] L. B. Madsen, F. Jensen, A. I. Dnestryan, and O. I. Tolstikhin, J. Chem. Phys. **149**, 164107 (2018), URL https://doi.org/10.1063/1.5046902.

[202] S. Petretti, Y. V. Vanne, A. Saenz, A. Castro, and P. Decleva, Phys. Rev. Lett. **104**, 223001 (2010), URL https://link.aps.org/doi/10.1103/PhysRevLett.104.223001.

[203] V. P. Majety and A. Scrinzi, Phys. Rev. Lett. **115**, 103002 (2015), URL https://link.aps.org/doi/10.1103/PhysRevLett.115.103002.

[204] S.-K. Son and S.-I. Chu, Phys. Rev. A **80**, 011403 (2009), URL https://link.aps.org/doi/10.1103/PhysRevA.80.011403.

[205] M. Abu-samha and L. B. Madsen, Phys. Rev. A **80**, 023401 (2009), URL https://link.aps.org/doi/10.1103/PhysRevA.80.023401.

[206] S.-F. Zhao, C. Jin, A.-T. Le, T. F. Jiang, and C. D. Lin, Phys. Rev. A **80**, 051402 (2009), URL https://link.aps.org/doi/10.1103/PhysRevA.80.051402.

[207] M. Spanner and S. Patchkovskii, Phys. Rev. A **80**, 063411 (2009), URL https://link.aps.org/doi/10.1103/PhysRevA.80.063411.

[208] R. Murray, M. Spanner, S. Patchkovskii, and M. Y. Ivanov, Phys. Rev. Lett. **106**, 173001 (2011), URL https://link.aps.org/doi/10.1103/PhysRevLett.106.173001.

[209] G. R. Wu, P. Hockett, and A. Stolow, Phys. Chem. Chem. Phys. **13**, 18447 (2011), URL https://pubs.rsc.org/en/content/articlepdf/2011/cp/c1cp22031d.

[210] H. Shi-Lin, Z. Zeng-Xiu, and S. Ting-Yun, Chinese Phys. Lett. **30**, 103103 (2013), URL http://stacks.iop.org/0256-307X/30/i=10/a=103103.

[211] J. Yao, G. Li, X. Jia, X. Hao, B. Zeng, C. Jing, W. Chu, J. Ni, H. Zhang, H. Xie, et al., Phys. Rev. Lett. **111**, 133001 (2013), URL https://link.aps.org/doi/10.1103/PhysRevLett.111.133001.

[212] M. D. Śpiewanowski and L. B. Madsen, Phys. Rev. A **91**, 043406 (2015), URL https://link.aps.org/doi/10.1103/PhysRevA.91.043406.

[213] V.-H. Hoang, S.-F. Zhao, V.-H. Le, and A.-T. Le, Phys. Rev. A **95**, 023407 (2017), URL https://link.aps.org/doi/10.1103/PhysRevA.95.023407.

[214] I. Petersen, J. Henkel, and M. Lein, Phys. Rev. Lett. **114**, 103004 (2015), URL https://link.aps.org/doi/10.1103/PhysRevLett.114.103004.

[215] X. Shi, W. Li, and B. Schlegel, J. Chem. Phys. **145**, 084309 (2016), URL https://doi.org/10.1063/1.4961644.

[216] X. Shi and H. B. Schlegel, J. Comput. Chem. **40**, 200 (2019), URL https://onlinelibrary.wiley.com/doi/abs/10.1002/jcc.25576.

[217] M. Yoshida, N. Takemoto, and Y. Ohtsuki, Phys. Rev. A **98**, 053434 (2018), URL https://link.aps.org/doi/10.1103/PhysRevA.98.053434.

[218] K. Lin, I. Tutunnikov, J. Qiang, J. Ma, Q. Song, Q. Ji, W. Zhang, H. Li, F. Sun, X. Gong, et al., Nat. Commun. **9**, 5134 (2018), URL https://doi.org/10.1038/s41467-018-07567-2.

[219] Z. Chen and F. He, J. Opt. Soc. Am. B **36**, 2571 (2019), URL http://josab.osa.org/abstract.cfm?URI=josab-36-9-2571.

[220] A. Vickers, *What is a p-value anyway?: 34 stories to help you actually understand statistics* (Addison-Wesley, 2010).

[221] M. S. Gordon and M. W. Schmidt, in *Theory and Applications of Computational Chemistry*, edited by C. E. Dykstra, G. Frenking, K. S. Kim, and G. E. Scuseria (Elsevier, Amsterdam, 2005), pp. 1167–1189, ISBN 978-0-444-51719-7, URL https://www.sciencedirect.com/science/article/pii/B9780444517197500846.

[222] P. B. Lukins and G. L. D. Ritchie, J. Phys. Chem. **89**, 3409 (1985), URL https://doi.org/10.1021/j100261a050.

[223] S.-F. Zhao, J. Xu, C. Jin, A.-T. Le, and C. D. Lin, Journal of Physics B: Atomic, Molecular and Optical Physics **44**, 035601 (2011), URL https://doi.org/10.1088/0953-4075/44/3/035601.

[224] A. F. Alharbi, A. E. Boguslavskiy, N. Thiré, G. S. Thekkadath, S. Patchkovskii, B. E. Schmidt, F. Légaré, T. Brabec, V. R. Bhardwaj, and M. Spanner, Phys. Rev. A **96**, 043402 (2017), URL https://link.aps.org/doi/10.1103/PhysRevA.96.043402.

[225] G. A. Garcia, L. Nahon, and I. Powis, Rev. Sci. Instrum. **75**, 4989 (2004), URL https://doi.org/10.1063/1.1807578.

[226] H. Hu, S. Larimian, S. Erattupuzha, J. Wen, A. Baltuška, M. Kitzler-Zeiler, and X. Xie, Phys. Rev. Research **1**, 033152 (2019), URL https://link.aps.org/doi/10.1103/PhysRevResearch.1.033152.

[227] P. W. Dooley, I. V. Litvinyuk, K. F. Lee, D. M. Rayner, M. Spanner, D. M. Villeneuve, and P. B. Corkum, Phys. Rev. A **68**, 023406 (2003), URL https://link.aps.org/doi/10.1103/PhysRevA.68.023406.

[228] A. S. Mouritzen and K. Mølmer, J. Chem. Phys. **124**, 244311 (2006), URL https://doi.org/10.1063/1.2208351.

[229] E. T. Karamatskos, S. Raabe, T. Mullins, A. Trabattoni, P. Stammer, G. Goldsztejn, R. R. Johansen, K. Długołecki, H. Stapelfeldt, M. J. J. Vrakking, et al., Nat. Commun. **10**, 3364 (2019), URL https://www.nature.com/articles/s41467-019-11122-y.pdf.

[230] A. S. Alnaser, S. Voss, X. M. Tong, C. M. Maharjan, P. Ranitovic, B. Ulrich, T. Osipov, B. Shan, Z. Chang, and C. L. Cocke, Phys. Rev. Lett. **93**, 113003 (2004), URL https://link.aps.org/doi/10.1103/PhysRevLett.93.113003.

[231] Z. Wu, C. Wu, X. Liu, Y. Deng, Q. Gong, D. Song, and H. Su, J. Phys. Chem. A **114**, 6751 (2010), URL https://doi.org/10.1021/jp1018197.

[232] S. De, M. Magrakvelidze, I. A. Bocharova, D. Ray, W. Cao, I. Znakovskaya, H. Li, Z. Wang, G. Laurent, U. Thumm, et al., Phys. Rev. A **84**, 043410 (2011), URL https://link.aps.org/doi/10.1103/PhysRevA.84.043410.

[233] L.-E. Berg, P. Erman, E. Källne, S. Sorensen, and G. Sundström, Phys. Scripta **44**, 131 (1991), URL https://doi.org/10.1088/0031-8949/44/2/003.

[234] T. Ayari, M. Desouter-Lecomte, R. Linguerri, G. A. Garcia, L. Nahon, A. B. Houria, H. Ghalila, R. B. Said, and M. Hochlaf, Adv. Phys. **5**, 1831955 (2020), URL `https://doi.org/10.1080/23746149.2020.1831955`.

[235] A. Natan, M. R. Ware, V. S. Prabhudesai, U. Lev, B. D. Bruner, O. Heber, and P. H. Bucksbaum, Phys. Rev. Lett. **116**, 143004 (2016), URL `https://link.aps.org/doi/10.1103/PhysRevLett.116.143004`.

[236] A. Rudenko, V. Makhija, A. Vajdi, T. Ergler, M. Schürholz, R. K. Kushawaha, J. Ullrich, R. Moshammer, and V. Kumarappan, Faraday Discuss. **194**, 463 (2016), URL `http://dx.doi.org/10.1039/C6FD00152A`.

[237] M. Wollenhaupt, M. Krug, J. Köhler, T. Bayer, C. Sarpe-Tudoran, and T. Baumert, Appl. Phys. B **95**, 647 (2009), URL `https://doi.org/10.1007/s00340-009-3513-0`.

[238] C. Smeenk, L. Arissian, A. Staudte, D. M. Villeneuve, and P. B. Corkum, J. Phys. B: At. Mol. Opt. **42**, 185402 (2009), URL `https://doi.org/10.1088/0953-4075/42/18/185402`.

[239] J. Maurer, D. Dimitrovski, L. Christensen, L. B. Madsen, and H. Stapelfeldt, Phys. Rev. Lett. **109**, 123001 (2012), URL `https://link.aps.org/doi/10.1103/PhysRevLett.109.123001`.

[240] D. M. Neumark, Annu. Rev. Phys. Chem. **52**, 255 (2001), URL `https://doi.org/10.1146/annurev.physchem.52.1.255`.

[241] T. Suzuki, Annu. Rev. Phys. Chem. **57**, 555 (2006), URL `https://doi.org/10.1146/annurev.physchem.57.032905.104601`.

[242] Y. Arasaki, K. Takatsuka, K. Wang, and V. McKoy, J. Chem. Phys. **132**, 124307 (2010), URL `https://doi.org/10.1063/1.3369647`.

[243] F. Kelkensberg, A. Rouzée, W. Siu, G. Gademann, P. Johnsson, M. Lucchini, R. R.

Lucchese, and M. J. J. Vrakking, Phys. Rev. A **84**, 051404 (2011), URL https://link.aps.org/doi/10.1103/PhysRevA.84.051404.

[244] A. Rouzée, A. G. Harvey, F. Kelkensberg, D. Brambila, W. K. Siu, G. Gademann, O. Smirnova, and M. J. J. Vrakking, J. Phys. B: At. Mol. Opt. **47**, 124017 (2014), URL https://doi.org/10.1088/0953-4075/47/12/124017.

[245] S. Minemoto, H. Shimada, K. Komatsu, W. Komatsubara, T. Majima, S. Miyake, T. Mizuno, S. Owada, H. Sakai, T. Togashi, et al., J. Phys. Commun. **2**, 115015 (2018).

[246] C. Marceau, V. Makhija, P. Peng, M. Hervé, P. B. Corkum, A. Y. Naumov, A. Stolow, and D. M. Villeneuve, Phys. Rev. A **99**, 023426 (2019), URL https://link.aps.org/doi/10.1103/PhysRevA.99.023426.

[247] V. Kumarappan, L. Holmegaard, C. Martiny, C. B. Madsen, T. K. Kjeldsen, S. S. Viftrup, L. B. Madsen, and H. Stapelfeldt, Phys. Rev. Lett. **100**, 093006 (2008), URL https://link.aps.org/doi/10.1103/PhysRevLett.100.093006.

[248] C. Z. Bisgaard, O. J. Clarkin, G. Wu, A. M. D. Lee, O. Geßner, C. C. Hayden, and A. Stolow, Science **323**, 1464 (2009), URL https://science.sciencemag.org/content/323/5920/1464.

[249] Y. Tang, Y.-I. Suzuki, T. Horio, and T. Suzuki, Phys. Rev. Lett. **104**, 073002 (2010), URL https://link.aps.org/doi/10.1103/PhysRevLett.104.073002.

[250] P. Hockett, C. Z. Bisgaard, O. J. Clarkin, and A. Stolow, Nat. Phys. **7**, 612 (2011), URL https://doi.org/10.1038/nphys1980.

[251] H. Fukuzawa, S. Yamada, Y. Sakakibara, T. Tachibana, Y. Ito, T. Takanashi, T. Nishiyama, T. Sakai, K. Nagaya, N. Saito, et al., J. Chem. Phys. **151**, 104302 (2019), URL https://doi.org/10.1063/1.5115801.

[252] H. Fukuzawa, R. R. Lucchese, X.-J. Liu, K. Sakai, H. Iwayama, K. Nagaya, K. Kreidi, M. S. Schöffler, J. R. Harries, Y. Tamenori, et al., J. Chem. Phys. **150**, 174306 (2019), URL `https://doi.org/10.1063/1.5091946`.

[253] V. Makhija, K. Veyrinas, A. E. Boguslavskiy, R. Forbes, I. Wilkinson, R. Lausten, S. P. Neville, S. T. Pratt, M. S. Schuurman, and A. Stolow, J. Phys. B: At. Mol. Opt. **53**, 114001 (2020), URL `https://doi.org/10.1088/1361-6455/ab7a84`.

[254] J. Arlt, D. P. Singh, J. O. F. Thompson, A. S. Chatterley, P. Hockett, H. Stapelfeldt, and K. L. Reid, Mol. Phys. **119**, e1836411 (2021), URL `https://doi.org/10.1080/00268976.2020.1836411`.

[255] J. G. Underwood and K. L. Reid, J. Chem. Phys. **113**, 1067 (2000), URL `https://doi.org/10.1063/1.481918`.

[256] T. Seideman, Annu. Rev. Phys. Chem. **53**, 41 (2002), URL `https://doi.org/10.1146/annurev.physchem.53.082101.130051`.

[257] Y.-I. Suzuki and T. Suzuki, Mol. Phys. **105**, 1675 (2007), URL `https://doi.org/10.1080/00268970701551864`.

[258] A. Stolow and J. G. Underwood, *Time-Resolved Photoelectron Spectroscopy of Nonadiabatic Dynamics in Polyatomic Molecules. In Stuart A. Rice (Ed.) Advances in Chemical Physics, Volume 139* (John Wiley & Sons, Inc., 2008).

[259] S. Ramakrishna and T. Seideman, J. Phys. B: At. Mol. Opt. **45**, 194012 (2012), URL `https://doi.org/10.1088%2F0953-4075%2F45%2F19%2F194012`.

[260] F. Jin, H. Yang, H. Zhang, B. Wang, and W. Yang, Opt. Express **29**, 10726 (2021), URL `http://www.opticsexpress.org/abstract.cfm?URI=oe-29-7-10726`.

[261] P. Hockett, M. Wollenhaupt, C. Lux, and T. Baumert, Phys. Rev. Lett. **112**, 223001 (2014), URL `https://link.aps.org/doi/10.1103/PhysRevLett.112.223001`.

[262] A. J. Yencha, K. Ellis, and G. C. King, J. Electron Spectrosc. **195**, 160 (2014), URL http://www.sciencedirect.com/science/article/pii/S0368204814001522.

[263] S. Petretti, A. Magaña, A. Saenz, and P. Decleva, Phys. Rev. A **94**, 053411 (2016), URL https://link.aps.org/doi/10.1103/PhysRevA.94.053411.

[264] M. Gregory, P. Hockett, A. Stolow, and V. Makhija, *Molecular frame photoelectron angular distributions in polyatomic molecules from lab frame coherent rotational wavepacket evolution* (2020), arXiv:2012.04561.

[265] D. M. Mintz and A. Kuppermann, J. Chem. Phys. **71**, 3499 (1979), URL https://doi.org/10.1063/1.438739.

[266] G. Kaya, N. Kaya, J. Strohaber, N. A. Hart, A. A. Kolomenskii, and H. A. Schuessler, *Nonadiabatic Molecular Alignment of Linear Molecules Probed by Strong-Field Ionization Yields of Photoelectrons* (Springer International Publishing, Cham, 2018), pp. 577–595, ISBN 978-3-319-64346-5, URL https://doi.org/10.1007/978-3-319-64346-5_31.

[267] M. Bérard, P. Lallemand, J. P. Cebe, and M. Giraud, J. Chem. Phys. **78**, 672 (1983), URL https://doi.org/10.1063/1.444811.

[268] K. Sonoda, S. Fukahori, and H. Hasegawa, Phys. Rev. A **103**, 033118 (2021), URL https://link.aps.org/doi/10.1103/PhysRevA.103.033118.

[269] M. Zohrabi, J. McKenna, B. Gaire, N. G. Johnson, K. D. Carnes, S. De, I. A. Bocharova, M. Magrakvelidze, D. Ray, I. V. Litvinyuk, et al., Phys. Rev. A **83**, 053405 (2011), URL https://link.aps.org/doi/10.1103/PhysRevA.83.053405.

[270] M. Magrakvelidze, C. M. Aikens, and U. Thumm, Phys. Rev. A **86**, 023402 (2012), URL https://link.aps.org/doi/10.1103/PhysRevA.86.023402.

[271] Y. Malakar, F. Wilhelm, D. Trabert, K. R. P., X. Li, W. L. Pearson, W. Cao,

B. Kaderiya, I. Ben-Itzhak, and A. Rudenko, Phys. Rev. A **98**, 013418 (2018), URL https://link.aps.org/doi/10.1103/PhysRevA.98.013418.

[272] S. Xue, H. Du, B. Hu, C. D. Lin, and A.-T. Le, Phys. Rev. A **97**, 043409 (2018), URL https://link.aps.org/doi/10.1103/PhysRevA.97.043409.

[273] V. Singh, A. K. Samanta, N. Roth, D. Gusa, T. Ossenbrüggen, I. Rubinsky, D. A. Horke, and J. Küpper, Phys. Rev. A **97**, 032704 (2018), URL https://link.aps.org/doi/10.1103/PhysRevA.97.032704.

[274] K. Hegazy, *Extracting body frame molecular geometry from ultrafast diffraction gas-phase experiments through coherent ensemble anisotropy*, 52nd Annual Meeting of the APS Division of Atomic, Molecular and Optical Physics (2021).

[275] D. Rolles, *Strong-field ionization of toluene studied by mass spectrometry and ultrafast electron diffraction*, K-State Physics Department AMO seminar (2021).

Appendix A

Supporting materials for photoelectron experiments

A.1 Propagation of uncertainty

Assuming there is no covariance between quantities, the uncertainty of simple functions of the real variables A, B, with standard deviations σ_A, σ_B and exactly known (deterministic) real-valued constants a, b can be propagated using the following formulas

Function	Standard deviation
$f = aA$	$\lvert a\rvert\sigma_A$
$f = aA \pm bB$	$\sqrt{a^2\sigma_A^2 + b^2\sigma_B^2}$
$f = AB$ or A/B	$\lvert f\rvert\sqrt{(\sigma_A/A)^2 + (\sigma_B/B)^2}$

In the first step, after constructing the corrected time-dependent VMI images as described in Eq. (6.2), we estimate the uncertainty of the mean of each pixel (i, j) at each delay by the statistical error

$$\sigma_m(i, j) = \frac{\sigma_d(i, j)}{\sqrt{N}}, \tag{A.1}$$

where σ_d is the width of the distribution and N is the number of scans. For each VMI image, we have a corresponding image of uncertainty with pixel-to-pixel mapping.

Since the VMI images are four-fold symmetric, we can fold each image into one quadrant to increase the statistics. At this step, the uncertainties of the four averaged pixels are added in quadrature. The images can also be Gauss-smoothed to reduce pixel noise. Since the convolution with a Gaussian filter generates a weighted average of neighboring pixels, the uncertainty can be calculated by using the expression for $f = aA + bB$ from the table. Both the error image and the Gaussian kernel are squared element-by-element and then convoluted. The square root of the result then gives the new error estimate for the VMI image.

These VMI images and their corresponding uncertainty images are then fed into the pBasex algorithm for inversion. The original pBasex algorithm[225] does not treat uncertainty and does not produce the uncertainty of the output coefficients. Our version of pBasex weights the mean value of each pixel with its uncertainty and uses linear regression through Single Value Decomposition to find the fitting coefficients, $C_L(k,t)$, and their errors. Similar to the previous steps, errors were propagated through Eq. (6.7). For each channel, we average over a range of radial momentum, k, and then obtain the average delay-dependent coefficients and their uncertainty for the channel, $C_{kL}(t) \pm \sigma^C_{kL}(t)$.

Finally, these delay-dependent coefficients and errors are fed into the ORRCS algorithm that uses linear regression to retrieve the real coefficients, $A_{JL}(k) \pm \sigma^A_{JL}(k)$, which determine the YCAR-LFPAD through Eq. (6.2).

A.2 Connections between LFPADs and MFPADs

In this section of the appendix, we would like to discuss the connections between the laboratory-frame photoelectron angular distributions (LFPAD) and the molecular-frame photoelectron angular distribution (MFPAD). In particular, we discuss how to construct LFPADs from MFPADs and how to extract MFPADs from measurements of LFPADs. We will explain why the information around the laser polarization direction was lost because of the cylindrical symmetry of the LF measurement, what needs to be done to recover this dependence, and we will spell out the relation between our retrieved real coefficients and the complex coefficients that described the outgoing photoelectron wave function.

A.2.1 Photoelectron wave function expressed in the LF angles

In the LF, consider a molecule at an orientation described by $(\theta, \phi = 0)$ ionized by a linearly polarized pulse. The outgoing photoelectron wave function, in its asymptotic form, can be written as

$$\psi^e = \frac{e^{ikr}}{r} \sum_{lm} \tilde{c}_{lm}(\theta, k) Y_l^m(\theta_k, \phi_k), \tag{A.2}$$

where all the molecular and ionization dynamics are encoded in the $\tilde{c}_{lm}(\theta, k)$ coefficients.

The wave function for a molecule at any orientation described by an arbitrary azimuthal angle ϕ and the same polar angle θ can be obtained by rotating this function about the LF Z-axis.

$$\psi^e = \frac{e^{ikr}}{r} \sum_{lm} \tilde{c}_{lm}(\theta, k) \sum_{m'} D^J_{m'm}(\phi, \theta = 0, \chi = 0) Y_l^{m'}(\theta_k, \phi_k), \tag{A.3}$$

with $\tilde{c}_{lm}$ outside of the m' summation since it does not depend on ϕ.

In this case, the Wigner-D rotation matrix reduces to

$$D^J_{m'm}(\phi, \theta = 0, \chi = 0) = \sum_{m'} e^{-im'\phi} \delta_{mm'}. \tag{A.4}$$

Hence, the wave function is

$$\psi^e = \frac{e^{ikr}}{r}\sum_{lm}\tilde{c}_{lm}(\theta,k)e^{-im\phi}Y_l^m(\theta_k,\phi_k). \tag{A.5}$$

This form of the equation shows that only the difference between ϕ and ϕ_k (i.e., $\phi - \phi_k$) matters but not the absolute values of the two angles because $Y_l^m(\theta_k,\phi_k) \sim e^{im\phi_k}$.

In scattering theory, the outgoing wave is written in the form of $\frac{e^{ikr}}{r}f(\theta_k,\phi_k)$, and the differential cross section (DCS) will then be defined as $|f(\theta_k,\phi_k)|^2$. Therefore, in this case, the dependence of the FR-LFPAD on the molecular orientation is

$$\frac{d\sigma}{dkd\Omega d\Omega_k} = \left|\sum_{lm}\tilde{c}_{lm}(\theta,k)e^{-im\phi}Y_l^m(\theta_k,\phi_k)\right|^2, \tag{A.6}$$

where $d\Omega$ expresses the dependence on θ and ϕ, and $d\Omega_k$ expresses the dependence on θ_k and ϕ_k. This FR-LFPAD is equivalent to the MFPAD (or the MF interferogram) written in LF angles (i.e., $\theta,\phi,\theta_k,\phi_k$). It can be expressed in terms of the MF angles by a rotation connecting the two frames. Both contain the same information since no averaging has been done, and rotation does not affect the shape of the distribution.

The modulus square in Eq. (A.6) can be written as a double sum

$$\frac{d\sigma}{dkd\Omega d\Omega_k} = \sum_{lm}\sum_{l'm'}\tilde{c}_{lm}(\theta,k)\tilde{c}^*_{l'm'}(\theta,k)e^{-i(m-m')\phi}Y_l^m(\theta_k,\phi_k)\left[Y_{l'}^{m'}(\theta_k,\phi_k)\right]^*. \tag{A.7}$$

This expression can be simplified by expanding the product of the two spherical harmonics as a series by using the contraction rule

$$\begin{aligned}\frac{d\sigma}{dkd\Omega d\Omega_k} =& \sum_{lm}\sum_{l'm'}\tilde{c}_{lm}(\theta,k)\tilde{c}^*_{l'm'}(\theta,k)e^{-i(m-m')\phi}\\ &\times\sum_{LM}\langle l,0,l',0|L0\rangle\langle l,m,l',-m'|LM\rangle\\ &\times(-1)^{m'}\sqrt{\frac{(2l+1)(2l'+1)}{4\pi(2L+1)}}Y_L^M(\theta_k,\phi_k).\end{aligned} \tag{A.8}$$

The dependence of the $\tilde{c}_{lm}(\theta, k)$ coefficients on the polar angle θ can be expanded in the Legendre polynomial basis as

$$\tilde{c}_{lm}(\theta, k) = \sum_{j} \tilde{a}_{lmj}(k) P_j(\cos\theta). \tag{A.9}$$

The FR-LFPAD then becomes

$$\begin{aligned}\frac{d\sigma}{dk d\Omega d\Omega_k} = &\sum_{lm}\sum_{l'm'}\sum_{LM}\sum_{jj'} \tilde{a}_{lmj}(k)\tilde{a}^*_{l'm'j'}(k) \\ &\times (-1)^{m'} e^{-i(m-m')\phi} P_j(\cos\theta) P_{j'}(\cos\theta) \\ &\times \langle l, 0, l', 0|L0\rangle \langle l, m, l', -m'|LM\rangle \\ &\times \sqrt{\frac{(2l+1)(2l'+1)}{4\pi(2L+1)}} Y_L^M(\theta_k, \phi_k).\end{aligned} \tag{A.10}$$

The product of two Legendre polynomials can also be expanded in a series, this leads to

$$\begin{aligned}\frac{d\sigma}{dk d\Omega d\Omega_k} = &\sum_{lm}\sum_{l'm'}\sum_{LM}\sum_{jj'}\sum_{J} \tilde{a}_{lmj}(k)\tilde{a}^*_{l'm'j'}(k)(-1)^{m'} e^{-i(m-m')\phi} \\ &\times \langle j, 0, j', 0|J0\rangle^2 P_J(\cos\theta) \\ &\times \langle l, 0, l', 0|L0\rangle \langle l, m, l', -m'|LM\rangle \\ &\times \sqrt{\frac{(2l+1)(2l'+1)}{4\pi(2L+1)}} Y_L^M(\theta_k, \phi_k).\end{aligned} \tag{A.11}$$

As discussed previously[140,156,255,258], the measured LFPAD is a summation of the FR-LFPAD in Eq. (A.11) weighted by the time-dependent molecular axis distribution $\rho(\theta, t)$ excited by the alignment pulse. Technically, we need to multiply Eq. (A.11) by $\rho(\theta, t)$ and average over θ and ϕ.

Since $\rho(\theta, t)$ does not depend on ϕ, we can perform the integration over ϕ independently first, then multiply by $\rho(\theta, t)$ and average over θ later. The integral over ϕ is non-zero only if $m = m'$, which makes $M = 0$. This gives

$$\begin{aligned}\frac{d\sigma}{dkd\theta d\theta_k} =&2\pi \sum_L \sum_J \sum_{ll'm} \sum_{jj'} \tilde{a}_{lmj}(k)\tilde{a}^*_{l'mj'}(k)\frac{(-1)^m}{4\pi}\sqrt{(2l+1)(2l'+1)} \\ &\times \langle j,0,j',0|J0\rangle^2 \langle l,0,l',0|L0\rangle\langle l,m,l',-m|L0\rangle \\ &\times P_J(\cos\theta)P_L(\cos\theta_k),\end{aligned} \tag{A.12}$$

where the dependence on ϕ and ϕ_k is gone.

The $\rho(\theta,t)$-weighted integration over θ then gives us the time-dependent photoelectron spectrum measured in the LF

$$\begin{aligned}\frac{d\sigma}{dkd\theta_k} =&2\pi \sum_L \sum_J \sum_{ll'm} \sum_{jj'} \tilde{a}_{lmj}(k)\tilde{a}^*_{l'mj'}(k) \\ &\times \frac{(-1)^m}{4\pi}\sqrt{(2l+1)(2l'+1)} \\ &\times \langle j,0,j',0|J0\rangle^2 \langle l,0,l',0|L0\rangle\langle l,m,l',-m|L0\rangle \\ &\times \langle P_J(\cos\theta)(t)\rangle P_L(\cos\theta_k),\end{aligned} \tag{A.13}$$

where

$$\langle P_J(\cos\theta)\rangle(t) = \int P_J(\cos\theta)\rho(\theta,t)\sin\theta d\theta \tag{A.14}$$

is the time-dependent axis distribution moment.

The expression in Eq. (A.13) is equivalent to Eq. (6.5) in section 6.2. By comparing the two, we can obtain

$$\begin{aligned}A_{JL}(k) =&\sum_{ll'm} \sum_{jj'} \tilde{a}_{lmj}(k)\tilde{a}^*_{l'mj'}(k) \\ &\times \frac{(-1)^m}{4\pi}\sqrt{(2l+1)(2l'+1)} \\ &\times \langle j,0,j',0|J0\rangle^2 \\ &\times \langle l,0,l',0|L0\rangle\langle l,m,l',-m|L0\rangle,\end{aligned} \tag{A.15}$$

where $A_{JL}(k)$ are the real coefficients that we retrieved in the chapter.

The complex coefficients, $\tilde{a}_{lmj}(k)$, and hence $\tilde{c}_{lm}(k)$ and the outgoing photoelectron wave function, can be retrieved by fitting the real coefficients $A_{JL}(k)$ to the expansion in Eq. (A.15). A proper ionization model limits the number of terms involved in the fit. Without constraints imposed by the knowledge about the ionization process, the parameter space is too large and the fitting problem becomes too big to be solved reliably (in other words, it can become a massive under-deterministic problem where the number of parameters that need to be determined is way more than the number of independent parameters that can be measured in the LF).

In chapter 6, we did not perform this fitting step to retrieve those complex coefficients, and hence, could not retrieve the FR-LFPAD in Eq. (A.11) (or equivalently, the MFPAD). However, by retrieving the real coefficients $A_{JL}(k)$ we did retrieve the AR-LFPAD in Eq. (A.27), where the θ-dependent is recovered, but the information about the laser polarization axis was lost from the integration over the azimuthal angle ϕ because of the cylindrically symmetric distribution. In terms of $A_{JL}(k)$, this AR-LFPAD can be re-written as

$$\frac{d\sigma}{d\theta d\theta_k} = 2\pi \sum_{JL} A_{JL}(k) P_J(\cos\theta) P_L(\cos\theta_k), \tag{A.16}$$

which is the form that we use in chapter 6.

A.2.2 Photoelectron wave function expressed in the MF angles

In this section, we would like to express the same relations established in the previous section but by starting from the MF photoelectron wave function and constructing the LFPAD at the end. In the MF, consider a molecule ionized by a linearly polarized pulse at a polarization geometry described by $(\theta_s, \phi_s = 0)$. The asymptotic photoelectron wave function can be written as

$$\psi^e_{MF} = \frac{e^{ikr}}{r} \sum_{lm} \tilde{b}_{lm}(k, \theta_s) Y_l^m(\theta_e, \phi_e), \tag{A.17}$$

where all the molecular and ionization dynamics are encoded in $\tilde{b}_{lm}(k, \theta_s)$.

The photoelectron wave function created by ionization at any polarization geometry described by an arbitrary azimuthal angle ϕ_s and the same polar angle θ_s can be obtained by rotating this function about the MF z-axis.

$$\psi^e_{MF} = \frac{e^{ikr}}{r} \sum_{lm} \tilde{b}_{lm}(k, \theta_s) \sum_{m'} D^l_{m'm}(\phi_s, 0, 0) Y_l^{m'}(\theta_e, \phi_e), \tag{A.18}$$

with $\tilde{b}_{lm}$ outside of the m' summation since it does not depend on ϕ_s.

As before, the Wigner-D rotation matrix reduces to $\sum_{m'} e^{-im'\phi_s}\delta_{mm'}$ and the photoelectron wave function becomes

$$\psi^e_{MF} = \frac{e^{ikr}}{r} \sum_{lm} \tilde{b}_{lm}(k, \theta_s) e^{-im\phi_s} Y_l^m(\theta_e, \phi_e). \tag{A.19}$$

In the LF, this photoelectron wave function can be written as

$$\begin{aligned} \psi^e_{LF} =& \mathbf{R}(\phi, \theta, \chi) \frac{e^{ikr}}{r} \sum_{lm} \tilde{b}_{lm}(k, \theta_s) e^{-im\phi_s} Y_l^m(\theta_e, \phi_e) \\ =& \frac{e^{ikr}}{r} \sum_{lm} \tilde{b}_{lm}(k, \theta) e^{-im\chi} \sum_{m_1} D^l_{m_1 m}(\phi, \theta, \chi) Y_l^{m_1}(\theta_k, \phi_k), \end{aligned} \tag{A.20}$$

where the rotation $\mathbf{R}(\phi, \theta, \chi) = \sum_{m_1} D^l_{m_1 m}(\phi, \theta, \chi)$ brings the LF to coincide with the MF (see Fig. A.1).

The dependence of the DCS on the molecular orientation is

$$\frac{d\sigma}{d\Omega d\Omega_k} = \left| \sum_{lm} \tilde{b}_{lm}(k, \theta) e^{-im\chi} \sum_{m_1} D^l_{m_1 m}(\phi, \theta, \chi) Y_l^{m_1}(\theta_k, \phi_k) \right|^2, \tag{A.21}$$

where $\Omega\Omega_k = \{\theta, \phi, \chi, \theta_k, \phi_k\}$. This fully angle-resolved DCS can be referred to as the MFPAD written in LF angles (i.e., $\theta, \phi, \chi, \theta_k, \phi_k$). The fully angle-resolved DCS and the MFPAD contain the same information (i.e., the dependence of the PAD on five angles) since no averaging has been done, and rotation does not affect the shape of the distribution. The two are connected by the rotation $\mathbf{R}(\phi, \theta, \chi)$.

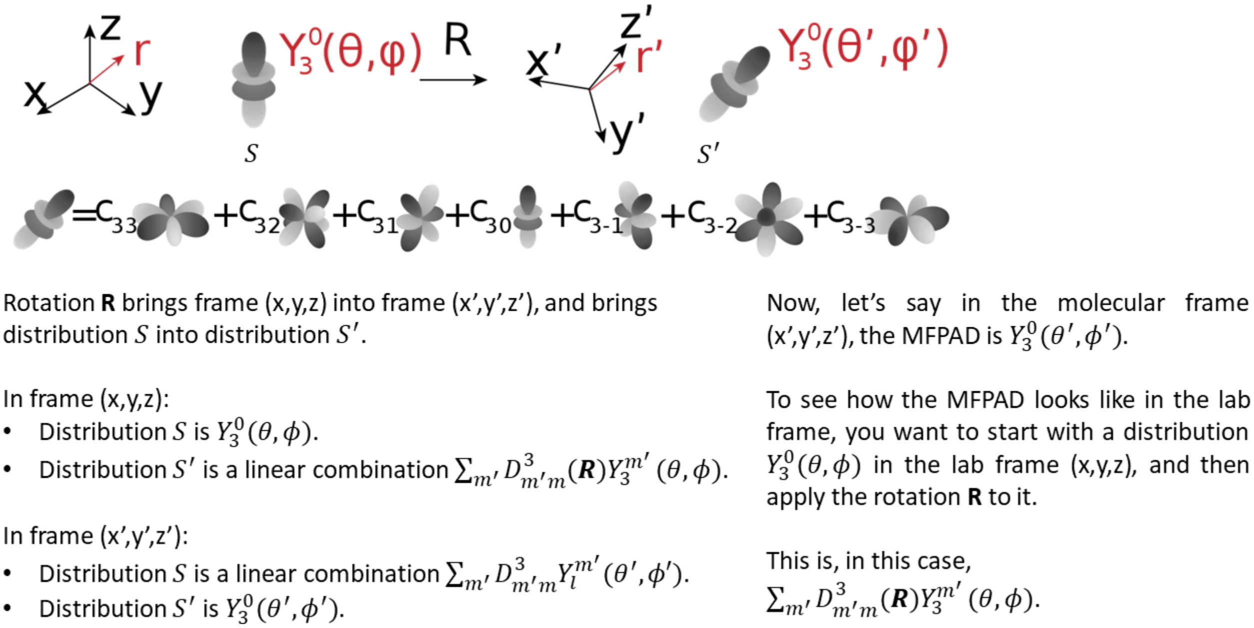

Rotation **R** brings frame (x,y,z) into frame (x',y',z'), and brings distribution S into distribution S'.

In frame (x,y,z):

- Distribution S is $Y_3^0(\theta,\phi)$.
- Distribution S' is a linear combination $\sum_{m'} D^3_{m'm}(\boldsymbol{R}) Y_3^{m'}(\theta,\phi)$.

In frame (x',y',z'):

- Distribution S is a linear combination $\sum_{m'} D^3_{m'm} Y_l^{m'}(\theta',\phi')$.
- Distribution S' is $Y_3^0(\theta',\phi')$.

Now, let's say in the molecular frame (x',y',z'), the MFPAD is $Y_3^0(\theta',\phi')$.

To see how the MFPAD looks like in the lab frame, you want to start with a distribution $Y_3^0(\theta,\phi)$ in the lab frame (x,y,z), and then apply the rotation **R** to it.

This is, in this case, $\sum_{m'} D^3_{m'm}(\boldsymbol{R}) Y_3^{m'}(\theta,\phi)$.

Figure A.1: *A note on frame transformation.*

The modulus square in Eq. (A.21) can be written as a double sum

$$
\begin{aligned}
\frac{d\sigma}{d\Omega d\Omega_k} = \sum_{lm}\sum_{l'm'}\sum_{m_1}\sum_{m_1'} & \tilde{b}_{lm}(k,\theta)\tilde{c}^*_{l'm'}(k,\theta)e^{-i(m-m')\chi} \\
& \times D^l_{m_1 m}(\phi,\theta,\chi)\left[D^{l'}_{m_1' m'}(\phi,\theta,\chi)\right]^* \\
& \times Y_l^{m_1}(\theta_k,\phi_k)\left[Y_{l'}^{m_1'}(\theta_k,\phi_k)\right]^* .
\end{aligned}
\tag{A.22}
$$

This expression can be simplified by rewriting the product of two Wigner-D functions as a Clebsch-Gordan series (Zare, page 99)[145] and expanding the product of the two spherical harmonics as a series by using the contraction rule

$$\begin{aligned}\frac{d\sigma}{d\Omega d\Omega_k} =& \sum_{lm}\sum_{l'm'}\sum_{m_1}\sum_{m_1'} \tilde{b}_{lm}(k,\theta)\tilde{c}^*_{l'm'}(k,\theta)e^{-i(m-m')\chi} \\ &\times \sum_{l_2,m_2,m_2'} \langle l,m,l',-m'|l_2,m_2\rangle\langle l,m_1,l',-m_1'|l_2,m_2'\rangle \\ &\times (-1)^{m_1'-m'} D^{l_2}_{m_2'm_2}(\phi,\theta,\chi) \\ &\times \sum_{LM}\langle l,0,l',0|L0\rangle\langle l,m_1,l',-m_1'|LM\rangle \\ &\times (-1)^{m_1'}\sqrt{\frac{(2l+1)(2l'+1)}{4\pi(2L+1)}}Y_L^M(\theta_k,\phi_k).\end{aligned} \tag{A.23}$$

The dependence of the $\tilde{b}_{lm}(k,\theta)$ coefficients on the polar angle θ can be expanded in the Legendre polynomial basis as

$$\tilde{b}_{lm}(\theta,k) = \sum_j \tilde{d}_{lmj}(k)P_j(\cos\theta). \tag{A.24}$$

The fully angle-resolved DCS $d\sigma/d\Omega d\Omega_k$ then becomes

$$\begin{aligned}\frac{d\sigma}{d\Omega d\Omega_k} =& \sum_{lm}\sum_{l'm'}\sum_{m_1m_1'}\sum_{LM}\sum_{l_2,m_2,m_2'}\sum_{jj'} \tilde{d}_{lmj}(k)\tilde{d}^*_{l'm'j'}(k) \\ &\times (-1)^{m_1'-m'}(-1)^{m_1'}e^{-i(m-m')\chi}P_j(\cos\theta)P_{j'}(\cos\theta) \\ &\times \langle l,m,l',-m'|l_2,m_2\rangle\langle l,m_1,l',-m_1'|l_2,m_2'\rangle \\ &\times D^{l_2}_{m_2'm_2}(\phi,\theta,\chi) \\ &\times \langle l,0,l',0|L0\rangle\langle l,m_1,l',-m_1'|LM\rangle \\ &\times \sqrt{\frac{(2l+1)(2l'+1)}{4\pi(2L+1)}}Y_L^M(\theta_k,\phi_k).\end{aligned} \tag{A.25}$$

The product of two Legendre polynomials can also be expanded in a series, which leads to

$$
\begin{aligned}
\frac{d\sigma}{d\Omega d\Omega_k} = & \sum_{lm}\sum_{l'm'}\sum_{m_1m_1'}\sum_{LM}\sum_{l_2,m_2,m_2'}\sum_{jj'}\sum_{j''}\tilde{d}_{lmj}(k)\tilde{d}^*_{l'm'j'}(k) \\
& \times (-1)^{m_1'-m'}(-1)^{m_1'}e^{-i(m-m')\chi} \\
& \times \langle j,0,j',0|j''0\rangle^2 P_{j''}(\cos\theta) \\
& \times \langle l,m,l',-m'|l_2,m_2\rangle\langle l,m_1,l',-m_1'|l_2,m_2'\rangle \\
& \times e^{-im_2'\phi}d^{l_2}_{m_2'm_2}(\theta)e^{-im_2\chi} \\
& \times \langle l,0,l',0|L0\rangle\langle l,m_1,l',-m_1'|LM\rangle \\
& \times \sqrt{\frac{(2l+1)(2l'+1)}{4\pi(2L+1)}}Y_L^M(\theta_k,\phi_k).
\end{aligned} \tag{A.26}
$$

The DCS measured in the LF is a summation of the fully angle-resolved DCS in Eq. (A.26) weighted by the time-dependent molecular axis distribution $\rho(\theta,\phi,\chi)$ excited by the alignment pulse. Technically, we need to multiply Eq. (A.26) by $\rho(\theta,\phi,\chi)$ and average over θ, ϕ and χ. Within the discussion of linearly polarized alignment pulses and linear molecules, spatially, the rotational wave packet only depends on the polar angle θ. Since $\rho(\theta,t)$ does not depend on ϕ and χ, we can perform the integration over χ and ϕ independently first, then multiply by $\rho(\theta,t)$ and average over θ later.

The integral over ϕ is non-zero only if $m_2'=0$, which makes $m_1=m_1'$ and $M=0$. This gives us

$$\begin{aligned}\frac{d\sigma}{d\theta d\chi d\theta_k} =& 2\pi \sum_{lm}\sum_{l'm'}\sum_{m_1}\sum_{L}\sum_{l_2,m_2}\sum_{jj'}\sum_{j''} \tilde{d}_{lmj}(k)\tilde{d}^*_{l'm'j'}(k) \\ &\times \frac{(-1)^{-m'}}{4\pi}\sqrt{(2l+1)(2l'+1)}e^{-i(m-m'+m_2)\chi} \\ &\times \langle j,0,j',0|j''0\rangle^2 \\ &\times \langle l,m,l',-m'|l_2,m_2\rangle\langle l,m_1,l',-m_1|l_2,0\rangle \\ &\times d^{l_2}_{0m_2}(\theta) \\ &\times \langle l,0,l',0|L0\rangle\langle l,m_1,l',-m_1|L0\rangle \\ &\times P_{j''}(\cos\theta)P_L(\cos\theta_k),\end{aligned} \tag{A.27}$$

where the dependence on ϕ and ϕ_k is gone.

The integral over χ is non-zero only if $m-m'+m_2=0$ and the Clebsch-Gordan coefficients require $m-m'=m_2$, making $m_2=0$ and $m'=m$. We then have

$$\begin{aligned}\frac{d\sigma}{d\theta d\theta_k} =& \sum_{lm}\sum_{l'}\sum_{m_1}\sum_{L}\sum_{l_2}\sum_{jj'}\sum_{j''} \tilde{d}_{lmj}(k)\tilde{d}^*_{l'mj'}(k) \\ &\times (-1)^{-m}\pi\sqrt{(2l+1)(2l'+1)} \\ &\times \langle j,0,j',0|j''0\rangle^2 \\ &\times \langle l,m,l',-m|l_2,0\rangle\langle l,m_1,l',-m_1|l_2,0\rangle \\ &\times \langle l,0,l',0|L0\rangle\langle l,m_1,l',-m_1|L0\rangle \\ &\times P_{l_2}(\cos\theta)P_{j''}(\cos\theta)P_L(\theta_k).\end{aligned} \tag{A.28}$$

Again, the product of two θ-dependent Legendre polynomials can be expanded in a series

$$\begin{aligned}\frac{d\sigma}{d\theta d\theta_k} = &\sum_{lm}\sum_{l'}\sum_{m_1}\sum_{L}\sum_{l_2}\sum_{jj'}\sum_{j''}\sum_{J}\tilde{d}_{lmj}(k)\tilde{d}^{*}_{l'mj'}(k)\\ &\times(-1)^{-m}\pi\sqrt{(2l+1)(2l'+1)}\\ &\times\langle j,0,j',0|j''0\rangle^2\langle l_2,0,j'',0|J0\rangle^2\\ &\times\langle l,m,l',-m|l_2,0\rangle\langle l,m_1,l',-m_1|l_2,0\rangle\\ &\times\langle l,0,l',0|L0\rangle\langle l,m_1,l',-m_1|L0\rangle\\ &\times P_J(\cos\theta)P_L(\cos\theta_k).\end{aligned} \tag{A.29}$$

The $\rho(\theta,t)$-weighted integration over θ then gives us the time-dependent photoelectron spectrum measured in the LF

$$\begin{aligned}\frac{d\sigma}{d\theta_k}(t) = &\sum_{L}\sum_{J}\sum_{ll'}\sum_{mm_1}\sum_{l_2}\sum_{jj'}\sum_{j''}\tilde{d}_{lmj}(k)\tilde{d}^{*}_{l'mj'}(k)\\ &\times(-1)^{-m}\pi\sqrt{(2l+1)(2l'+1)}\\ &\times\langle j,0,j',0|j''0\rangle^2\langle l_2,0,j'',0|J0\rangle^2\\ &\times\langle l,m,l',-m|l_2,0\rangle\langle l,m_1,l',-m_1|l_2,0\rangle\\ &\times\langle l,0,l',0|L0\rangle\langle l,m_1,l',-m_1|L0\rangle\\ &\times\langle P_J(\cos\theta)\rangle(t)P_L(\cos\theta_k).\end{aligned} \tag{A.30}$$

The expression in Eq. (A.30) is equivalent to Eq. (6.5) in section 6.2. By comparing the two, we can obtain

$$
\begin{aligned}
A_{JL}(k) =& \sum_{ll'} \sum_{mm_1} \sum_{l_2} \sum_{jj'} \sum_{j''} \tilde{d}_{lmj}(k) \tilde{d}^*_{l'mj'}(k) \\
& \times \frac{(-1)^{-m}}{2} \sqrt{(2l+1)(2l'+1)} \\
& \times \langle j, 0, j', 0 | j'' 0 \rangle^2 \langle l_2, 0, j'', 0 | J 0 \rangle^2 \\
& \times \langle l, m, l', -m | l_2, 0 \rangle \langle l, m_1, l', -m_1 | l_2, 0 \rangle \\
& \times \langle l, 0, l', 0 | L 0 \rangle \langle l, m_1, l', -m_1 | L 0 \rangle,
\end{aligned}
\tag{A.31}
$$

where $A_{JL}(k)$ are the real coefficients that we retrieved. The complex coefficients $\tilde{d}_{lmj}(k)$, and hence $\tilde{b}_{lm}(k)$ and the MF photoelectron wave function in Eq. (A.17), can be retrieved by fitting the real coefficients $A_{JL}(k)$ to the expansion in Eq. (A.31). In term of $A_{JL}(k)$, the AR-LFPAD expressed in Eq. (A.29) can be re-written as

$$
\frac{d\sigma}{d\theta d\theta_k} = 2\pi \sum_{JL} A_{JL}(k) P_J(\cos\theta) P_L(\theta_k),
\tag{A.32}
$$

which is the form that we use in the chapter.

In conclusion, starting from the MF photoelectron wave function in Eq. (A.17) and constructing the LFPAD at the end in Eq. (A.30), we obtain similar conclusions to the previous section. Because the LF has cyclindrical symmetry, expressions for the LFPAD and the coefficients $A_{JK}(k)$ are simpler when using LF expansion coefficients $\tilde{c}_{lm}$ (see Eq. (A.13) and Eq. (A.15)) compared to when using the MF expansion coefficients $\tilde{b}_{lm}$ (see Eq. (A.30) and Eq. (A.31)). The extra sums in the later case take care of the rotation of frames, however, we do not gain any new insights by writing it that way.

A.3 $A_{JL}(k)$ coefficients for selected ionization channels

In this section of the appendix, we print the $A_{JL}(k)$ coefficients for the channels presented in chapter 6. The coefficients are in arbitrary units; only their relative magnitudes are relevant.

	$J = 0$	$J = 2$	$J = 4$	$J = 6$
$L = 0$	15.91 ± 0.01	7.16 ± 0.05	-1.94 ± 0.07	-0.54 ± 0.10
$L = 2$	11.72 ± 0.02	8.11 ± 0.10	-3.28 ± 0.15	3.08 ± 0.21
$L = 4$	30.81 ± 0.03	3.90 ± 0.14	-10.21 ± 0.21	-0.24 ± 0.28
$L = 6$	12.99 ± 0.03	9.53 ± 0.16	-1.10 ± 0.24	-0.39 ± 0.32
$L = 8$	19.26 ± 0.04	24.91 ± 0.18	2.42 ± 0.27	-2.41 ± 0.37
$L = 10$	0.50 ± 0.04	-3.05 ± 0.19	-1.25 ± 0.29	1.19 ± 0.39

Table A.1: *$A_{JK}(k)$ coefficients for 4-photon ionization of* N_2 *into the* $X^2\Sigma_g$ *ionic state.*

<table>
<tr><td colspan="5">$\nu = 1$</td></tr>
<tr><td></td><td>$J = 0$</td><td>$J = 2$</td><td>$J = 4$</td><td>$J = 6$</td></tr>
<tr><td>$L = 0$</td><td>6.83 ± 0.01</td><td>6.50 ± 0.04</td><td>3.01 ± 0.06</td><td>-0.25 ± 0.08</td></tr>
<tr><td>$L = 2$</td><td>0.34 ± 0.02</td><td>-8.74 ± 0.08</td><td>-3.79 ± 0.12</td><td>0.67 ± 0.16</td></tr>
<tr><td>$L = 4$</td><td>2.94 ± 0.02</td><td>6.98 ± 0.10</td><td>5.37 ± 0.16</td><td>2.23 ± 0.21</td></tr>
<tr><td>$L = 6$</td><td>1.38 ± 0.02</td><td>-10.96 ± 0.12</td><td>-7.28 ± 0.19</td><td>-4.39 ± 0.25</td></tr>
<tr><td>$L = 8$</td><td>0.51 ± 0.03</td><td>2.29 ± 0.14</td><td>2.14 ± 0.21</td><td>0.69 ± 0.29</td></tr>
<tr><td colspan="5">$\nu = 2$</td></tr>
<tr><td></td><td>$J = 0$</td><td>$J = 2$</td><td>$J = 4$</td><td>$J = 6$</td></tr>
<tr><td>$L = 0$</td><td>3.35 ± 0.01</td><td>0.13 ± 0.03</td><td>1.17 ± 0.04</td><td>0.05 ± 0.06</td></tr>
<tr><td>$L = 2$</td><td>1.33 ± 0.01</td><td>-4.36 ± 0.06</td><td>-1.13 ± 0.08</td><td>-0.60 ± 0.11</td></tr>
<tr><td>$L = 4$</td><td>-0.74 ± 0.01</td><td>3.42 ± 0.07</td><td>1.80 ± 0.11</td><td>1.27 ± 0.15</td></tr>
<tr><td>$L = 6$</td><td>0.47 ± 0.02</td><td>-3.00 ± 0.09</td><td>-0.15 ± 0.13</td><td>-1.1 ± 0.18</td></tr>
<tr><td>$L = 8$</td><td>0.05 ± 0.02</td><td>-0.26 ± 0.10</td><td>0.41 ± 0.15</td><td>0.05 ± 0.20</td></tr>
<tr><td colspan="5">$\nu = 3$</td></tr>
<tr><td></td><td>$J = 0$</td><td>$J = 2$</td><td>$J = 4$</td><td>$J = 6$</td></tr>
<tr><td>$L = 0$</td><td>5.73 ± 0.01</td><td>0.05 ± 0.04</td><td>0.17 ± 0.06</td><td>0.27 ± 0.08</td></tr>
<tr><td>$L = 2$</td><td>4.36 ± 0.02</td><td>-4.89 ± 0.08</td><td>-2.25 ± 0.12</td><td>-0.46 ± 0.16</td></tr>
<tr><td>$L = 4$</td><td>0.76 ± 0.02</td><td>0.40 ± 0.11</td><td>1.21 ± 0.16</td><td>2.84 ± 0.22</td></tr>
<tr><td>$L = 6$</td><td>1.66 ± 0.03</td><td>-5.47 ± 0.13</td><td>1.80 ± 0.19</td><td>-1.73 ± 0.26</td></tr>
<tr><td>$L = 8$</td><td>0.09 ± 0.03</td><td>-0.65 ± 0.15</td><td>0.14 ± 0.22</td><td>0.20 ± 0.30</td></tr>
</table>

Table A.2: *$A_{JK}(k)$ coefficients for 4-photon ionization of* N_2 *into three different vibrational levels of the first excited state* $A^2\Pi_u$ *of the cation.*

	$J = 0$	$J = 2$	$J = 4$	$J = 6$
$L = 0$	1.00 ± 0.001	0.44 ± 0.003	-0.35 ± 0.006	0.06 ± 0.008
$L = 2$	1.65 ± 0.001	0.51 ± 0.006	-1.37 ± 0.012	0.04 ± 0.018
$L = 4$	1.15 ± 0.001	1.03 ± 0.008	-1.47 ± 0.016	-0.08 ± 0.023
$L = 6$	0.19 ± 0.002	0.48 ± 0.098	-2.04 ± 0.019	-0.41 ± 0.028
$L = 8$	-0.01 ± 0.002	0.01 ± 0.011	-0.19 ± 0.021	-0.09 ± 0.032

Table A.3: *$A_{JK}(k)$ coefficients for three-photon ionization of $\mathrm{CO_2}$ into the ground state, $\tilde{\mathrm{X}}^2\Pi_\mathrm{g}$, of the ion.*